



Title	Studies on tracked dynamic model and optimum harvesting area for path planning of robot combine harvester
Author(s)	Rahman, Md. Mostafizar
Citation	北海道大学. 博士(農学) 甲第13158号
Issue Date	2018-03-22
DOI	10.14943/doctoral.k13158
Doc URL	http://hdl.handle.net/2115/75608
Type	theses (doctoral)
File Information	Md._Mostafizar_Rahman.pdf



[Instructions for use](#)

STUDIES ON TRACKED DYNAMIC MODEL AND OPTIMUM HARVESTING AREA FOR PATH PLANNING OF ROBOT COMBINE HARVESTER

(ロボットコンバインのダイナミックモデル構築と走行経路生成の
ための収穫領域最適化に関する研究)



By

Md. Mostafizar Rahman

Dissertation

*Submitted to Division of Environmental Resources in the
Graduate school of Agriculture
Hokkaido University, Sapporo, 060-8589, Japan, in particular fulfillment
of the requirements for the degree of*

Doctor of Philosophy

2018

TABLE OF CONTENTS

TABLE OF CONTENTS	I
ABSTRACT	IV
ACKNOWLEDGMENT	VI
LIST OF FIGURES	VIII
LIST OF TABLES	XII
NOTATIONS	XIII
UNITS OF MEASUREMENT	XVII
ACRONYMS AND ABBREVIATIONS	XVIII
Chapter 1 Introduction	1
1.1 Research Background	1
<i>1.1.1 Concept of Autonomous Agricultural Vehicles</i>	1
<i>1.1.2 Research on Autonomous Combine Harvester</i>	4
<i>1.1.3 Research on Sensors and Sensor Fusion</i>	5
<i>1.1.4 Research on Tracked Vehicle Motion Model</i>	7
<i>1.1.5 Research on Path Planning of Agricultural Vehicles</i>	9
1.2 Research Motivation and Objectives	10
Chapter 2 Research Platform, Materials and Methods	14
2.1 Introduction	14
2.2 Research Platform	14
<i>2.2.1 Tracked Combine Harvester</i>	14
2.3 Research Materials	17
<i>2.3.1 RTK-GPS</i>	17
<i>2.3.2 IMU</i>	23
2.4 Research Methods	26
<i>2.4.1 Kalman Filter</i>	26
<i>2.4.2 Convex Hull Method</i>	31
<i>2.4.3 Rotating Caliper Method</i>	34
2.5 Conclusions	36
Chapter 3 Tracked Motion Model for Tracked Combine Harvester	37
3.1 Introduction	37

3.2	Materials and Method.....	39
3.2.1	<i>System Components</i>	39
3.2.2	<i>Tracked Combine Harvester dynamic model</i>	41
3.2.3	<i>Tracked Combine Harvester Kinematic model</i>	45
3.2.4	<i>Methods</i>	48
3.3	Results and Discussion.....	49
3.3.1	<i>Trajectories of Tracked Combine Harvester</i>	49
3.3.2	<i>Yaw rate of Tracked Combine Harvester</i>	51
3.3.3	<i>Speed of Tracked Combine Harvester</i>	53
3.3.4	<i>Sideslip angle of Tracked Combine Harvester</i>	55
3.3.5	<i>Turning Radius of Tracked Combine Harvester</i>	57
3.3.6	<i>Tracks slip of Tracked Combine Harvester</i>	59
3.3.7	<i>Lateral Coefficient of Friction</i>	60
3.3.8	<i>Longitudinal Coefficient of Friction</i>	62
3.4	Conclusions	63
Chapter 4 Heading Estimation of Tracked Combine Harvester during Nonlinear Maneuverability		65
4.1	Introduction	65
4.2	Materials and Methods	67
4.2.1	<i>System platform and sensors</i>	67
4.2.2	<i>Tracked combine harvester model</i>	68
4.2.3	<i>RTK-GPS and IMU Fusion Algorithm</i>	69
4.3	Results and Discussion.....	73
4.3.1	<i>Trajectory of Tracked Combine Harvester</i>	73
4.3.2	<i>Estimated Heading of Circular Trajectory</i>	75
4.3.3	<i>Estimated Heading of Sinusoidal Trajectory</i>	80
4.3.4	<i>Estimated heading of convex and concave polygon field</i>	85
4.4	Conclusions	89
Chapter 5 Optimum Harvesting Area for Path Planning of Robot Combine Harvester		90
5.1	Introduction	90
5.2	Materials and methods.....	91
5.2.1	<i>Research platform and sensors</i>	91
5.2.2	<i>Automatic Path planning algorithm</i>	93
5.2.3	<i>Header end position</i>	95

5.2.4 Convex hull algorithm	96
5.2.5 Optimum area of Rectangle by Rotating Caliper method	97
5.2.6 Optimum area of Convex polygon from N-Polygon algorithm	98
5.2.7 Optimum area of Concave polygon from Concave hull algorithm.....	100
5.2.8 Working path and waypoints algorithm	102
5.3 Results and Discussion.....	104
5.3.1 Estimated Header end position.....	104
5.3.2 Estimated Convex and Concave Hull	105
5.3.3 Estimated the optimum harvesting area of polygon field	108
5.3.4 Comparison of Optimum Harvesting Area	110
5.3.5 Estimated working path of the convex and concave polygon field.....	111
5.4 Conclusions	116
Chapter 6 Research Summary and Conclusion.....	117
6.1 Introduction	117
6.2 Summary of Each Chapter.....	117
6.3 Contributions	119
6.3.1 Tracked Combine Harvester Motion Model.....	119
6.3.2 Heading Estimation Method.....	119
6.3.3 Optimization of Harvesting Area of Convex and Concave Polygon field	119
6.3.4 Path Planning for Convex and Concave Polygon field	120
6.4 Future Work	120
References	121

ABSTRACT

Automatic path planning is an important topic nowadays for robotic agricultural vehicles. Especially for a robot combine harvester, path planning is required to choose the crop field of optimum harvesting area; otherwise, crop losses may occur during harvesting of the field. In general, a boundary zone in the field includes some water inlets and outlets, or some objects that are very dangerous for a robot running. In order to make the turning margin safe for the robot combine harvester operation, the surrounding crop near to boundary zone is cut twice or thrice by manual operation; however, this surrounding cutting crop is not exactly straight, sometimes it is curved or meandering. Developing a path planning in a conventional way, in order to take a corner position from the global positioning system by visual observation is a time consuming operation; the curved or meandering crop is not cut during harvesting, and the harvesting area is not optimum. During harvesting, this curved or meandering crop may be left in the field, which indicates the crop losses. In addition, normally, the tracked combine harvester takes turn at high speed and high steering command at the corner of the field during the cutting of outside crop nearby headland. During this turning, the inertial sensor gives the yaw rate gyro measurement bias, which is necessary to compensate for estimating absolute heading to determine the crop periphery. In order to consider the crop losses, operational processing time and compensating yaw rate gyro measurement bias, a tracked dynamic model of tracked combine harvester and optimum harvesting area of convex or concave polygon form in the field are very important. Therefore, this research's objective is to develop a tracked combine harvester dynamic model based on the sensor measurements for estimating the absolute heading of tracked combine harvester, and an algorithm that the optimum harvesting area for a convex or concave polygon field in determining the corner vertices to calculate the working path of a robot combine harvester.

A real time global positioning system and an inertial measurement unit with tracked combine harvester dynamic model are used to calculate the absolute heading in turning maneuverability, which is further used to determine the combine harvester's header end position that is called the exact outline of the remaining crop or crop periphery. Incremental convex hull method is used to estimate the convex hull from the exact outline crop position, and the optimum harvesting area and corner vertices are estimated by the rotating caliper method. However, this rotating caliper method is only suitable for a rectangular polygon field. Unlike the rotating caliper method, the developed N-polygon algorithm is applicable to all convex polygon fields. Similarly, we developed another algorithm for concave polygon fields, which is called the split of convex hull and cross point method. This method calculates the optimum harvesting area and the corner vertices from the concave polygon (like L-shape) field. The simulation and experimental results showed that our developed algorithm can estimate the optimum harvesting area and corner vertices for a convex or a concave polygon field, which takes all crop portions. Then, a path planning algorithm is used to calculate the working path based on the estimated corner vertices for the robot combine harvester, which cuts whole crop in the field during harvesting. In conclusion, the tracked combine harvester model with sensor fusion method can estimate absolute heading in course of turning condition, and the estimated optimum harvesting area based on our algorithm completely reduces the crop losses, and the working path calculated based on the corner vertices requires less processing time.

ACKNOWLEDGMENT

Undertaking this Ph.D has been a really life-changing experience for mine and it was difficult to do without the continuous support, guidance and advice which I received eagerly from some well-wisher.

First and foremost I would like to express my sincere gratitude to my advisor Dr. Kazunobu Ishii, who has supported me throughout my Ph.D study and related research with his patience, motivation and immense knowledge. I attribute the level of my Ph.D degree to his encouragement and effort, and without him this dissertation, too, would not have been completed or written.

Besides my advisor, I would like to show my greatest appreciation to the eminent and respectable Professor Noboru Noguchi who was accepted me as a student in his vehicle robotics laboratory which is renowned in the world. I am also pleased on him for his deep concern about my research in the past there years, and for his kind advices.

I would like to thank Dr. Hiroshi Okamoto who gave me constructive comments and warm encouragement during my research. I am also indebt to Ms. Mami Aoki and Ms. Tomoko Namikawa who helped and supported me about any official difficulties, which was easier to live me in Sapporo, Japan. Special thanks to brother Mr. Ricardo Ospina Alarcon who helped and advised me in the period of my research. I am also grateful to Dr. Yufei Liu and Dr. Chi Zhang for their kind help and advice during my research. I want to say thanks to my friends Mr Roshanianfard Ali and Du Mengmeng for their friendly behavior, motivation and encouraging talk about our research and also our cultures. I also want to say thanks to the master's student Mr. Tatsuki kamada and Mr.

Kannapat Udompant for their kind help in the course of my experiment in the field. I am also thankful to all members, Laboratory of Vehicle Robotics for their kindness, friendliness and supporting in my research.

Finally, I owe my deepest gratitude to my beloved parents, father and mother in law, wife and son, who gave me unconditional support, love and advice to be patience sothat I can enjoy my study, research and livelihood in Japan. Therefore, I dedicated this dissertation to my lovely family.

LIST OF FIGURES

Figure 1-1. Agricultural population and age percentage of agricultural population in Japan (Source: Ministry of Agriculture, Forestry and Fisheries; Statistics Bureau, 2016)	2
Figure 1-2. Basic elements of autonomous guidance system for agricultural vehicles (Reid et al., 2000)	3
Figure 1-3. Schematic of the corner vertices determined conventionally and the curve or meandering portion	12
Figure 2-1. A Yanmer AG1100 model combine harvester	15
Figure 2-2. Overall controlling architecture of a robot combine harvester (Source: Zhang, 2014)	17
Figure 2-3. Schematic view of Virtual Reference Station (VRS) for RTK-GPS position	20
Figure 2-4. Real view of Topcon RTK-GPS receiver and antenna	21
Figure 2-5. Real view of Inertial Measurement Unit (IMU)	24
Figure 2-6. Overview of Kalman Filter and Extended Kalman Filter Cycle	30
Figure 2-7. Convex hull of a finite set P assumed by a rubber band	32
Figure 2-8. Schematic representation of incremental convex hull method (a. sorting of points cloud, b. convex hull when $i = 2$, c. convex hull when $i = 3$, d. convex hull when $i = 4$)	33
Figure 2-9. Division of convex hull for upper and lower hull	34
Figure 2-10. Estimation of a rectangle using Rotating Calipers method	36
Figure 3-1. Outlook of the tracked combine harvester equipped with RTK-GPS and IMU sensors	40
Figure 3-2. Free body diagram of the tracked combine harvester dynamic model (a. General forces acting on the harvester and b. Detail of centrifugal force, F_c)	42

Figure 3-3. Schematic representation of the tracked combine harvester’s speed, slip velocity and turning radius.....	45
Figure 3-4. Turning radius R calculated from the RTK-GPS positions	46
Figure 3-5. Measured Trajectory (MTrajectory) and Dynamic model trajectory (DTrajectory) of the tracked combine harvester which runs in a circular way	50
Figure 3-6. Measured Trajectory (MTrajectory) and Dynamic model trajectory (DTrajectory) of the tracked combine harvester which runs in a sinusoidal way	51
Figure 3-7. Measured yaw rate (MYawrate) and Dynamic model yaw rate (DYawrate) of the tracked combine harvester which runs in a circular way	52
Figure 3-8. Measured yaw rate (MYawrate) and Dynamic model yaw rate (DYawrate) of the tracked combine harvester which runs in a sinusoidal way	53
Figure 3-9. Speed of the tracked combine harvester for circular trajectories.....	54
Figure 3-10. Speed of the tracked combine harvester for sinusoidal trajectories.....	54
Figure 3-11. Measured and theoretical sideslip angle β for the circular trajectories	56
Figure 3-12. Measured and theoretical sideslip angle β for the sinusoidal trajectories ...	56
Figure 3-13. Measured and theoretical turning radius R for the circular trajectories.....	58
Figure 3-14. Measured and theoretical turning radius R for the sinusoidal trajectories...	58
Figure 3-15. Computed slip of left and right tracks for the circular trajectories	59
Figure 3-16. Computed slip of left and right tracks for the sinusoidal trajectories	60
Figure 3-17. Lateral coefficient of circular trajectories for the concrete and soil ground	61
Figure 3-18. Lateral coefficient of sinusoidal trajectories for the concrete and soil ground	61
Figure 3-19. Longitudinal coefficient of friction for the left and right tracks computed for the circular trajectories on the concrete and soil ground	62

Figure 3-20. Longitudinal coefficient of friction for the left and right tracks computed for the sinusoidal trajectories on the concrete and soil ground	63
Figure 4-1. Circle representing the turning area of the tracked combine harvester.....	67
Figure 4-2. Circular trajectories of the tracked combine harvester at different input steering angles.....	74
Figure 4-3. Sinusoidal trajectories of the tracked combine harvester at different input steering angles.....	74
Figure 4-4. Measured and estimated headings (top figures) for circular trajectories as well as heading difference (below figures). (Where, GPSH = GPS Heading, MH = Measured Heading, EH = Estimated Heading and GPSH (Reg) = Linear Regression of GPS Heading).....	79
Figure 4-5. Measured and estimated headings (top figures) for sinusoidal trajectories as well as heading difference (below figures). (Where, GPSH = GPS Heading, MH = Measured Heading, EH = Estimated Heading and GPSH (Reg) = Linear Regression of GPS Heading)	84
Figure 4-6. Estimated heading for convex and concave polygon field during field.....	87
Figure 4-7. Heading difference for convex and concave polygon field	88
Figure 5-1. Robot combine harvester equipped with RTK-GPS position and IMU direction sensors.....	92
Figure 5-2. Automatic path planning algorithm of the robot combine harvester	94
Figure 5-3. Heading angle of the robot combine harvester for estimating the header's end position.....	95
Figure 5-4. Convex hull from a finite set of RTK-GPS position of convex polygon.....	97
Figure 5-5. Optimum harvesting area of rectangle obtained by the Rotating Caliper method.....	98

Figure 5-6. Optimum harvesting area of an N-angular shape polygon.....	99
Figure 5-7. Schematic of a concave hull by the split of convex hull and cross point method.....	102
Figure 5-8. Schematic representation of the estimated path for the robot combine harvester.....	103
Figure 5-9. Estimated Header end position from the measured RTK-GPS position $P(X_i, Y_i)$ and heading angle φ of the robot combine harvester	105
Figure 5-10. Estimated vertices of convex and concave hull from the crop perimeter of convex and concave polygon field.....	107
Figure 5-11. Estimated optimum harvesting area and corner vertices of convex and concave polygon field.....	110
Figure 5-12. Comparison of the optimum and conventional harvesting area of convex polygon field.....	111
Figure 5-13. Estimated working path of the convex and concave polygon field	113
Figure 5-14. Estimated working path of the robot combine harvester during experiment in a rectangular wheat field.....	114
Figure 5-15. Estimated working path of the robot combine harvester during experiment in a concave wheat field.....	115

LIST OF TABLES

Table 2-1. Specifications of Yanmer AG1100 Combine Harvester (Source: Zhang, 2014)	16
Table 2-2. Specifications of RTK-GPS receiver.....	21
Table 2-3. Specifications of RTK-GPS antenna.....	22
Table 2-4. Specifications of Inertial Measurement Unit (IMU)	25
Table 4-1. RMS error for Measured and Estimated heading.	76
Table 4-2. RMS error for measured and estimated heading.	81

NOTATIONS

(C_x, C_y)	Centroid of polygon
(G_x, G_y)	Gravity point
(x', y')	Way point
(x_c, y_c)	Cross point
(x_i, y_i)	Corner point
(a, b)	Center of circle
\hat{P}_{k+1}	Estimated covariance
\dot{X}_{k+1}	Tracked combine harvester velocity in X-direction at time t_{k+1}
\dot{Y}_{k+1}	Tracked combine harvester velocity in Y-direction at time t_{k+1}
\ddot{x}_c	Acceleration of longitudinal axis for the tracked combine harvester
\hat{x}_{k+1}	Estimate state
\ddot{y}_c	Acceleration of lateral axis for the tracked combine harvester
$\dot{\phi}_k$	Yaw rate at time t_k
$\dot{\phi}_{k+1}$	Yaw rate at time t_{k+1}
A_k	Jacobian matrix for state transition
F_L	Thrust of left track
F_R	Thrust of right track
F_c	Resultant centrifugal force
F_{cx}	Centrifugal force in longitudinal direction
F_{cy}	Centrifugal force in lateral direction
H_k	Jacobian matrix for measurement
M_r	Moment of turning resistance
P_{k+1}	Predicated covariance

Q_k	Process noise for extended kalman filter
R'	Distance from instantaneous center of rotation and center of gravity
R_L	Resistive force for left track
R_R	Resistive force for right track
R_k	Measurement noise for extended kalman filter
V_L	Left track velocity
V_R	Right track velocity
V_c	Velocity of tracked combine harvester
V_{gps}	Velocity from GPS
V_{sl}	Slip velocity for left track
V_{sr}	Slip velocity for right track
\dot{X}	Velocity in longitudinal direction in global frame
X_i	i^{th} Longitude
X_k	Tracked combine harvester position in east direction at time t_k
X_{k+1}	Tracked combine harvester position in east direction at time t_{k+1}
\dot{Y}	Velocity in lateral direction in global frame
Y_i	i^{th} Latitude
Y_k	Tracked combine harvester position in north direction at time t_k
Y_{k+1}	Tracked combine harvester position in north direction at time t_{k+1}
f_y	Lateral friction force
v_k	Innovation for extended kalman filter
x_c	Longitudinal axis of tracked combine harvester
y_c	Lateral axis of tracked combine harvester

z_{k+1}	Predicated measurement
μ_l	Longitudinal coefficient of left track
μ_r	Longitudinal coefficient of right track
$\dot{\varphi}$	Yaw rate
$\ddot{\varphi}$	Yaw rate acceleration
φ_{gps}	Heading angle from GPS
φ_{imu}	Heading angle from IMU
φ_k	Heading of tracked combine harvester at time t_k
φ_{k+1}	Heading of tracked combine harvester at time t_{k+1}
A	Area
A	Amplitude
A, B, C	Undetermined coefficients
B	Tread of tracked combine harvester
$CP(X_i, Y_i)$	i^{th} cross points
D	Distance shifting along longitudinal direction
I	Moment of Inertia
K	Kalman gain
L	Length of track
$P(X_H, Y_H)$	Header end position of tracked combine harvester
$P(X_i, Y_i)$	GPS position
R	Turning radius
S	Innovation covariance for extended kalman filter
$V(X_i, Y_i)$	i^{th} corner vertices
X	X-axis coordinate in global frame

XYZ	3-axis coordinates in global frame
Y	Y-axis coordinate in global frame
a	Slope of line
b	Intercept of line
bm	Intercept for next line
d	Header length
g	Gravitational acceleration
m	Mass of tracked combine harvester
t	Time
β	Sideslip angle
θ	Offset angle
μ	Lateral coefficient of friction
φ	Heading angle of tracked combine harvester
S_l	Slip for left track
S_r	Slip for right track
H	Center height
φ_{gk+1}	Heading from GPS at time t_{k+1}
b_{k+1}	Yaw rate gyro measurement bias at time t_{k+1}
$CH(P_0, P_1 \dots P_i)$	i^{th} vertices of convex hull

UNITS OF MEASUREMENT

hp	Horsepower
kW	Kilowatt
rpm	Revolutions per minute
mm	Millimeter
kg	Kilogram
m/s	Meter per second
Hz	Hertz (one cycle per second)
Sec	Second
m	Meter
MHz	Megahertz
dB _c	Decibels relative to the carrier
g	Gram
deg./sec	Degree per second
deg.	Degree
kHz	Kilohertz
hr	Hour
°/sec	Degree per second
mg	Milligram
Gauss	Magnetic flux density Unit
mbar	Millibar
°C	Degree Celsius
ppm	Parts per million
rad/sec	Radian per second
m ²	Square meter

ACRONYMS AND ABBREVIATIONS

2D	Two Dimensional
3D	Three Dimensional
3DOF	Three Degree of Freedom
5DOF	Five Degree of Freedom
AHRS	Attitude and Heading Reference System
BINEX	Binary Exchange Format
CAN	Control Area Network
CCH	Concave Hull
CEP	Circular Error Probability
CG	Center of Gravity
CH	Convex Hull
CMR	Compact Measurement Record
CP	Cross Point
CT	Combine Harvester Trajectory
DGPS	Differential Global Positioning System
ECU	Electrical Control Unit
EGNOS	European Geostationary Navigation Overlay Service
EH	Estimated Heading
FOG	Fiber Optic Gyroscope
FPID	Field Programmable Interconnect Device
FS	Full Scale
GB-3	G3 Dual Frequency Receiver
GDS	Geomagnetic Direction Sensor

GEONET	GPS Earth Observation Network
GGA	Output Message from Global Positioning
GIS	Geographic Information System
GLONASS	GLObalnaya NAVigatsionnaya Sputnikovaya Sistema (Russian Name)
GNSS	Global Navigation Satellite System
GPS	Global Positioning System
GPSH	Global Positioning System Heading
H	Height
ICR	Instantaneous Center of Rotation
IMU	Inertial Measurement Unit
INS	Inertial Navigation System
ISO	International Standards Organization
L	Length
LT	Left Crawler Track
MEMS	Micro-Electro-Mechanical System
MH	Measured Heading
MSAS	MTSAT Satellite Augmentation System
NMEA	National Marine Electronics Association
pc	Personal Computer
PDF	Probability Distribution Function
PG-S1	Topcon Antenna
PID	Proportional-Integral-Derivative
PTO	Power Take Off
RMS	Root Mean Square
RS232	Recommended Standard 232

RT	Right Crawler Track
RTCM	Radio Technical Commission for Maritime
RTK	Real Time Kinematic
RTK-GPS	Real Time Kinematic Global Positioning System
TNC	Terminal Node Controller
TSP	TSP File Extension
UNC-2B	Unified National Coarse-2B
USB	Universal Serial Bus
V	Vertex
VNIMU	Header for Asynchronous Solution Output Type
VNYMR	Header for Asynchronous Solution Output Type
VRS	Virtual Reference Station
W	Width
WAAS	Wide Area Augmentation System
YANMAR	Japanese Diesel Engine Manufacturer

Chapter 1 Introduction

1.1 Research Background

1.1.1 Concept of Autonomous Agricultural Vehicles

The concept of autonomous agricultural vehicles is introduced in Japan due to decrease the number of agricultural population in the commercial agricultural industries and increase their age. In 1995, about 4.14 million peoples were involved in agricultural farming of which 43.5 percent of agricultural farmers aged were 65 years and over. But, this figure changed over two decades. About 2.10 million peoples were engaged in agricultural farming as their principal occupation that is called commercial farmers in 2015, of whom 63.5 percent were aged 65 years and over (Statistics Bureau, 2016) as shown in figure 1-1. In addition, young peoples are not interest to come in agricultural sector considering it as a principal occupation. Since, the aged of agricultural populations are increasing and young peoples are not coming in this sector, a smart agricultural system play an important role to overcome this situation in Japan, of which one is autonomous agricultural vehicles.

Another concept is that the industrial civilization moves up into the agricultural industries to change the manual and animal power system to the mechanical power system in 20th century by providing agricultural vehicles (Liu, 2017). These agricultural vehicles are operated in the field by a human driver for the operation of cultivating, planting, fertilizing, weeding and harvesting, even the weather condition is sunny, windy and rainy, because the drivers are in the cabin of those vehicles. But it is a little bit difficult for the driver to pay concertation all the time in the field during the operation of agricultural vehicles, and the fatigue of driver

is likely to happen. Due to consider this fact, the human driver can be replaced by the autonomous guidance vehicles which can solve this problem, and work continually in the field, since an autonomous guidance vehicles or a robot never fails to concentrate (Zhang, 2014).

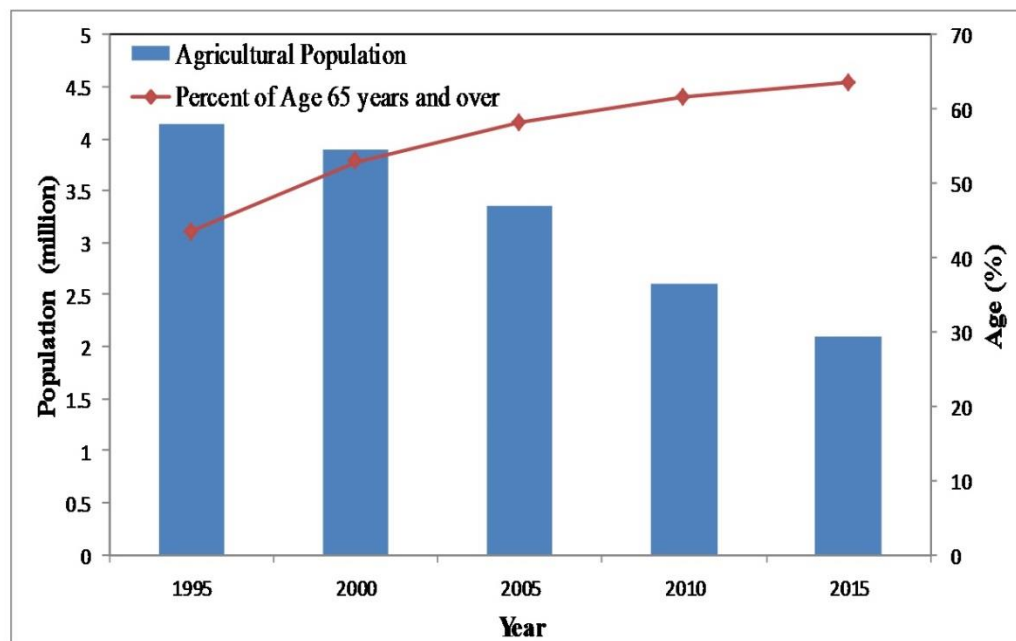


Figure 1-1. Agricultural population and age percentage of agricultural population in Japan (Source: Ministry of Agriculture, Forestry and Fisheries; Statistics Bureau, 2016)

An autonomous guidance system is an auto steered controlling system for a vehicle using a guidance system that shows the target path and current position of a vehicle via a User Interface. On the other hand, a robot vehicle is an autonomous vehicle of which the steering, engine rotation, speed, PTO, Hitch, Header etc. of a vehicle controlled automatically (Choi, 2014). Generally, there are two types of autonomous agricultural vehicles developed for agricultural production, of which one is used for outdoor field operations such as tillage, planting, fertilizing, weeding, harvesting and transportation (Chateau et al., 2000; Bell, 1999; Fehr et al., 1995;

Noguchi, 1998; Reid & Searcy, 1987; Stombaugh et al., 1998; Choi, 2014). Another is involved mainly for indoor field operations like green-house system (Mandow et al., 1996; Sandini et al., 1990; Van Henten et al., 2002; Belforte et al., 2006; Julian et al., 2010). Reid et al. (2000) described an autonomous guidance framework for agricultural vehicles, which is given in figure 1-2. The basic elements of autonomous guidance system are navigation sensors, vehicle models, navigation planner and steering controller, which each elements have the own function for supporting the agricultural vehicles to complete the autonomous system.

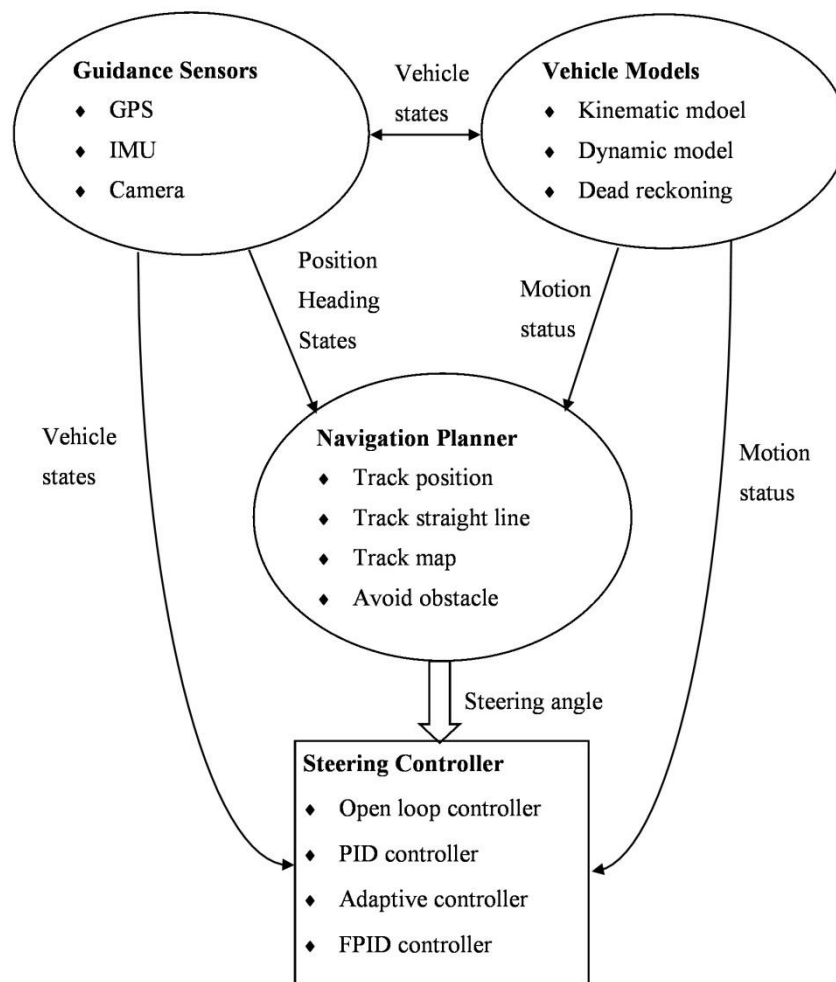


Figure 1-2. Basic elements of autonomous guidance system for agricultural vehicles (Reid et al., 2000)

1.1.2 Research on Autonomous Combine Harvester

A modern combine harvester, or simply combine, is a versatile machine designed to harvest a variety of cereal crops efficiently in the field to deliver clean grains, usually collected in the combine storage tank and discharged periodically for transportation and further processing or storage. An autonomous combine harvester or a robot combine harvester is capable to work in the field while a human supervisor assigned a program. There are three tasks done by the robot combine harvester to maintain a permanent communication with the human supervisor (Miu, 2016). These are (1) the automatic navigation on the road and in the field, (2) self-acting and reacting to its environment (other vehicles, obstacles, road conditions, etc.), and (3) self-regulating the harvesting process of a crop.

Research in Japan is going on about the autonomous combine harvester which is instrumented with a guidance sensors sothat it can work in the field more friendlyly with human operator. An autonomous combine harvester was developed utilizing a commercially available head feeding type combine harvester which is integrated by the position and azimuth data from the GPS and azimuth sensors, and controlled by the CAN bus (Iida et al., 2016; Saito et al., 2012 & 2013). Kurita et al. (2017) reported an operational frame work for autonomous rice harvesting by developed an integrated algorithm for robotic operation and cooperation for farm workers to automate each subsection of the harvesting and unloading process. A robot combine harvester is developed successfully in Hokkaido University, Japan by utilizing the Global and local sensor such as Global Navigation Satellite System (GNSS), Inertial Measurement Unit (IMU), Laser scanner and camera sensors to harvest rice, wheat and soybean crops, which is controlled by CAN (Zhang, 2014; Choi, 2014).

Research in other countries, a machine vision guidance algorithm is developed to guide an agricultural combine harvester for maize harvesting to detect the lateral position of the crop cut edge (Benson et al., 2003). On the other hand, Rovira-Más et al. (2007) developed an algorithm that is capable of finding the edge of corn using stereo vision, and allowing the system to automatically guide the combine harvester at regular speed. An automatic guidance system is developed for a combine harvester which steering system is controlled based on the measured position of the swath on the field by using laser scanner (Coen et al., 2008). Cordesses et al. (2000) evaluated Real Time Kinematic GPS for controlling of combine harvester without any orientation sensor.

1.1.3 Research on Sensors and Sensor Fusion

Sensors are used to monitor the surrounding environment in order to enhance our decisions for the development of autonomous guidance. There are two types of sensor used for autonomous guidance. These are the global sensor (like GPS) and local sensor (like IMU, GDS, Camera, Laser scanner, etc.), which are used to measure the position, the direction of autonomous vehicles and surrounding environments. Researches in the past have been conducted based on these global and local sensors by some scholar's. For instance, a robot tractor is developed by using a vision sensor and GDS sensor (Ishii et al., 1994, 1995 & 1998; Noguchi et al., 1997). Tillet et al. (1998) described a robot system for plant-scale husbandry by using vision sensor, wheel speed sensor, GDS and inclination sensor. Stombaugh et al. (1998) and Bell (2000) used a Kinematic differential GPS for autonomous navigation system by installing an automate steering of tractor. Cho et al. (1999) developed a speed sprayer by using machine vision and ultra-sonic sensor. Reid et al. (2000) developed automatic windrower by using machine vision system, whereas Kise et al. (2001 &

2003) used a RTK-GPS and FOG for developing a robot tractor. Nagasaka et al. (2004, 2009 & 2013) developed an autonomous guidance for rice transplanting by using a global positioning and inertial system. Suguri et al. (2004) developed an autonomous crawler wagon based on RTK-GPS and rotary encoders at driving wheels. Takai et al. (2010) developed a crawler-type robot tractor by using GPS and IMU. Ahamed et al. (2004) used a laser scanner for developing a positioning method based on reflectors for infield navigation of autonomous tractor. Yang and Noguchi (2014) used a 2D laser scanner for obstacle detection for autonomous vehicles at both indoor and outdoor environment.

In general, a single sensor is not capable of providing enough information; therefore, multiple sensor is integrated in a way to perform the additional task of interpretation, which may be more useful and informative than what can be monitored using a single sensor. Since, the sensor's functional characteristics can lead to output which contains erroneous measurement reading due to noise, measurement errors and time delays, multiple sensors are required to ensure the certainty of desired actions. For sensors to work properly, a computational method is needed to fuse sensor data in a process, which is called sensor fusion (Adla et al., 2013). Noguchi et al. (1998) developed a guidance system based on the sensor fusion by using RTK-GPS, GDS and machine vision. Inoue et al. (1999) used an automatic tractor based on sensor fusion the by using Kalman-filter. Nagasaka et al. (1999) developed a robot transplanting machine by the fusion of an RTK-GPS and a FOG. Hague et al. (2000) developed a ground based sensing systems for autonomous agricultural vehicles by using machine vision, odometers, accelerometers, and compass, where sensor fusion is accomplished using an extended kalman filter. Randle et al. (1997) used sensor fusion method which is kalman filter to integrate GPS and low cost INS sensor for

both flight and land vehicle navigation. English et al. (2013) estimated pose of a prototype agricultural robot by fusing data from a low-cost global positioning sensor, low-cost inertial sensors and a new technique for vision-based row tracking. Oksanen et al. (2005) used kalman filter for sensor fusion of integrated GPS, inertial sensor and odometer for agricultural vehicles. Subramanian et al. (2009) discussed a fuzzy logic enhanced Kalman filter for sensor fusion to guide an autonomous vehicle through citrus grove alleyways, where machine vision, laser radar, IMU and speed sensor is integrated with this system. A real time tractor position estimation system which consists of GPS and IMU is developed by Linsong et al. (2002), where kalman filter is used for sensor fusion. Iqbal et al. (2009) used a multisensor system including gyroscope and odometer to provide full 2D positioning solution in denied GPS environment, where kalman filter is used to predict and compensate the position errors of the multisensor system. Mizuhsima et al. (2011) developed a low-cost attitude sensor for agricultural vehicles by using least square method as a sensor fusion algorithm to estimate tilt angles (roll and pitch). Zhang et al. (2013) developed a prototype of guidance system equipped with RTK-GPS for rice-transplanter, where a kalman filter is used for the sensor fusion to estimate the posture of that vehicle.

1.1.4 Research on Tracked Vehicle Motion Model

Tracked vehicles are mainly used in the military services. Now it is using in civilian activities such as agricultural framing, forestry, building construction and mining etc. With high tractive effort, the application of tracked vehicles are increasing in these sectors though its high production cost, because it has low ground pressure which imposes less damage to the soil and requires no road construction, and now, the need to improve the performance capabilities of tracked vehicles which has forced to the designers, engineers and scientists to find a way to handle this task properly and

economically (Le, 1999). Motion of tracked vehicles over the ground is governed by the interaction between the soil and the tracks. Mathematical modelling of these interactions has been conducted by a number of authors (Bekker, 1962 & 1969; Wong, 1989), which have been recognized widely.

Kitano and Jyozaki (1976) developed motion equations for uniform turning to analyze and predict steering dynamics and steerability in plane motion of tracked vehicles. Kitano and Kuma (1977) also used tracked vehicles motion model to analyze of steering dynamics on level ground including track slippage, inertia force and the moment of inertia. Watanabe and Kitano (1986) developed a mathematical model to analyze the steering performance of articulated tracked vehicles on level ground. Janarthanan et al. (2011) developed a 5 DOF steering model of a tracked vehicle, and studied the handling behavior during non-stationary motion, when operating is at high and low speeds. Huh and Hong (2001) derived a modified 3 DOF dynamic model for tracked vehicle, which is utilized to estimate tractive force and track tension. Wong and Chiang (2001) derived a new theory which provides a unified approach to the study of the mechanics of skid steering for tracked vehicle. David and Wormell (2003 & 2004) used track vehicle model to analyze the fundamentals of tracked vehicle steering at low and high speed. Tehmoor and Raul (2010) estimated the soil slip and tracked coefficient based on the motion model for small scale robotic tracked vehicles. Shiller et al. (1993) used dynamic model to find out the trajectory of tracked vehicles on flat and inclined planes. Le et al. (1997) estimated the track-soil interaction parameters for robust autonomous guidance and control of a tracked vehicle.

1.1.5 Research on Path Planning of Agricultural Vehicles

When a robot vehicle is designed, four questions must be taken into account: what work has to be done, in which way the work has to be completed, which information is necessary and which positions must be measured (Murphy, 2000). In agricultural farming, the first answer is usually provided by the human operator and the last two are more or less solved from the measurement of field environments and positions based on environmental and positioning sensors. But the most difficult issue for the robot vehicle is the proper field operation, how to drive the robot in the field with more precision. Reid (2004) stated that proper path planning is one of the key tasks in the planning process. Field efficiency and operational costs with the use of high end technology is driven by the proper planning of field operation. The proper field operation reduces the production costs and increases the adoption of agricultural robots by the farmers (Rodrigo, 2012).

In general, a robot used a path planning algorithm which is capable to find a path from place A to B in order that no collisions occur with obstacles, and the path will be optimal with respect to a certain measure (Murphy, 2000). In agricultural robots, the task is usually to cover the whole field, not only going from place A to B, and this kind of path planning is not directly suitable in the agricultural field. Researchers are continually working to develop a working route for agricultural robots that can cover the whole field of crop. For instance, Taïx et al. (2006) derived a field coverage algorithm for convex polygonal fields which is one vertex of concavity, and the field is divided into a working area and a turning area. Non-convex fields with large obstacles are subdivided along the boundary segments defined by the concave vertices. Hofstee et al. (2009) developed a tool in determining of an optimum path for field operations in single convex fields. The field is split into subfields based on the

longest side of the field or the longest segment of a field polygon (Stoll, 2003). Acar et al. (2002) described the cellular decompositions of a field in various patterns for path planning between two points, and to cover the free space. Oksanen and Visala (2007) developed a higher level algorithm based on the trapezoidal split of a complex shaped field plot to smaller parts. Willigenburg et al. (2004) proposed an on-line kinematic minimum time path planning for an industrial fruits picking robot which is controlled in the presence of obstacles. Bochtis et al. (2015) developed a route planning method for a deterministic behavior robot based on the adaption of an optimal area coverage method developed for arable farming operations, which generates route plans for intra- and inter-row orchard operations. Hameed et al. (2016) developed a novel side-to-side 3D coverage path planning method which ensures zero skips/overlaps regardless of the topographical nature of the field terrain and saves a significant percentage of uncovered area if an appropriate driving angle is chosen. Driscoll (2011) derived an algorithm for solving the optimal complete coverage problem on a field boundary with n sides. Jin and Tang (2010) reported a path planning algorithm based on a developed geometric model for generating an optimized full coverage pattern for a given 2D field by using Boustrophedon paths.

1.2 Research Motivation and Objectives

A Yanmar AG1100 model combine harvester was converted to a robot (called robot combine harvester) which is instrumented by the global and local sensors under the vehicle robotics laboratory, Hokkaido University, Japan (Zhang et al., 2013; Zhang, 2014; Choi, 2014) which is successfully running in summer season in the field to harvest the cereal crops like paddy, wheat and soybean. Before harvesting of these crops, the outer crops near to headland is cut twice or thrice by manual driving of the robot combine harvester to confirm safe turning of robot combine harvester

throughout the field. After then, each corner position is measured by the operator with fixing a portable computer connected to a RTK-GPS system on the back pack and log this position as A, B, C, D etc in that computer, and for better understanding this position is shown in figure 1-3. Now the position A and B is called the start point and end point which are inputted into a path planning software developed by the vehicle robotics laboratory for a robot combine harvester to make a harvesting map of crops for the robot combine harvester. Finally, this map is inputted to the navigation software for the operation of robot combine harvester.

But in this method, there are some problems arising during real time harvesting of wheat or paddy, especially if the crop pattern is not row. Firstly, when we cut the surrounding crops near to headland, the remaining crop periphery will be curved or meandering rather than straight as shown in figure 1-3. Path planning based on the corner position A and B, the robot combine harvester is run to harvest the crop, but after harvesting it has been seen that the curved or meandering crop portion is not harvested. This curved or meandering crop portion leaves in the field during harvesting which indicates the crop losses. Secondly, the corner position is taken by walking along the surrounding periphery of crop, which is time consuming. This time depends on the size of crop field. For large field, the time will be more than small field. Thirdly, the path planning on the basis of A and B position for the robot combine harvester is only suitable for a rectangular polygon field. But if the field shape is a convex polygon or a concave polygon other than rectangular polygon, this method is not working properly.

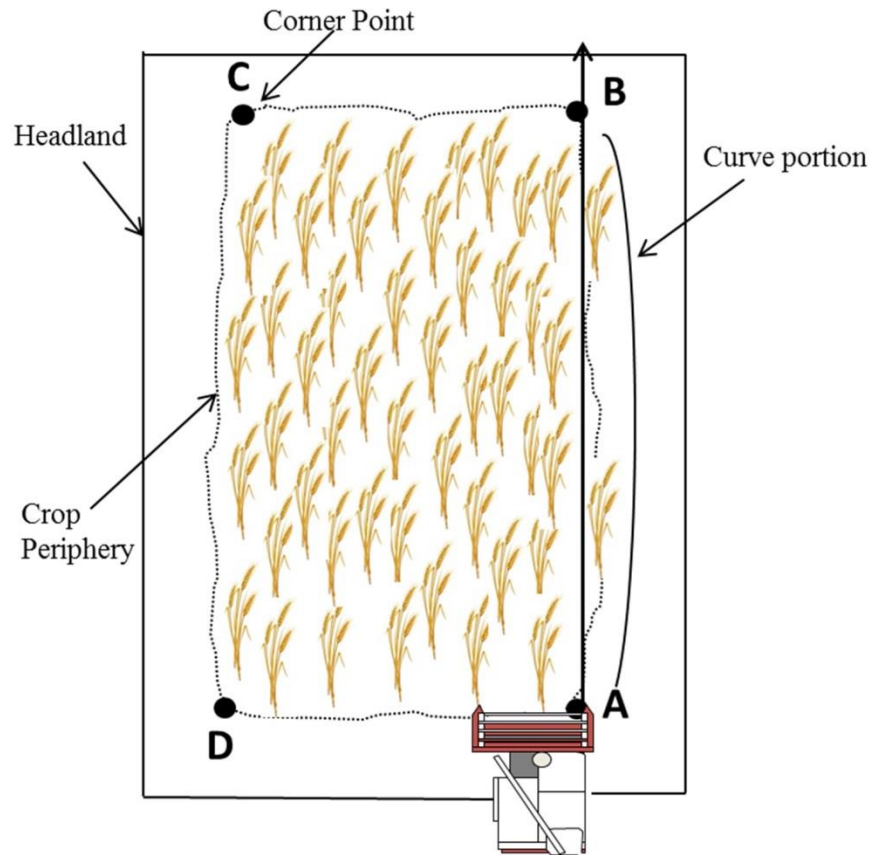


Figure 1-3. Schematic of the corner vertices determined conventionally and the curve or meandering portion

From the above addressing problems, it may be solved by the following specific objectives which are described in detailed in chapter 5.

1. To obtain the measured position and heading of the robot combine harvester during the cutting of surrounding crops twice or thrice near to headland.
2. To estimate the header end position/the crop periphery by using the measured position and heading of the robot combine harvester.
3. To use a convex hull method to calculate the exact outline of crop periphery by reducing the point clouds.

4. To use the rotating caliper method for finding out the optimum harvesting area for a rectangular field.
5. To develop an algorithm for finding out the optimum harvesting area if the field shape is convex polygon.
6. To develop an algorithm for finding out the optimum harvesting area if the field shape is concave polygon.
7. To calculate the harvesting map of crop based on the optimum harvesting area of a convex polygon or a concave polygon field.

Another problem describes in this dissertation which happens by using inertial measurement unit (IMU) to measure heading of the robot combine harvester for calculating the header end position/the crop periphery. In the tracked combine harvester, turning is done at high speed and high steering command or small turning radius. During turning of the robot combine harvester in the corner of crop periphery, the yaw rate gyro measurement from IMU will be erroneous measurement like bias, and the heading will be the integration of that yaw rate gyro measurement which contains the drift error. In that case, the exact heading measurement of the robot combine harvester is difficult into the corner position. Due to compensate yaw rate gyro measurement bias for estimating the absolute heading, the following objectives are considered, which are discussed in detailed in chapter 3 and 4.

1. To develop a tracked combine harvester dynamic model based on the RTK-GPS and IMU sensor measurements.
2. To use a sensor fusion method like extended kalman filter for estimating the absolute heading by using the tracked combine harvester dynamic model.

Chapter 2 Research Platform, Materials and Methods

2.1 Introduction

This chapter introduces the research platform, sensors, sensor fusion method and field optimization methods, which are used throughout the research. Section 2.2 shows the original looks of a robot combine harvester and its detail specifications, which can be operated by manual mode or by automatic mode. The global positioning system and inertial measurement unit is used to provide useful information to the robot combine harvester for autonomous purposes which is also introduced in section 2.3. Kalman filter, convex hull and rotating caliper method discussed in section 2.4, which are used for reducing sensor uncertainties, and for the optimization of crop field.

2.2 Research Platform

2.2.1 Tracked Combine Harvester

A Yanmar AG1100 model combine harvester provided by the Yanmar Co., Ltd is used as a research platform in the chapter 3 to 5, which was designed to harvest for the paddy and wheat crops. This combine harvester can also work for soybean and other crops when cutting header is changed. Figure 2-1 shows the original look of the tracked combine harvester with a general-purpose header, which has 110 Horsepower (hp) or 80.9 kW output and 2500 rpm engine rotation speed. In order to prolong its working time, a 110 L diesel tank is equipped sothat the tracked combine harvester can work continuously for a whole day. More detailed specifications are discussed in Table 2-1.



Figure 2-1. A Yanmar AG1100 model combine harvester

In order to modify a robot combine harvester, a control pc is integrated with some sensors and safety devices such as RTK-GPS, IMU, laser scanner and emergency stop controllers. The robot combine harvester can work in both Manual Mode and Automatic Mode. In automatic mode, the driving part can be fully controlled by the robot, which includes the going forward and backward, left or right steering or any combination of these operations. The safety system of the robot combine harvester can also be controlled in Automatic Mode. The driving commands should be sent to the combine harvester within every 200 milliseconds; otherwise the combine harvester will stop and make a sound alarm. The overall controlling architecture of the robot combine harvester is given in figure 2-2.

Table 2-1. Specifications of Yanmar AG1100 Combine Harvester (Source: Zhang, 2014)

Combine Harvester Specifications	
Dimensions:	
1. Overall Length	6150 mm
2. Overall Width	2350 mm
3. Overall Height	2760 mm
4. Weight	4610 kg
Engine:	
1. Volume	3.053 L
2. Max Output	80.9 kW
3. Max Rotation	2500 rpm
4. Fuel Type	Diesel
5. Fuel Tank Volume	110 L
Crawlers:	
1. Overall Length	1780 mm
2. Overall Width (Each)	500 mm
3. Distance	1185 mm
4. Transmission	Full Time Drive System
5. Travelling Speed	-2 m/s ~ 2 m/s
Header:	
1. Divider Width	2060 mm
2. Cutter Width	1976 mm
3. Cutting Range (Height)	-100 mm ~ 1000 mm
4. Reel Radius × Width	1000 mm × 1915 mm
5. Rotation Speed	Synchronized with Crawler
Grain Tank:	
1. Volume	1900 L
2. Unloading Height	5100 mm

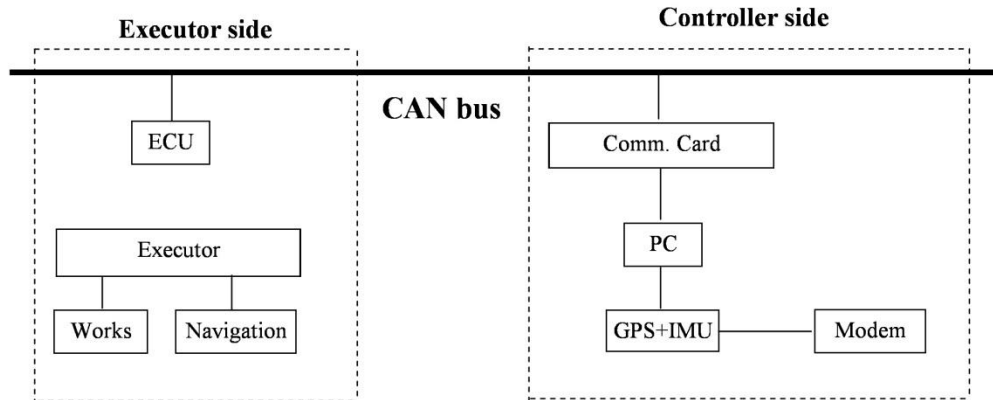


Figure 2-2. Overall controlling architecture of a robot combine harvester (Source: Zhang, 2014)

According to controlling architecture, the control pc is connected to the Control Area Network (CAN bus) by using a communication interface. This control pc can send commands to or receive feedback from the combine harvester through the interface. The GPS and IMU sensors are connected to this control pc with a RS232 serial port and USB port. An emergency stop controller is used to connect directly to the combine harvester's control system, which enables to provide an immediate stop of the machine in case of emergency. In addition, an electronic control unit (ECU) is fixed between the control pc and the combine harvester's actuators which is used to serve as a guard to the machine; and which can shield all wrong CAN messages and commands from the control pc. This ECU can also filter unnecessary messages on the CAN bus, that are not related to navigation and field work.

2.3 Research Materials

2.3.1 RTK-GPS

The Global Positioning System (GPS) is a space-based radio navigation system developed by the U.S. Department of Defense starting in the 1970s as military system (Parkinson and Spilker, 1996). It is also called a global navigation satellite

system which provides geolocation and time information to a GPS receiver anywhere on or near the Earth, where there is an unobstructed line of sight to four or more GPS satellites. This GPS technology provides critical positioning capabilities to military, civil, and commercial users around the world.

For producing GPS position, a GPS receiver is used to receive signals from at least four satellites. These GPS signals are obtained by using an antenna, which is converted to digital timing signals and satellite orbital data used to calculate the user's position. The GPS accuracy is affected by a number of error sources, where some of these errors are corrected by the use of differential GPS (DGPS) and other errors are uncorrectable. The most uncorrectable GPS error sources are caused by the receiver and antenna design, and multipath interference in the user's local environment, whereas the most DGPS-correctable errors are ionosphere-induced signal distortions, satellite timing errors, and satellite ephemeris errors. The GPS errors also depend on the method of differential correction. The relative errors of a GPS generally may grow with the time of observation (Jorge and Arthur, 2009).

RTK is a Global Navigation Satellite System (GNSS) technique which is used to enhance the precision of positioning data derived from satellite-based positioning systems such as GPS, GLONASS, Galileo and BeiDou. It uses carrier-based ranging rather than code-based positioning, and relies on a single reference station to provide real-time corrections. It provides centimeter-level accuracy which is often required in the several applications such as land survey, hydrographic survey and in consumer unmanned aerial vehicle navigation. The GPS signal is converted to a usable RTK signal for reducing and removing common errors.

In code-based positioning, GPS receiver provides its position from the correlation with four or more satellites determining their ranges. With using these ranges and the position of satellites, the GPS receiver can derive its position within a few meters. Moreover, the carrier-based ranging calculates the range by determining the number of carrier cycles between the satellites and the rover station, and this number is multiplied by the carrier wavelength, which results in more precise positions than those derived by code based positioning (TerrisGPS, 2016).

RTK-GPS consists of a base station, which monitors the signals coming from the satellites as shown in figure 2-3. One or several rover users receive information from the base station, and a communication channel with which the base station broadcasts correction data to the users in real time. RTK-GPS delivers highly accurate positioning information within the vicinity of base station. For computing an RTK solution, satellite measurements are sent from a fixed reference station to receivers nearby. By combining satellite measurements with those of the reference station, whose exact location is well known, which removes common errors such as ionosphere errors, satellite clock errors etc. Once these errors have been removed, it will use the phase measurements to determine an exact position within 2–5 centimeters.

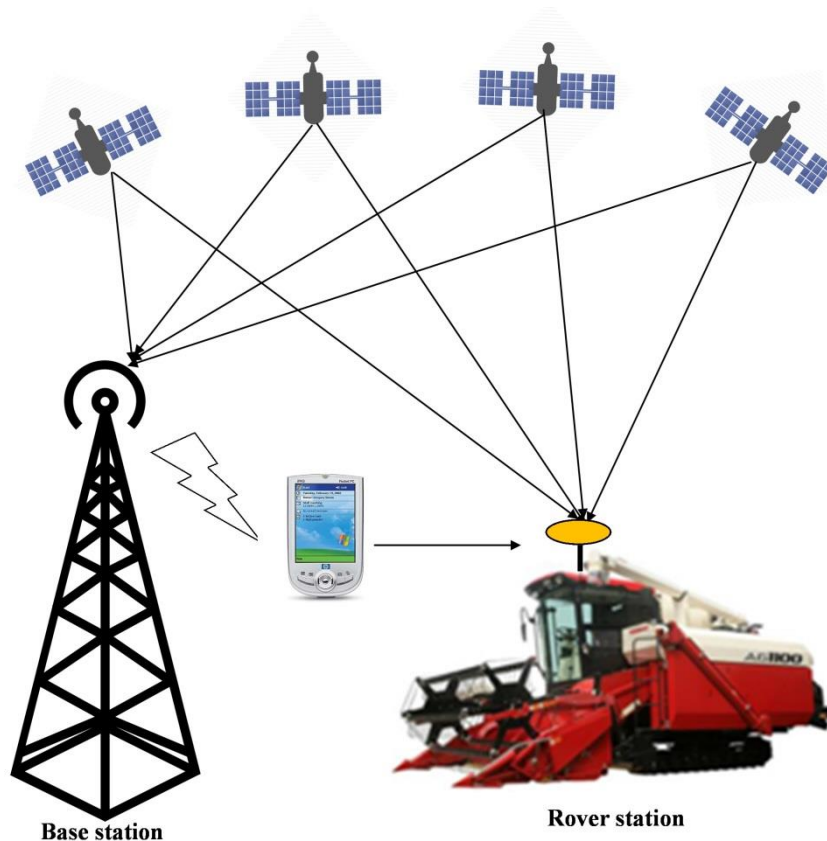


Figure 2-3. Schematic view of Virtual Reference Station (VRS) for RTK-GPS position

The use of RTK-GPS is most suitable where a large number of unknown points are tried to determine within the vicinity of known base station, and where the coordinates are required in real time. It is also important, when the line of sight from the base station to the rover users is relatively unobstructed. RTK-GPS position accuracy will decrease as the distance increases between the reference station and the rover receivers, and the recommended distance limit is considered between 20 and 30 kilometers. A significant amount of position accuracy will be lost, where the distance is greater than 30 kilometers (TerrisGPS, 2016).

In this research, a RTK-GPS receiver (Topcon Co., Ltd) as shown in figure 2-4 was used to measure the position of robot combine harvester where the GEONET is

used as the Virtual reference station (VRS). The specifications of RTK-GPS are given in Table 2-2. The specifications state that the RTK-GPS data can be logged at 20 Hz update rate via RS232 serial port.



Topcon GB-3 Receiver



Topcon PG-S1 Antenna

Figure 2-4. Real view of Topcon RTK-GPS receiver and antenna

Table 2-2. Specifications of RTK-GPS receiver

Technical Specifications of Receiver	
Tracking:	
1. Signals	GPS/GLONASS L1/L2/L5 C/A and P Code & Carrier, WAAS/EGNOS/MSAS
2. Channels	72 universal
3. Multipath reduction	C/A code phase and carrier phase
4. Time to First Fix (50%)	Hot < 10 sec, Warm < 35 sec, Cold < 60 sec
5. Reacquisition	< 1sec
Position Accuracy:	
1. Standalone	H: 2 m (CEP), V: 3 m (CEP)
2. Static	H: 3 mm + 0.5ppm V: 4 mm + 1.0ppm
3. RTK Kinematic	H: 10 mm + 1.0ppm V: 15 mm + 1.0ppm

4. DGPS (RTCM based)	Horizontal 0.4 m (CEP) Vertical 0.6 m (CEP)
5. Velocity	0.02 m/sec (CEP)
Data Features:	
1. Data Formats	Proprietary (TPS) data format, NMEA 0183 versions 2.x and 3.x,RTCM SC104 versions 2.x and 3.x, CMR/CMR+, BINEX
2. Update and output rates	Up to 20 Hz
Physical Characteristics	
1. Dimensions	240 x 110 x 35 mm (W x H x D)
2. Weight	0.6kg
3. Color	Topcon Urban Yellow and Black

Table 2-3. Specifications of RTK-GPS antenna

Technical Specifications of Antenna	
Operating Frequency Range	
1. L1 GPS/GLONASS	1586.5 ± 25MHz
2. L2 GPS/GLONASS	1236 ± 20MHz
3. L-Band	1535 ± 10MHz
Out of Band Rejection	
1. L1	± 100 MHz -30 dBc (typical)
2. L2	± 200 MHz -60 dBc (typical)
Connector and Mounting	
1. Antenna Connector	TNC
2. Mount	5/8-11 UNC-2B thread
Physical Characteristics	
1. Dimensions	141.6 (W) x 141.6 (H) mm x 54.2 (L) mm
2. Diameter	200 mm (with ground plane)
3. Weight	430 g (without ground plane) 615 g (with ground plane)

2.3.2 IMU

An inertial measurement unit (IMU) is an electronic device which consists of a combination of accelerometers, gyroscopes and magnetometers, which measures and reports a vehicle body's specific force, angular rate, and the magnetic field surrounding the vehicle body. The integration of IMU allows a GPS receiver to work when GPS-signals are unavailable, such as in tunnels, inside buildings, or when electronic interference is present. IMU works by detecting linear acceleration and rotational rate using one or more accelerometers or gyroscopes, where a magnetometer is commonly used as a heading reference. Its typical configurations contain one accelerometer, gyroscope, and magnetometer per axis for each of the three vehicle axes such as pitch, roll and yaw (Wikipedia, 2017).

In land vehicles, an IMU can be integrated into GPS based autonomous navigation systems or vehicle tracking systems, getting the system a dead reckoning capability and the ability to gather as much accurate data as possible about the vehicle's current speed, turn rate, heading, inclination and acceleration, in combination with the vehicle's wheel speed sensor output and reverse gear signal if available, for purposes such as better traffic collision analysis (Wikipedia, 2017). In a navigation system, the data of the IMU is fed into to a control PC, which calculates its current position based on velocity and time.

A major demerit of using the IMU for navigation is that it typically suffers from accumulated error. Because, the navigation system is continually adding detected changes to its previously calculated positions, any errors in measurement, however small, accumulate from point to point. This leads to 'drift', or an ever-increasing difference between where the system thinks it is located and the actual location. Due to accumulation error, the IMU can be used with the positional tracking

system such as GPS in a navigation system (Zhang, 2017). Since, the IMU measures the relative heading angle with a high accuracy, which is usually integrated with the RTK-GPS mentioned above using fusion algorithms to acquire the absolute heading of the vehicle. An IMU fused with RTK-GPS (Nagasaka et al., 2004; Takai et al., 2014; Yang et al., 2016) can provide the position data at a high accuracy.



Figure 2-5. Real view of Inertial Measurement Unit (IMU)

In this research, VN-100 IMU as shown in figure 2-5 is a miniature, high-performance Inertial Measurement Unit (IMU) and Attitude Heading Reference System (AHRS) which is used to measure the vehicle's heading angle and angular rate. Incorporating the latest MEMS sensor technology, the VN-100 IMU combines with 3-axis accelerometers, 3-axis gyros, 3-axis magnetometers, a barometric pressure sensor and a 32-bit processor. Along with providing calibrated sensor measurements, the VN-100 IMU also computes and outputs a real-time 3D orientation solution which is continuous over the full 360 degrees of motion (Vectornav, 2017). Table 2-4 shows the detailed specifications of VN-100 IMU which can measure the angular rate within

the range of 2000 deg./s. It also can measure pitch angles within the range of 90 deg., while yaw and roll angle is 180 deg. The digital output signal was sent to the vehicle control pc at a frequency of 400 Hz/1 kHz through a USB serial port.

Table 2-4. Specifications of Inertial Measurement Unit (IMU)

Technical Specifications	
Attitude & Heading:	
1. Range (Heading/Roll)	±180 °
2. Range (Pitch)	±90 °
3. Static Accuracy (Heading, Magnetic)	2.0 ° RMS
4. Static Accuracy (Pitch/Roll)	0.5 ° RMS
5. Dynamic Accuracy (Heading, Magnetic)	2.0 ° RMS
6. Dynamic Accuracy (Pitch/Roll)	1.0 ° RMS
7. Angular Resolution	< 0.05 °
8. Repeatability	< 0.2°
9. Output Rate (IMU Data)	1 kHz
10. Output Rate (Attitude Data)	400 Hz
Gyro:	
1. Range	±2000 °/s
2. In-Run Bias Stability	< 10 °/hr
3. Linearity	< 0.1 % FS
4. Noise Density	0.0035 °/s /√Hz
5. Bandwidth	256 Hz
6. Alignment Error	±0.05 °
Accelerometer:	
1. Range	±16 g
2. In-Run Bias Stability	< 0.04 mg
3. Linearity	< 0.5 % FS
4. Noise Density	0.14 mg/√Hz
5. Bandwidth	260 Hz
6. Alignment Error	±0.05 °
Magnetometer:	

1. Range:	±2.5 Gauss
2. Linearity:	< 0.1 %
3. Noise Density:	140 µGauss/√Hz
4. Bandwidth:	200 Hz
5. Alignment Error:	±0.05 °
Pressure Sensor:	
1. Range:	10 to 1200 mbar
2. Resolution:	0.042 mbar
3. Accuracy:	±1.5 mbar
4. Error Band:	±2.5 mbar
5. Bandwidth:	200 Hz
Environment:	
1. Operating Temp	-40°C to +85°C
2. Storage Temp	-40°C to +85°C
Physical Characteristics	
1. Size	36 x 33 x 9 mm
2. Weight	15 g
3. Interface	10-pin Harwin

2.4 Research Methods

2.4.1 Kalman Filter

Kalman filter is an algorithm developed by Rudolf E. Kalman that uses a series of measurements including statistical noise and other inaccuracies observed over time, and produces estimates of unknown variables which is more accurate than those based on a single measurement alone, by using Bayesian inference and estimating a joint probability distribution over the variables for each time frame (Wikipedia, 2017).

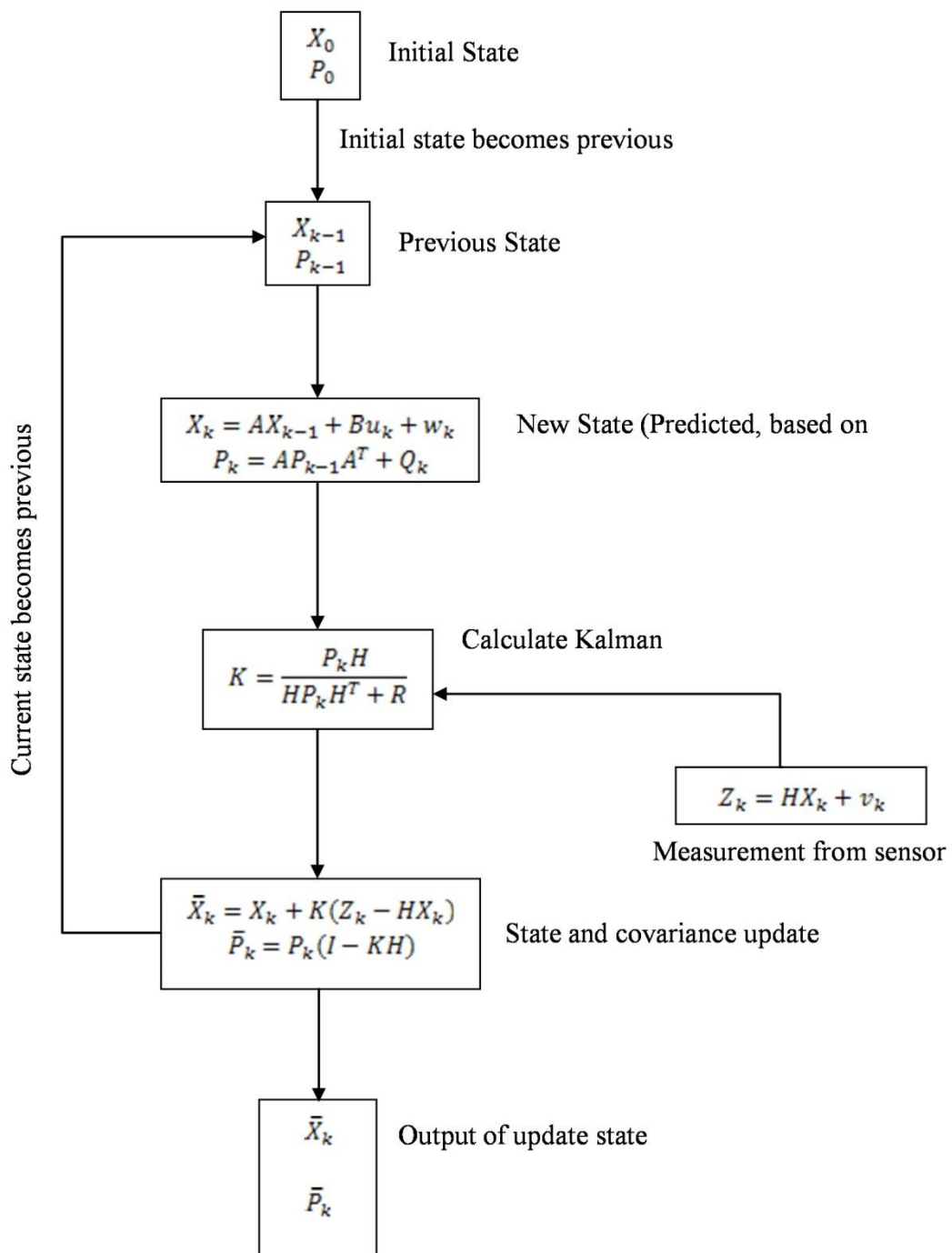
Kalman filter has a numerous applications such as for guidance, navigation, and control of ground vehicles, and for aircraft and spacecraft. It is widely applied

concept in time series analysis, which is used in the field of signal processing. It is also important in the field robotics motion planning and control, which is sometimes used for trajectory optimization. The kalman filter does not take any assumption, and the errors are Gaussian which is a statistical noise having a probability density function (PDF) equal to that of the normal distribution known as the Gaussian Distribution.

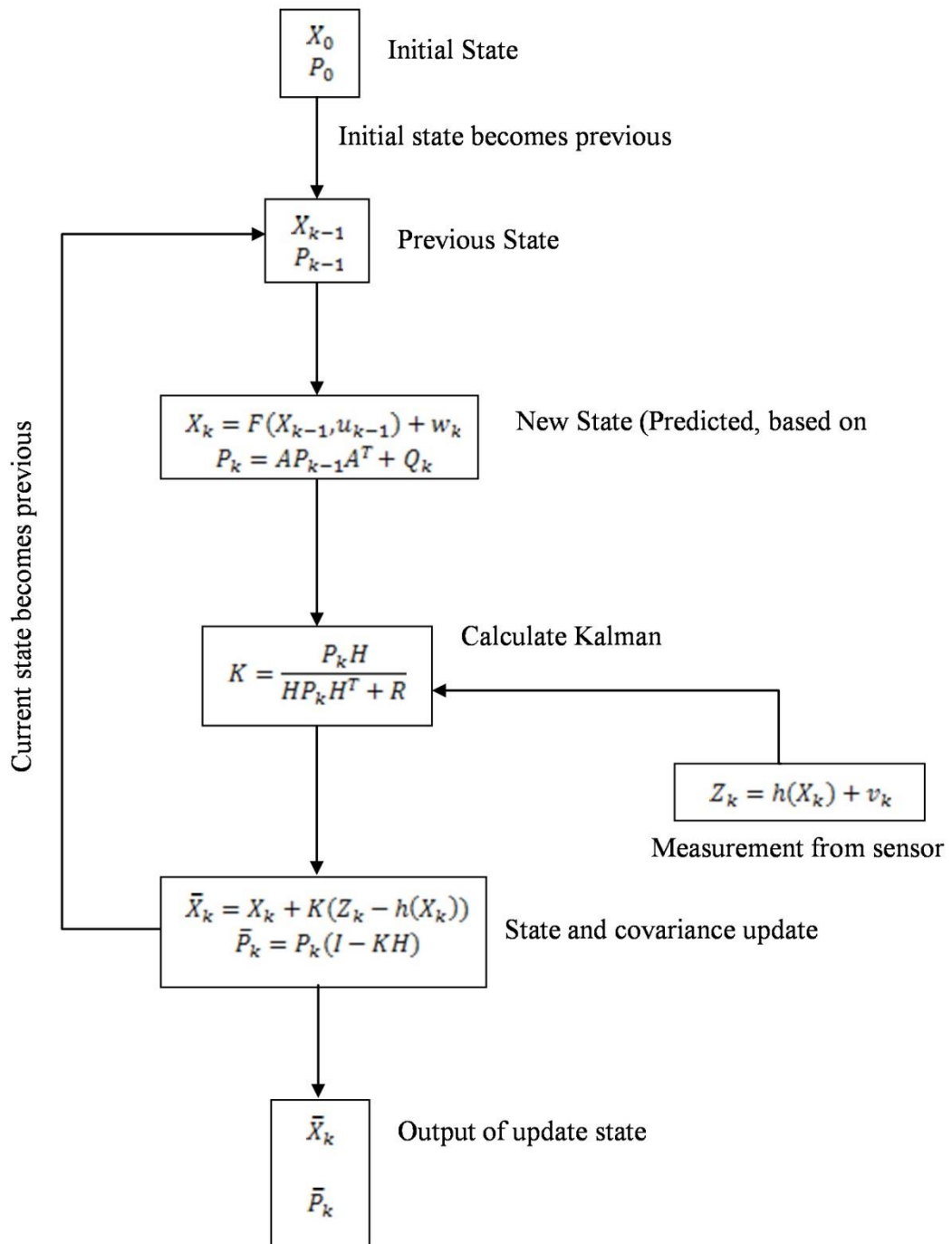
Kalman filter uses a system's dynamic model with known control input and multiple sequential measurements from sensors to form an estimate state which is better than the estimate obtained by using only one measurement alone; which is the common fact of sensor fusion and data fusion algorithm. This filter algorithm is divided into two steps, of which one is prediction step and another is measurement. In prediction step, the state is predicted from the previous epoch with the vehicle motion model. In the correction step, the predicted state is corrected with observation model sothat the error covariance of the estimator is minimized. Extensions and generalizations of the kalman filter are extended kalman filter and unscented kalman filter, which works in nonlinear condition.

The kalman filter cycle contains a series of equation depicts as shown in figure 2-6 (a). Initial state contains state matrix and initial process covariance matrix, where the state matrix indicates positon and velocity. The initial state is also called the previous state. The new state is predicted based on the vehicle motion model and previous state. Kalman gain is a residual fraction that is calculated between the estimated predicated new state and actual sensor measurements, and it is an important element, which indicates as regulator to update a new state from the predicated state and the actual sensor measurements. The output of kalman filter is the updated new state which is called the current state. To continue this cycle, the current state will be

the previous state. Similarly in extended kalman filter cycle as shown in figure 2-6 (b), the only variation is the estimated new state based on the previous state. A nonlinear state space model is used, which is linearized by the Taylor series expansion. A Jacobian matrix is introduced in update step for the extended kalman filter. In chapter 4, the extended kalman filter is used due to non-linear dynamic model for the tracked combine harvester.



(a) Kalman Filter Cycle



(b) Extended Kalman Filter Cycle

Figure 2-6. Overview of Kalman Filter and Extended Kalman Filter Cycle

The notations used in kalman filter cycle in figure 2-6 are as follows:

A, B = Adaptation matrices, to convert input state to process state	K =Kalman gain
$F(X, u)$ =Non-linear state transition matrix. A function of the state and control variables.	$h(X)$ =Non-linear measurement matrix
Q =Process noise covariance matrix. Keeps the state covariance matrix from becoming too small or going to 0.	R = Sensor noise/measurement covariance matrix
Z =Measurement of state	X =State matrix
u =Control variable matrix	H =Conversion matrix (to make sizes consistent)
v =Measurement noise	P = Process covariance matrix (represents error in the estimate)
w =Predicated state noise matrix	I = Identity matrix

2.4.2 Convex Hull Method

The convex hull of a set P of points in the Euclidean plane or in a Euclidean space is the minimum area of convex region, which contains every point (Sedgewick and Wayne, 2011). Formally, the convex hull is defined as the intersection of all convex sets containing P or as the set of all convex combinations of points in P . For example, when P is considered a set of points in the plane, imagine this set enclosed

by a rubber band which is stretched around P. When the band is released, it will make the shape of convex hull as shown in figure 2-7 (Shamos, 1978; de Berg et al., 2000). This method is used in problem findings of practical application in robot motion planning, pattern recognition, image processing, geographic information system (GIS) and construction of phase diagrams. It is also a tool, which considers a building block for a number of other computational-geometry such as the rotating calipers method for calculating the width and diameter of a point set (Wikipedia, 2017).

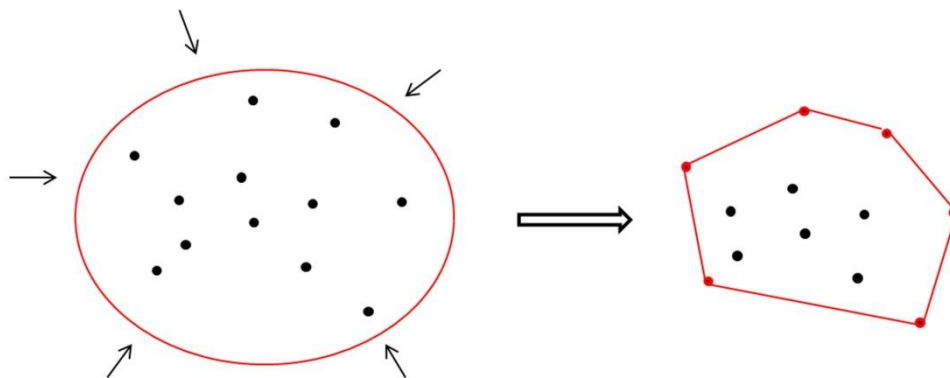


Figure 2-7. Convex hull of a finite set P assumed by a rubber band

An algorithm is described based on incremental approach to the convex hull problem used in chapter 5. Consider, convex hull of a set of points Q in figure 2-8 is the smallest convex polygon P for which each point of Q is either on boundary of P or inside it. It is expressed by the convex hull $CH(Q)$. There have some methods used to make a convex hull, of which an Incremental method is used to make a convex hull from a finite set of RTK-GPS position. The point set Q is sorted in clockwise to create a sort sequence (p_0, p_1, \dots, p_i) in figure 2-8 (a).

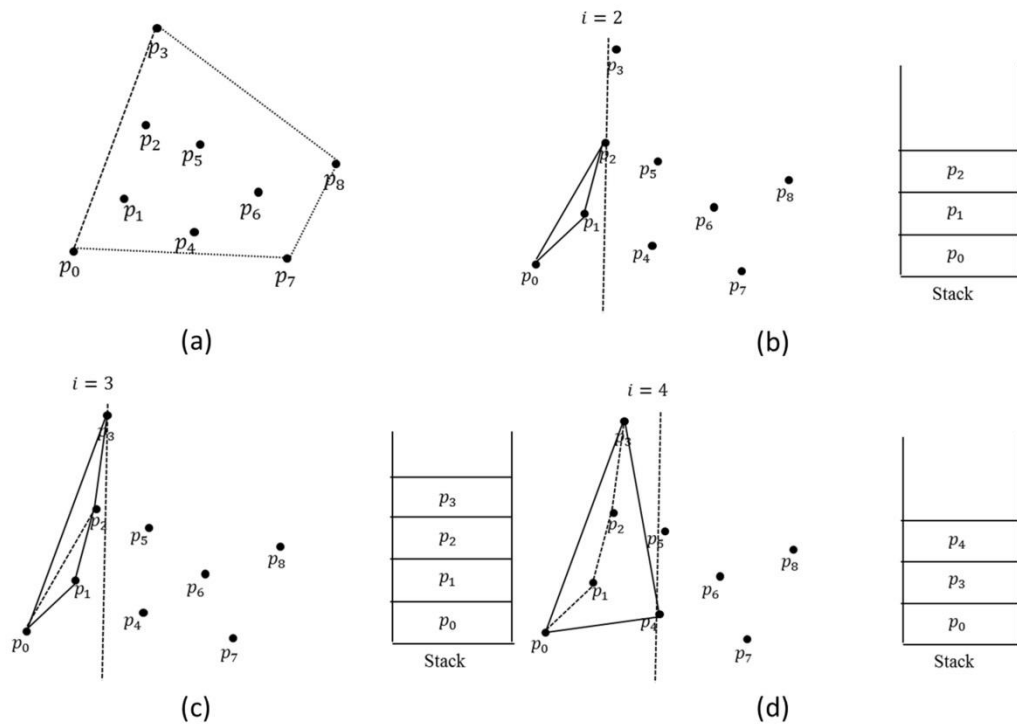


Figure 2-8. Schematic representation of incremental convex hull method (a. sorting of points cloud, b. convex hull when $i = 2$, c. convex hull when $i = 3$, d. convex hull when $i = 4$)

Firstly, three points are selected consecutively from the smallest sort sequence, such as p_0, p_1 and p_2 , and make a new convex hull $CH(p_0, p_1, p_2)$ which is stored in the stack in figure 2-8 (b). Secondly, the next point p_3 is selected to make a tangent to the convex hull $CH(p_0, p_1, p_2)$, and find the edge of convex hull $CH(p_0, p_1, p_2, p_3)$. As the contact point is one of the vertex of the convex hull at that time, it examines whether it is all contacts in the order stacked on the stack. After that, the line segment is removed from the convex hull $CH(p_0, p_1, p_2, p_3)$ in figure 2-8 (c). Thirdly, p_1 and p_2 are excluded from the stack when the next point p_4 is selected as shown in figure 2-8 (d). To continue these procedures, an i^{th} first convex hull $CH(p_0, p_1, p_3, \dots, p_i)$ is created from the left to the i^{th} stage.

Although, each element of the convex hull $CH(p_0, p_1, \dots, p_i)$ selected by the incremental method indicates that it is the vertex of the convex hull, and it is also unknown which point can combine to create convex hulls. A method is used for solving this problem as shown in figure 2-9. The point set is divided into two regions with the start point and the end point of the sorted stack column as the boundary, and the two convex hulls at the top and the bottom are obtained by incremental method. The stack S_1 and S_2 stores the vertices of the upper and lower convex hull. The vertices of convex hull are counted from left to right along the horizontal X coordinates. The vertices in the stack S_2 is a reverse order combined with the stack S_1 . The vertices of the convex hull are counted in the clockwise direction.

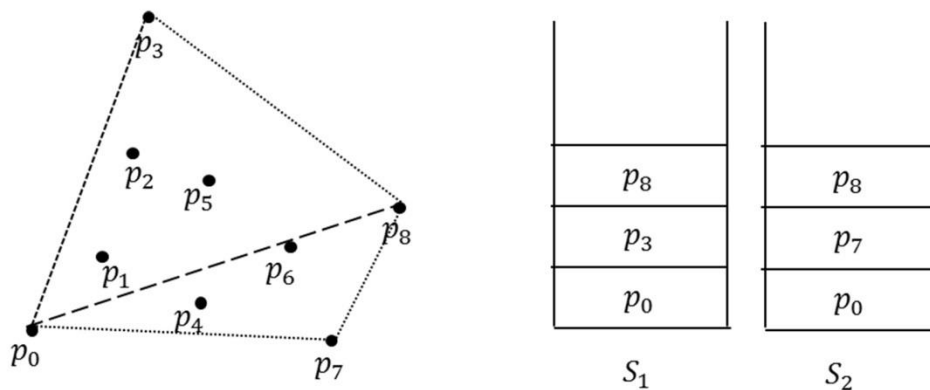


Figure 2-9. Division of convex hull for upper and lower hull

2.4.3 Rotating Caliper Method

A rotating caliper method in computational geometry is an algorithm design technique, which is used to solve optimization problems including finding the width or diameter of a set of points (Wikipedia, 2017). It resembles the idea of rotating a dynamically adjustable caliper around the outside of a convex polygon.

Rotating caliper method developed by Shamos (1978) is used for computing the width or diameter of a convex polygon $P = (p_1, p_2, \dots, p_n)$. The diameter is considered as the longest line segment drawn between parallel lines across through P . There are two parallel lines passing through a pair of vertices p_i and p_j in figure 2-10 (a), which is represented at diametrically opposed direction. This method generates all $O(n)$ antipodal pair of vertices and chooses the longest line segment called the diameter. Two antipodal vertices p_i and p_j with the X axis is selected as the initial direction. In order to find out the next antipodal vertices, the angles θ_i and θ_j are considered by $p_i p_{i+1}$ and $p_j p_{j+1}$ with parallel lines. When $\theta_j < \theta_i$, the parallel lines are rotated by θ_j and p_{j+1}, p_j which becomes the next antipodal vertices. This procedure is continued until the initial position comes. When $\theta_i = \theta_j$, three new antipodal vertices are generated.

The smallest area enclosing rectangle determined based on Freeman and Shapira (1975) theorem from the rotating calipers algorithm (Shamos, 1978; Godfried, 1983). $L_s(p_i)$ is defined as a straight line orthogonal to the tangent of the vertex p_i . $L(p_i, p_j)$ is indicated as a straight line passing through p_i and p_j . The first step is to select the vertices with minimum or maximum X and Y coordinates. These vertices are denoted by p_i, p_j, p_k and p_l as shown in figure 2-10 (b). $L_s(p_j), L_s(p_l)$ rotates to make the first set of calipers in the X direction. For the second set of calipers, $L_s(p_i), L_s(p_k)$ rotates it orthogonally with the first set. This process is repeated until the end. This is a line algorithm that changed from 2 points to 4 points, and consider four angles $\theta_i, \theta_j, \theta_k$ and θ_l . Let consider $\theta_i = \min\{\theta_i, \theta_j, \theta_k, \theta_l\}$. Now the four straight lines are rotated by an angle θ_i , and one side of the rectangle is determined when $L(p_i, p_{i+1})$ is common to p_i, p_{i+1} . The corners of the rectangle can be computed from

the coordinates of p_i, p_{i+1}, p_j, p_k and p_l . Then another vertex is uniquely determined. By repeating this procedure for all sides of the polygon it is possible to determine a rectangle with the smallest area.

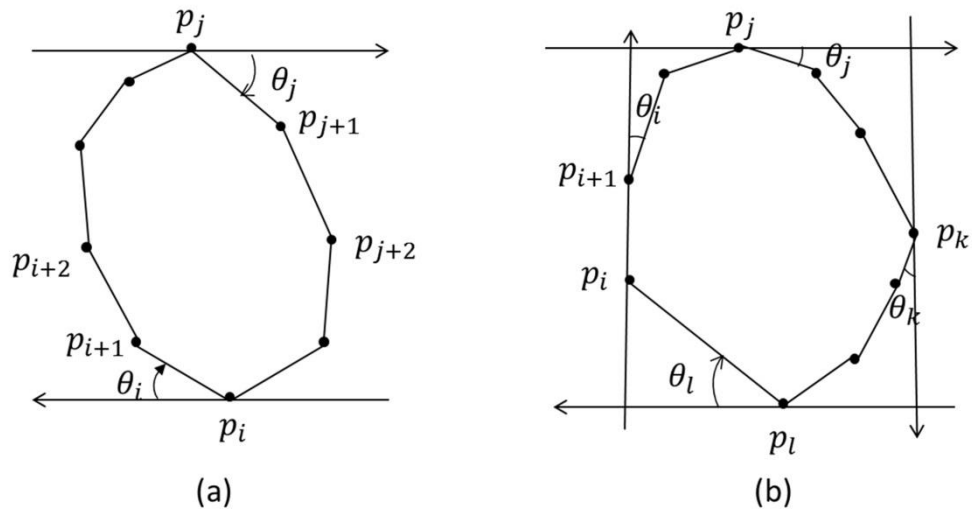


Figure 2-10. Estimation of a rectangle using Rotating Calipers method

2.5 Conclusions

The robot combine harvester, global positioning system and inertial measurement unit in this chapter is considered as a prime research platform and materials, based on these, the research was designed which is discussed in the chapter 3 to 5. The sensor fusion method like kalman filter is used in chapter 4 for compensating the sensor uncertainties. In chapter 5, the convex hull method and rotating calipers method are used to find out the optimum harvesting area of a crop field.

Chapter 3 Tracked Motion Model for Tracked Combine Harvester

3.1 Introduction

Nowadays, the application of tracked vehicles is increasing in agricultural sector because it has low ground pressure which imposes less damage to the soil. It is also better than wheel vehicle in order to larger contact area of tracks, which provide better floatation and traction at various terrains. That why tracked vehicle is now considered for autonomous purposes in off-road mobility. In autonomous application, it is necessary to use a modern sensor techniques and tracked vehicle motion model.

Tracked vehicle motion model play important in determining the vehicle state, heading of vehicle, sensor uncertainties compensation to control an autonomous off-road tracked vehicle. Mathematical modelling of the tracked vehicle has been conducted by some authors. Of particular note, Wong (2008) and Kitano & Jyozaki (1976) has been developed tracked vehicle motion model to account track-soil interaction parameters at different terrain condition. Real time estimation of tracked vehicle state, soil parameter and track coefficients based on the tracked vehicle motion model is required in achieving precise, robust autonomous guidance and control of tracked vehicles.

In modelling of tracked vehicle model, soil parameter and track coefficients play an important role in determining the maximum track forces and moment of turning resistance developed by the tracked vehicles, which is a little bit difficult to

measure or estimate. A few researches have been done to estimate the soil parameter and track coefficients by using the theoretical and statistical methods. Le et al. (1997) and Tehmoor & Raul (2010) described a method for estimating the slip over terrain with a statistical method from the vehicle trajectory data, and sideslip angle for a tracked vehicle in real time. Wong (2008) and Kitano & Kuma (1977) described a methodology for calculating track coefficient for small to large scaled tracked vehicle over a terrain. Tehmoor & Raul (2010) also established a method to estimate tracked coefficient of lateral and longitudinal with statistical method using the tracked vehicle kinematic and dynamic model for a different terrain, and this result confirmed the dependence of track coefficient of friction on vehicle turning radius and velocity (Al-Milli et al., 2007). As the turning radius is a vital parameter for turning maneuverability which can be estimated theoretically from the vehicle speed and angular velocity by using tracked vehicle kinematic model (Wong 2008; Kitano & Jyozaki, 1976). In this chapter, the above parameters are computed directly from the tracked vehicle controlling parameters, position and direction of vehicle combined with the tracked vehicle motion model, which is able to apply for the precise navigation purposes.

Determining the tracked vehicle state and posture which are important for the autonomous navigation. This vehicle state and posture are estimated from the information of positioning and inertial sensors by using the tracked vehicle motion model. Consequently, the soil parameter and track coefficients are also computed from both the sensor information's and tracked vehicle motion model. An autonomous tracked combine harvester developed by Zhang (2014), which is steered in a desired field with proper guidance sensing system be able to detect harvester state and posture. There are different sensing systems, including Real Time Kinematic

Global Positioning system (RTK-GPS), Inertial Measurement Unit (IMU) used to find out the control input parameters of the tracked combine harvester (Choi, 2014; Zhang, 2014). For the non-linear characteristics between the tracked combine harvester and terrain, the sensor measurements are sometimes uncertainties which need to compensate by using the tracked combine harvester motion model. For this reasons, a tracked combine harvester motion model is developed based on Wong (2008) with relevant sensor measurements in this chapter. Consequently, the tracked combine harvester model equations are used for estimating the soil parameter and track coefficients during turning maneuverability. In addition, the turning radius is computed from the tracked combine harvester absolute positions by using the regression model (Had to know, 2017), which is a good approach than theoretical turning radius. Therefore, the research in this chapter concentrates to develop a tracked combine harvester motion model combined with the positioning and inertial sensor measurements for determining the robot combine harvester state, posture, soil parameter and track coefficients over a nonlinear terrain for the precise controlling of autonomous tracked combine harvester in real time.

3.2 Materials and Method

3.2.1 System Components

This research was conducted by a YANMAR AG1100 combine harvester that is equipped with an on-board computer to log data from the RTK-GPS and IMU sensors by using RS232C serial ports as shown in figure 3-1. This tracked combine harvester is fully controlled by a CAN bus, and it follows the ISO11783 standard. The speed of tracked combine harvester ranges from 0.1 to 2 m/s, approximately. This harvester can be used to harvest cereal crops like paddy and wheat.



Figure 3-1. Outlook of the tracked combine harvester equipped with RTK-GPS and IMU sensors

The RTK-GPS was used to measure position, direction and speed of the tracked combine harvester, which is discussed in chapter 2. Maximum update and output rates of the RTK-GPS is up to 20 Hz. The low latency configuration (update rate: 5 or 10 Hz, data link: 115200 Baud rate) was used for the RTK mode, and this configuration provides a horizontal position accuracy of 10 mm + 1.0 ppm, a vertical position accuracy of 15 mm + 1.0 ppm and a velocity accuracy of 0.02 m/sec. The RTK correction signal was calculated from a Virtual Reference Station (VRS) via an Internet connected to the on-board computer that logs the data from the RTK-GPS receiver through RS232C serial port. The VN 100 IMU sensor was used as posture sensor which can measure the angular rate of the tracked combine harvester. Its

dynamic accuracy for the yaw rate is 1.0 deg. RMS, heading's dynamic accuracy: 2.0 deg. RMS and the lateral acceleration has an alignment error: ± 0.05 deg., noise density: < 0.14 mG/ $\sqrt{\text{Hz}}$. The output signal from the IMU was logged into the control pc at a frequency of 200 Hz through a USB serial port.

3.2.2 Tracked Combine Harvester dynamic model

Figure 3-2 shows the free body diagram of dynamic model for the tracked combine harvester moving on a general plane (Wong 2008; Kitano & Jyozaki 1976; Tehmoor & Raul 2010), turning to the left or counter clockwise. Its acceleration is in the positive x_c, y_c and φ directions. The external thrusts and resistive forces acting on the tracked combine harvester are F_R, F_L and R_R, R_L , respectively. The value f_y indicates the lateral friction force due to the effect of lateral soil shear.

The figure 3-2 (a) is shown in the global reference frame XYZ, which indicates the tracked combine harvester turns around an instantaneous center of rotation (ICR). The angle β is called sideslip angle that is determined from the velocity V_c and the longitudinal axis x_c of the tracked combine harvester. It is assumed that the normal pressure distribution along the track is non-uniform, and the coefficient of lateral resistance μ is not constant. The instantaneous center of rotation must shift forwards of the tracked combine harvester centroid by the amount of D, as shown in figure 3-2 (a). This longitudinal shifting D depends on the tracked combine harvester lateral acceleration (Wong, 2008). D is required to develop a net lateral force that accelerates the tracked combine harvester towards the instantaneous center of rotation, and also minimizes the resistive yawing moment (Le et al., 1997).

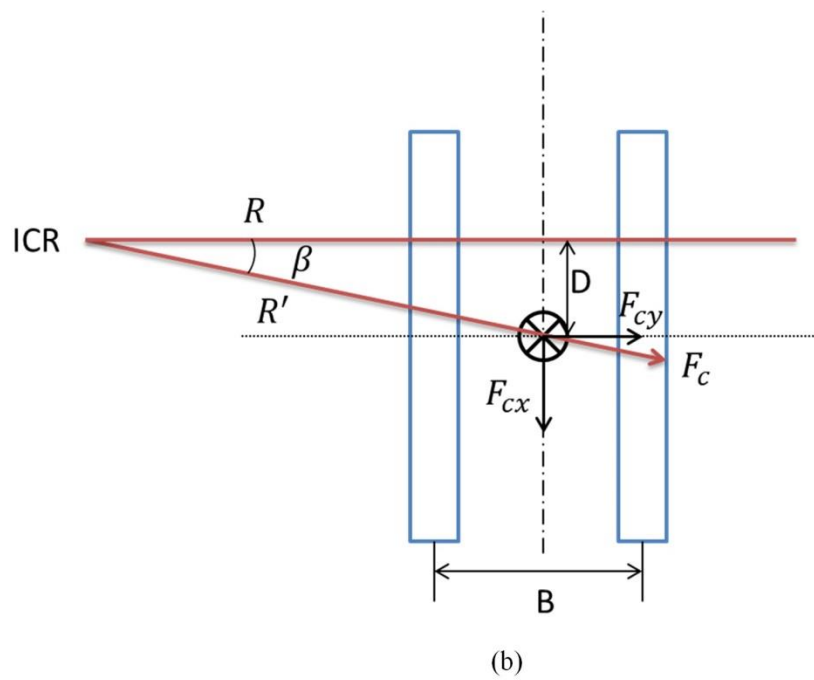
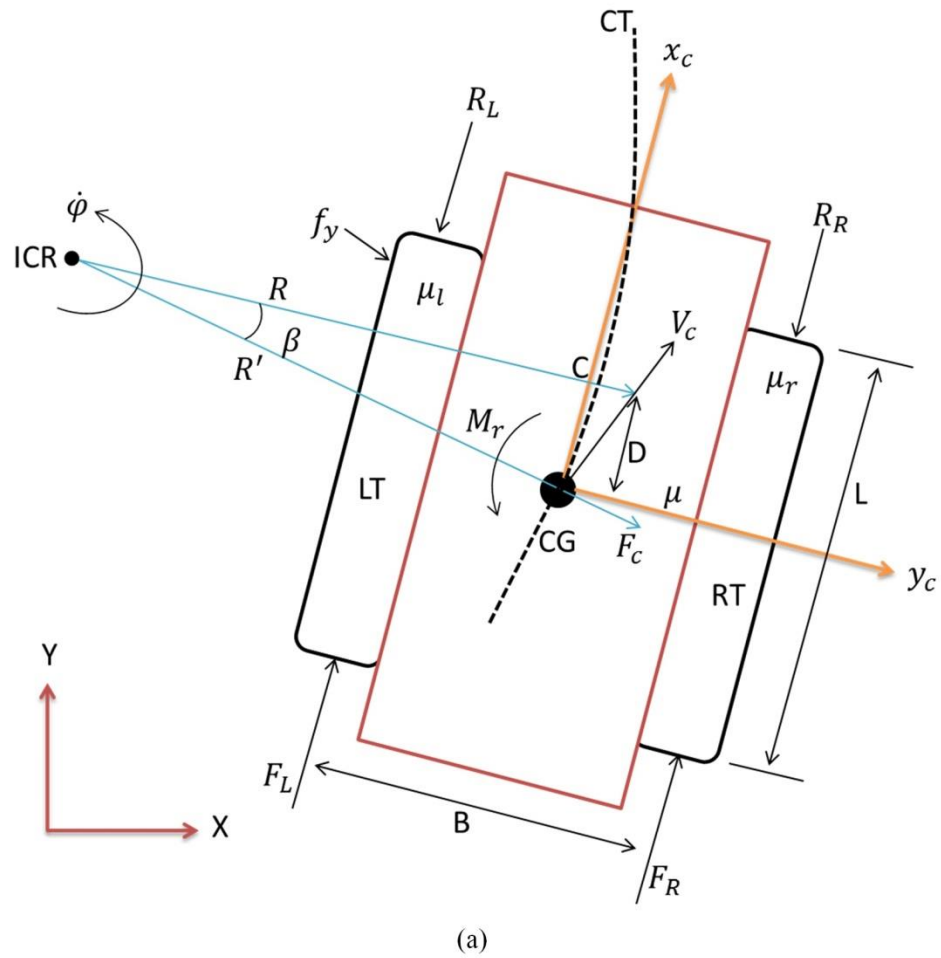


Figure 3-2. Free body diagram of the tracked combine harvester dynamic model (a.

General forces acting on the harvester and b. Detail of centrifugal force F_C)

Using RTK-GPS and IMU measurements along with the tracked combine harvester internal parameters, the dynamic model equations can be modified in order to calculate some essential parameters for automated navigation purposes. For a tracked combine harvester of mass m and a moment of inertia about the center of mass I , the equations of motion can be written in the body reference frame by using Eqs. (3.1), (3.2) and (3.3), respectively.

$$m\ddot{x}_c = F_R + F_L - R_R - R_L - F_c \sin\beta \quad (3.1)$$

$$m\ddot{y}_c = F_c \cos\beta - \mu mg \quad (3.2)$$

$$I\ddot{\phi} = \frac{[(F_R - R_R) - (F_L - R_L)]B}{2} - M_r \quad (3.3)$$

Where, the suffix c denotes coordinates fixed on the tracked combine harvester. The centrifugal force F_c acting on the tracked combine harvester is shown in figure 3-2 (b). The resultant F_c is given by $F_c = \frac{mV_c^2}{R}$, and the longitudinal and lateral centrifugal forces are given by Eqs. (3.4) and (3.5), respectively.

$$F_{cx} \sin\beta = \frac{mV_c^2}{R} \sin\beta \quad (3.4)$$

$$F_{cy} \cos\beta = \frac{mV_c^2}{R} \cos\beta \quad (3.5)$$

The sideslip angle β is calculated from the difference between the direction of the tracked combine harvester given by the RTK-GPS and the heading given by the IMU (Bevly, 2004).

$$\beta = \varphi_{gps} - \varphi_{imu} \quad (3.6)$$

The thrust forces on right and left track are determined by Eqs. (3.7) and (3.8).

$$F_R = \frac{mg(2B\mu_r + \mu L)}{4B} \quad (3.7)$$

$$F_L = \frac{mg(2B\mu_l - \mu L)}{4B} \quad (3.8)$$

It is considered that the centrifugal forces also cause lateral load transfer. Thus, the longitudinal resistive forces of the right and left tracks will not be identical, as described by Eqs. (3.9) and (3.10).

$$R_R = \left(\frac{mg}{2} + \frac{Hm\dot{\phi}^2 R}{B} \right) \mu_r \quad (3.9)$$

$$R_L = \left(\frac{mg}{2} - \frac{Hm\dot{\phi}^2 R}{B} \right) \mu_l \quad (3.10)$$

Considering lateral coefficient of friction μ , the moment of turning resistance M_r around the center of the tracks for the tracked combine harvester is given by Eq. (3.11).

$$M_r = \frac{\mu mgL}{4} \quad (3.11)$$

The lateral coefficient of friction μ depends on the turning radius R , angular rate $\dot{\phi}$, and sideslip angle β which is calculated in the Eq. (3.12).

$$\mu = \frac{1}{g} \left(\dot{\phi}^2 R - \frac{\Delta V_c}{\Delta t} \tan \beta \right) \quad (3.12)$$

After estimating the lateral coefficient of friction μ , the longitudinal coefficient of friction for the right and left tracks is calculated by using Eqs. (3.13) and (3.14).

$$\mu_r = \frac{2}{g} \left[\frac{\Delta V_R}{\Delta t} - \frac{gL}{4B} \mu \right] \quad (3.13)$$

$$\mu_l = \frac{2}{g} \left[\frac{\Delta V_L}{\Delta t} + \frac{gL}{4B} \mu \right] \quad (3.14)$$

3.2.3 Tracked Combine Harvester Kinematic model

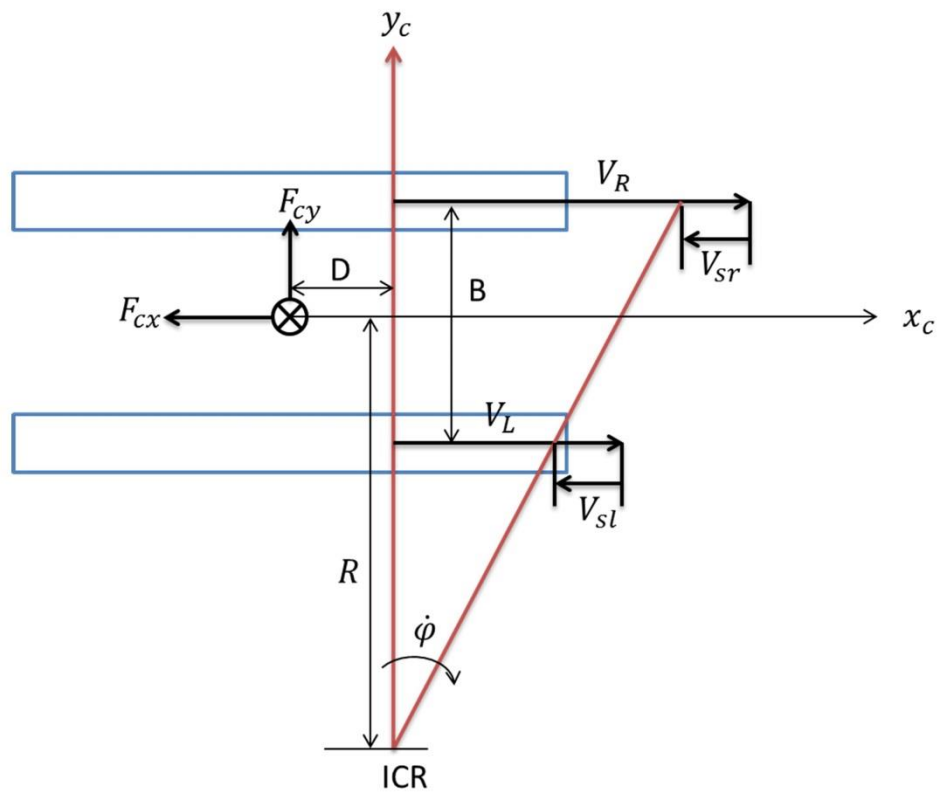


Figure 3-3. Schematic representation of the tracked combine harvester's speed, slip velocity and turning radius

Figure 3-3 shows the tracked combine harvester turning around on instantaneous center of rotation (ICR). Consider the velocities of right and left tracks are V_R and V_L ; with the slip velocities V_{sr} and V_{sl} , the turning radius R and angular velocity $\dot{\phi}$ are expressed by Eq. (3.15) (Kitano & Jyozaki,1976).

$$R\dot{\phi} = \frac{1}{2}[V_R - V_{sr} + V_L - V_{sl}] \quad (3.15)$$

Using the Eq. (3.15), the theoretical radius R is obtained by the Eq. (3.16).

$$R = \frac{[V_R(1-s_r)+V_L(1-s_l)]}{2\dot{\phi}} \quad (3.16)$$

Where, the left and right track slips are computed by the following Eqs. (3.17) and (3.18), respectively.

$$S_l = 1 - \frac{2V_{gps} - B\dot{\varphi}}{2V_L} \quad (3.17)$$

$$S_r = 1 - \frac{2V_{gps} + B\dot{\varphi}}{2V_R} \quad (3.18)$$

The vehicle's velocity V_c is calculated based on the each track's velocity including the slip of tracks from the tracked combine harvester expressed by the Eq. (3.19).

$$V_c = \frac{V_R(1-S_r) + V_L(1-S_l)}{2} \quad (3.19)$$

Figure 3-4 shows the RTK-GPS positions used to calculate the actual turning radius R by using the least square method (Had to know, 2017). The general circle equation is indicated by the Eq. (3.20).

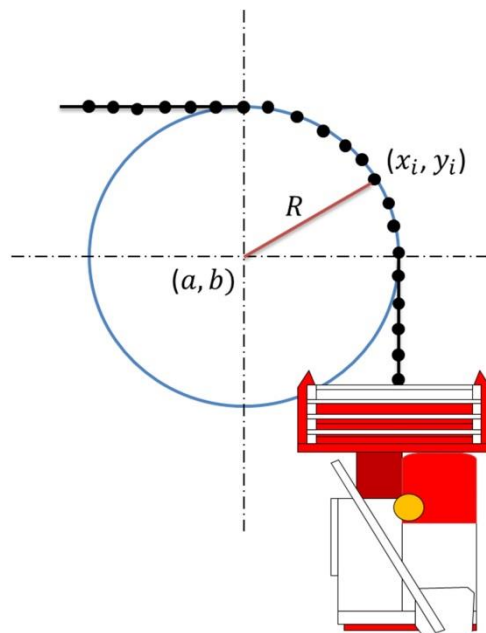


Figure 3-4. Turning radius R calculated from the RTK-GPS positions

$$(a - x)^2 + (y - b)^2 = R^2 \quad (3.20)$$

With the least squares, “best fit” means the equation have to minimize that is

$$F(h, k, R) = \sum [(x_i - h)^2 + (y_i - k)^2 - R^2]^2$$

The circle equation can be linearized by the Eq. (3.21).

$$x^2 + y^2 = Ax + By + C \quad (3.21)$$

The Eq. (3.21) is now linear in the undetermined coefficients A, B and C . To compute these coefficients, a matrix equation developed for circular regression is arranged as given in the Eq. (3.22).

$$\begin{bmatrix} \sum x_i^2 & \sum x_i y_i & \sum x_i \\ \sum x_i y_i & \sum y_i^2 & \sum y_i \\ \sum x_i & \sum y_i & n \end{bmatrix} \begin{bmatrix} A \\ B \\ C \end{bmatrix} = \begin{bmatrix} -\sum(x_i^3 + x_i y_i^2) \\ -\sum(x_i^2 y_i + y_i^3) \\ -\sum(x_i^2 + y_i^2) \end{bmatrix} \quad (3.22)$$

Where n is the number of RTK-GPS points (x_i, y_i) . In Eq. (3.22), if the left side matrix is invertible, the values of A, B and C generate the circle of best fit. After obtaining A, B and C , the center of the circle and the turning radius R are found by using Eqs. (3.23) and (3.24).

$$a = -\frac{A}{2}, \quad b = -\frac{B}{2} \quad (3.23)$$

$$R = \sqrt{(a^2 + b^2 - C)} \quad (3.24)$$

It is necessary to fix the direction (left and right turn) of the turning radius for the tracked combine harvester. For the direction of turning radius R , the Eq. (3.25) is calculated and made a condition based on cross product using the circle center and RTK-GPS position (where, $i = 0, 1, 2 \dots$).

$$(a_i - x_i)(y_{i+1} - y_i) - (b_i - y_i)(x_{i+1} - x_i) \begin{cases} > 0; R > 0 \text{ for right turn} \\ < 0; R < 0 \text{ for left turn} \end{cases} \quad (3.25)$$

Now, the equations (3.1) and (3.2) are integrated to make the velocities of longitudinal and lateral direction for the tracked combine harvester in local coordinate. In order to run the tracked combine harvester in real time, the velocities of longitudinal and lateral in the harvester coordinate is expressed as a global reference frame by the Eq. (3.26).

$$\begin{bmatrix} \dot{X} \\ \dot{Y} \end{bmatrix} = \begin{bmatrix} \cos\varphi & -\sin\varphi \\ \sin\varphi & \cos\varphi \end{bmatrix} \begin{bmatrix} \dot{x}_c \\ \dot{y}_c \end{bmatrix} \quad (3.26)$$

3.2.4 Methods

This dynamic system was verified by the field experiment in the Hokkaido University agricultural field. The tracked combine harvester with a proper configuration of RTK-GPS and IMU sensors were tested during the experiment. In this case, the tracked combine harvester was moved on the soil with half cut of wheat straw field. A set of input steering angles were fixed to run the tracked combine harvester at a circular and a sinusoidal trajectories. A constant 30 deg. and 40 deg. of steering angle were chosen for circular trajectory; whereas ± 30 deg. and ± 40 deg. steering commands for sinusoidal trajectory. Completely running at circular and sinusoidal trajectories, position, direction and speed of the tracked combine harvester from RTK-GPS and angular rate from IMU were used to obtain the state of the tracked combine harvester, track-soil interaction parameters, and track coefficient from the dynamic model. The physical parameters like mass (m), center height (H), track length (L), track tread (B) and moment of inertia (I) for the tracked combine harvester are 4610 kg, 1.2 m, 1.780 m, 1.185 m and 5270 kg-m², respectively, which were inputted in that model. The turning radius R is calculated based on the RTK-

GPS position by the Eq. (3.24) for tuning maneuverability. C/C++ programming language was used to describe the above parameters in this research.

3.3 Results and Discussion

3.3.1 Trajectories of Tracked Combine Harvester

Figure 3-5 shows the measured and dynamic model trajectories of tracked combine harvester. These trajectories were obtained by running the tracked combine harvester in a circular and sinusoidal way on a concrete and soil ground in the agricultural field side of Hokkaido University, Japan. The measured trajectory was obtained from the RTK-GPS which is fixed on the tracked combine harvester by using a set of commanding input steering angles. Figure 3-5 (a) and (c) indicates the circular trajectories on the concrete ground while steering angle was 30 and 40 deg.; whereas the circular trajectories on the soil ground was for 30 and 40 deg. as shown in figure 3-5 (b) and (d).

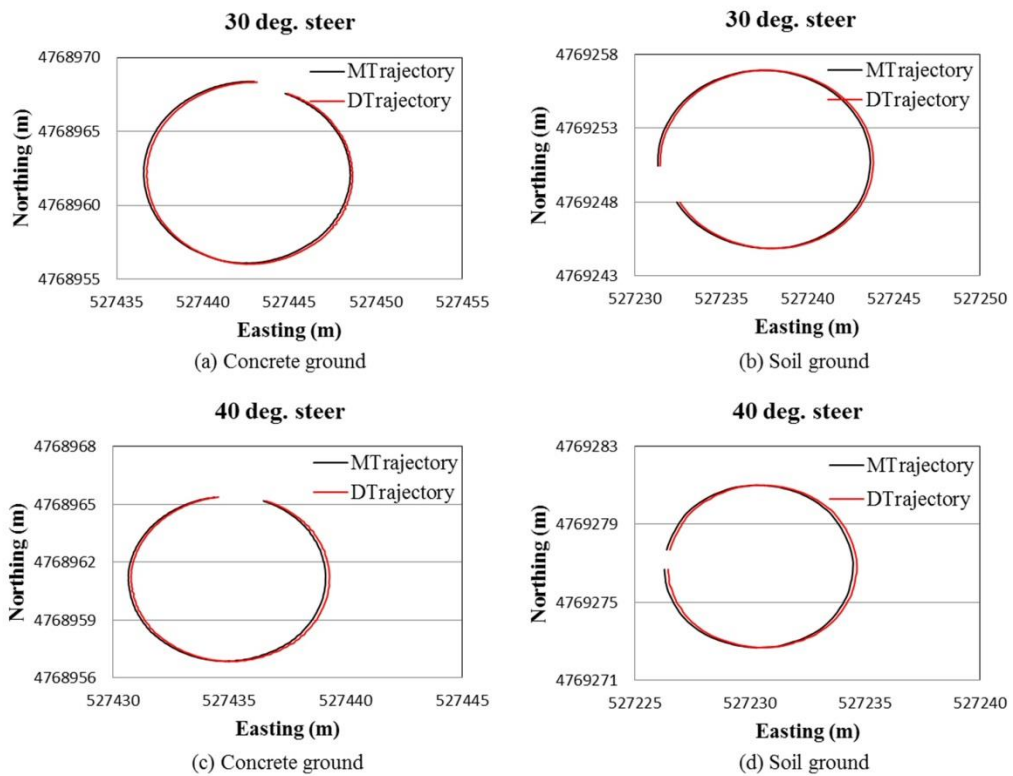


Figure 3-5. Measured Trajectory (MTrajectory) and Dynamic model trajectory (DTrajectory) of the tracked combine harvester which runs in a circular way

The results showed that the dynamic model trajectories of tracked combine harvester matched with the measured trajectories fairly well. From the error analysis of circular trajectories, the RMS errors between the measured and dynamic model for the concrete and soil ground are 0.029 m & 0.012 m for 30 deg. steering and 0.026 m & 0.013 m for 40 deg. steering, respectively. The RMS error for concrete ground is higher than soil ground because of sliding the tracks of the combine harvester on concrete ground.

The sinusoidal trajectories were obtained from a series of steering angle of ± 30 deg. and ± 40 deg. as shown in figure 3-6. Figure 3-6 (a) and (c) indicates the sinusoidal trajectories on concrete ground whereas figure 3-6 (b) and (d) are on soil

ground. The RMS errors of sinusoidal trajectories for concrete and soil ground are 0.034 m & 0.032 m for ± 30 deg. steering and 0.028 m & 0.016 m for ± 40 deg. steering. These results indicate that the dynamic model trajectories for both grounds are consistent to the measured one.

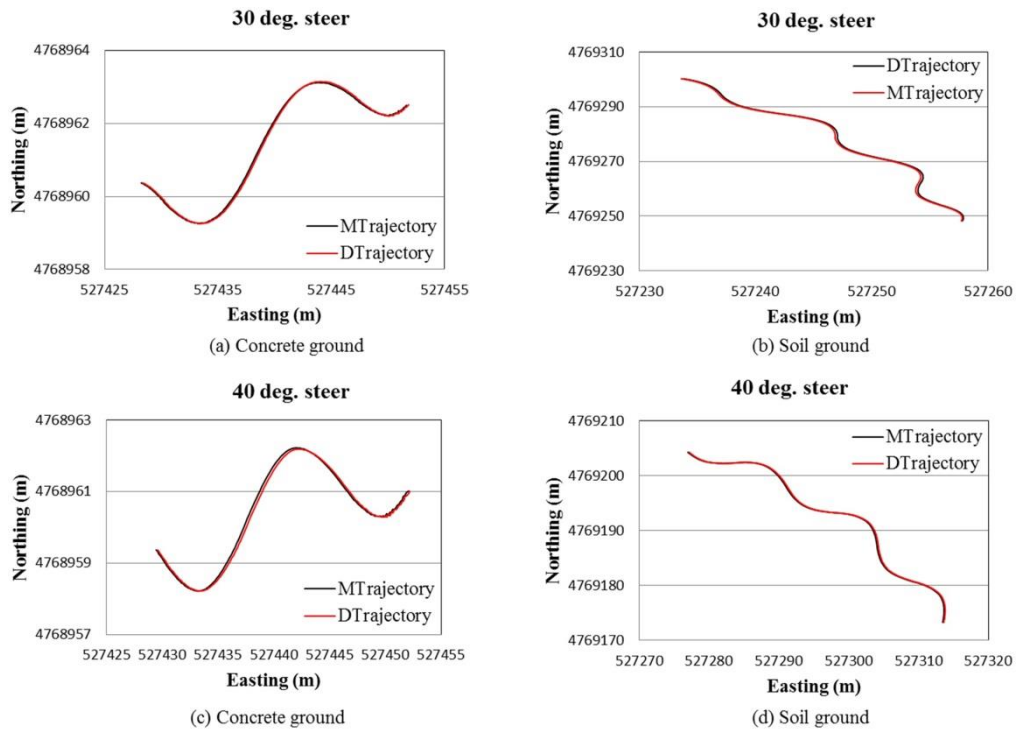


Figure 3-6. Measured Trajectory (MTrajectory) and Dynamic model trajectory (DTrajectory) of the tracked combine harvester which runs in a sinusoidal way

3.3.2 Yaw rate of Tracked Combine Harvester

Figure 3-7 shows the measured and dynamic model yaw rate $\dot{\phi}$ of tracked combine harvester for the circular trajectories. The measured yaw rate $\dot{\phi}$ is obtained directly from the IMU sensor while the dynamic model yaw rate $\dot{\phi}$ is calculated from the dynamic model equation. The dynamic model yaw rate $\dot{\phi}$ can be influenced by the yaw moment of inertia because it is a divisor factor. The yaw moment of inertia is very important that reflects the tracked combine harvester's resistance to change its

direction; which means a big yaw moment of inertia makes the combine harvester slower to swerve or go into a tight curve, and it also makes it slower to turn straight again (Ospina and Noguchi, 2016). Figure 3-7 (a) and (b) shows the measured and dynamic yaw rate for 30 deg. steering where the RMS errors are 0.0004 rad/sec for both grounds. The RMS errors obtained from the measured and dynamic yaw rate for 40 deg. steering are 0.0004 rad/sec for concrete ground and 0.0007 rad/sec for soil ground in figure 3-7 (c) and (d). In figure 3-8, the measured and dynamic yaw rate were obtained from the sinusoidal trajectory. The RMS errors of sinusoidal trajectories for both grounds are 0.0004 rad/sec for ± 30 deg. steering in figure 3-8 (a) and (b) and 0.0007 rad/sec for ± 40 deg. steering in figure 3-8 (c) and (d). The RMS error indicates that the yaw rate $\dot{\phi}$ given by the dynamic model is more closer to the measured yaw rate $\dot{\phi}$.

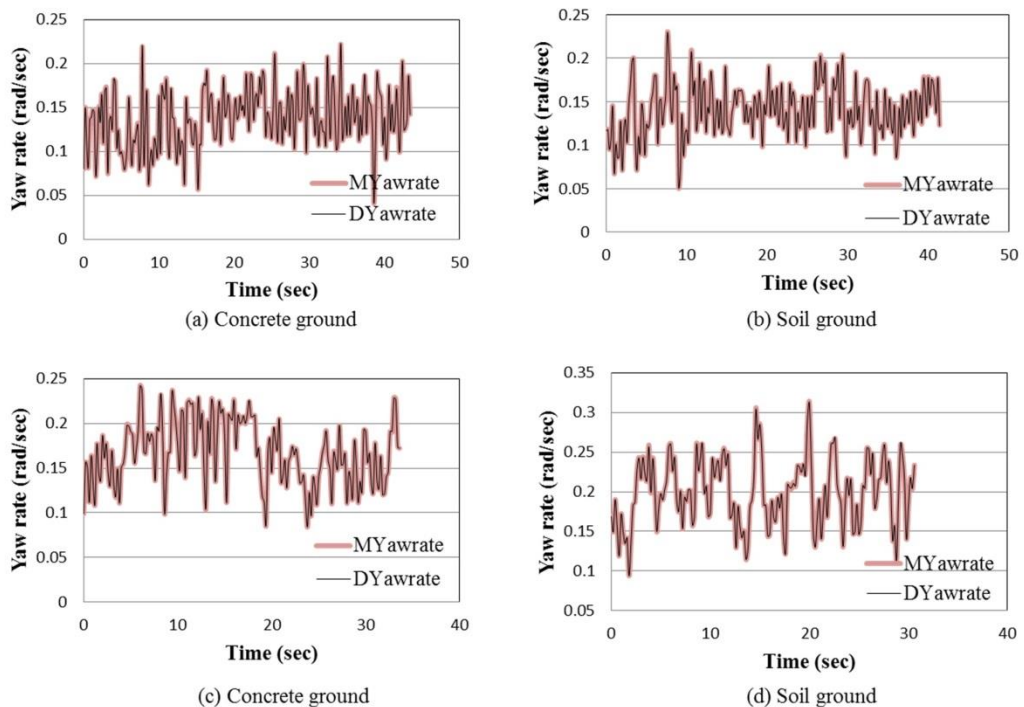


Figure 3-7. Measured yaw rate (MYawrate) and Dynamic model yaw rate (DYawrate) of the tracked combine harvester which runs in a circular way

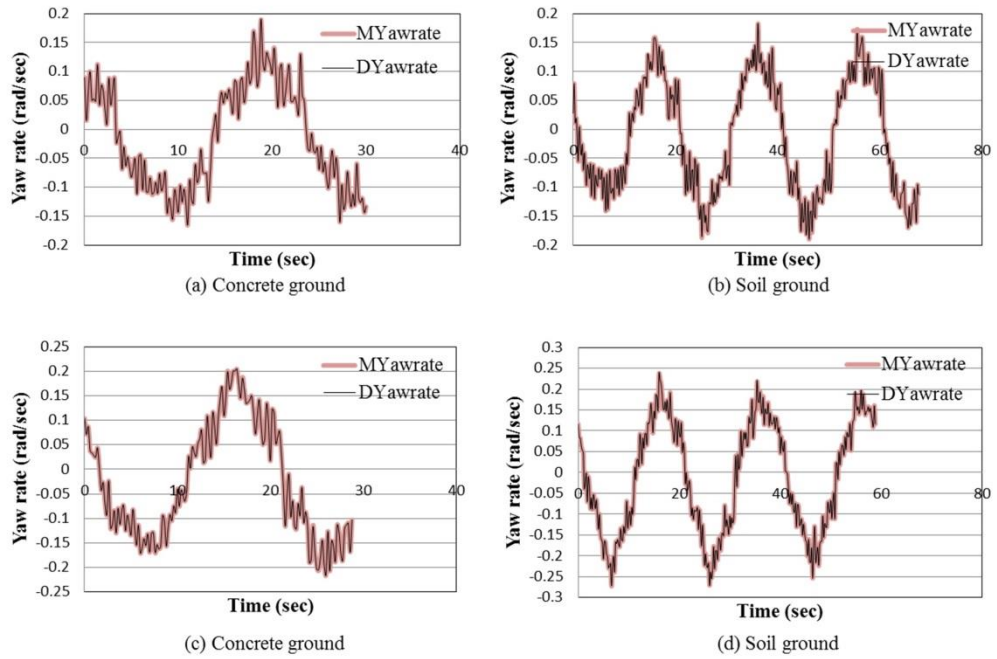


Figure 3-8. Measured yaw rate (MYawrate) and Dynamic model yaw rate (DYawrate) of the tracked combine harvester which runs in a sinusoidal way

3.3.3 Speed of Tracked Combine Harvester

Figure 3-9 shows the speed of tracked combine harvester for the circular trajectories moved on a concrete and soil ground when the steering angles were 30 and 40 deg., respectively. On the other hand, the speed for sinusoidal trajectories is given by the figure 3-10 for ± 30 and ± 40 deg. steering. These figures indicate that the speed is not constant all over the time, and it varies time to time.

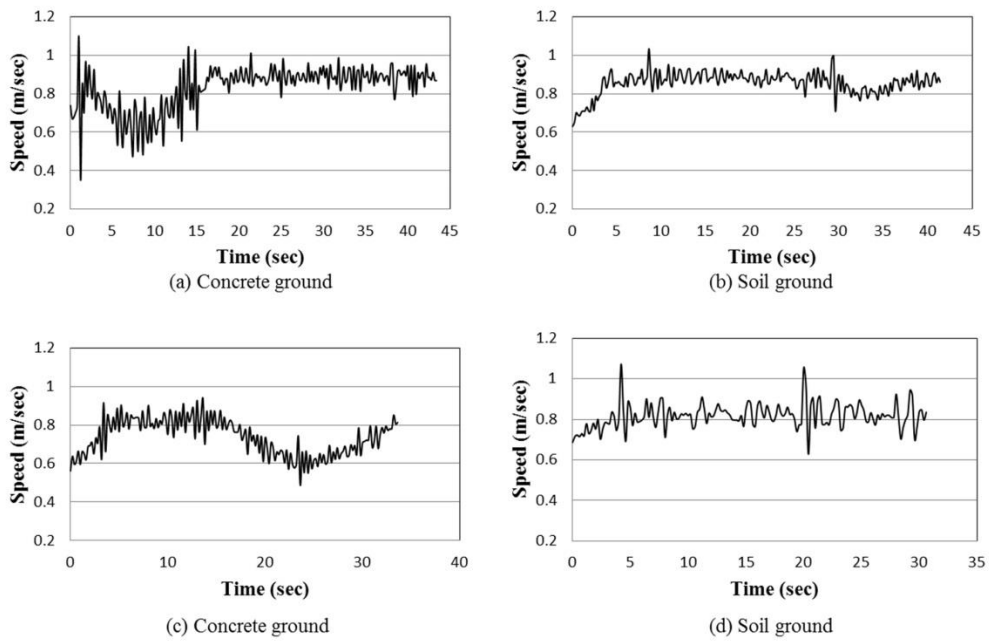


Figure 3-9. Speed of the tracked combine harvester for circular trajectories

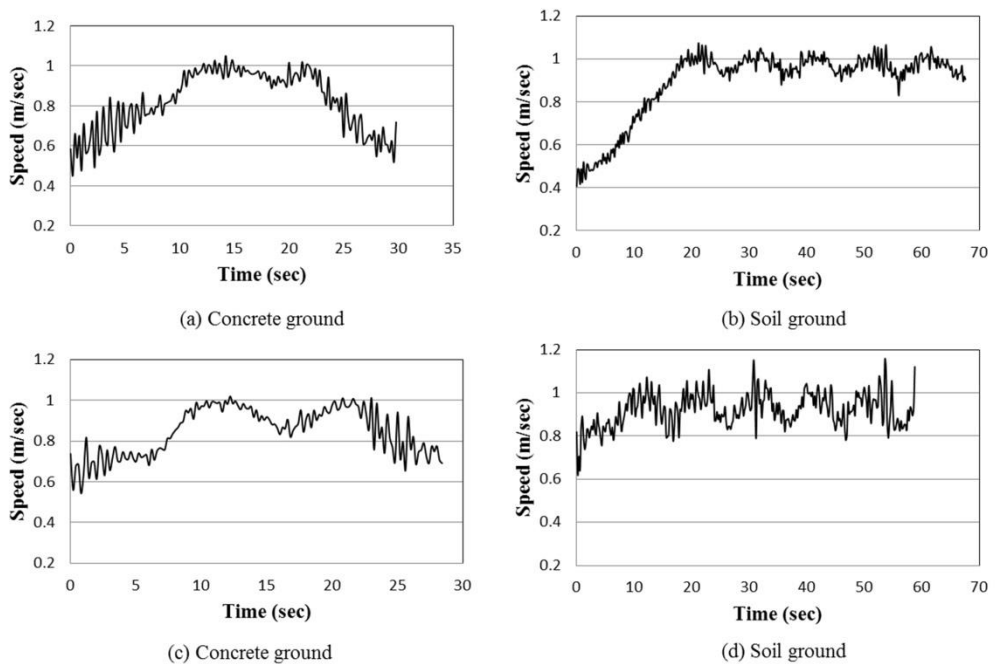


Figure 3-10. Speed of the tracked combine harvester for sinusoidal trajectories

3.3.4 Sideslip angle of Tracked Combine Harvester

Figure 3-11 and 3-12 shows the theoretical sideslip angle β which was calculated from the equation $\beta = \tan^{-1}\left(\frac{\dot{x}}{\dot{y}}\right)$ and compared with the measured side slip angle β obtained from the heading difference of RTK-GPS and IMU. In circular trajectories of the tracked combine harvester for concrete ground in figure 3-11 (a) and (c), the RMS errors between the measured and theoretical sideslip angle are 3.52 deg. for 30 deg. steering and 3.69 deg. for 40 deg. steering. In figure 3-11 (b) and (c), RMS errors for soil ground are 2.87 deg. for 30 deg. steering and 3.46 deg. for 40 deg. steering. The RMS errors of sideslip angle over concrete ground are little bit higher than soil ground because of sliding the combine harvester tracks on the concrete surface. On the other hand, sideslip angle was obtained from the sinusoidal trajectories of ± 30 and ± 40 deg. over concrete ground and soil ground as shown in figure 3-12. The RMS errors of sideslip angle over concrete ground are 4.03 deg. for ± 30 deg. steering and 4.88 deg. for ± 40 deg. steering in figure 3-12 (a) and (c), whereas the RMS errors of sideslip angle for soil ground are 2.23 deg. for ± 30 deg. steering and 2.79 deg. for ± 40 deg. steering as shown in figure 3-12 (b) and (d). In addition, the fluctuation of sideslip angle β is caused by the integration of yaw rate, noisy RTK-GPS direction angle and speed of the tracked combine harvester. A low speed with a high steering angle can make a little bit large slip angles (Bevly et al., 2010). In addition, the speed of the tracked combine harvester is not uniform, which influences the change of the direction of tracked combine harvester suddenly and makes a large fluctuation of sideslip angle β .

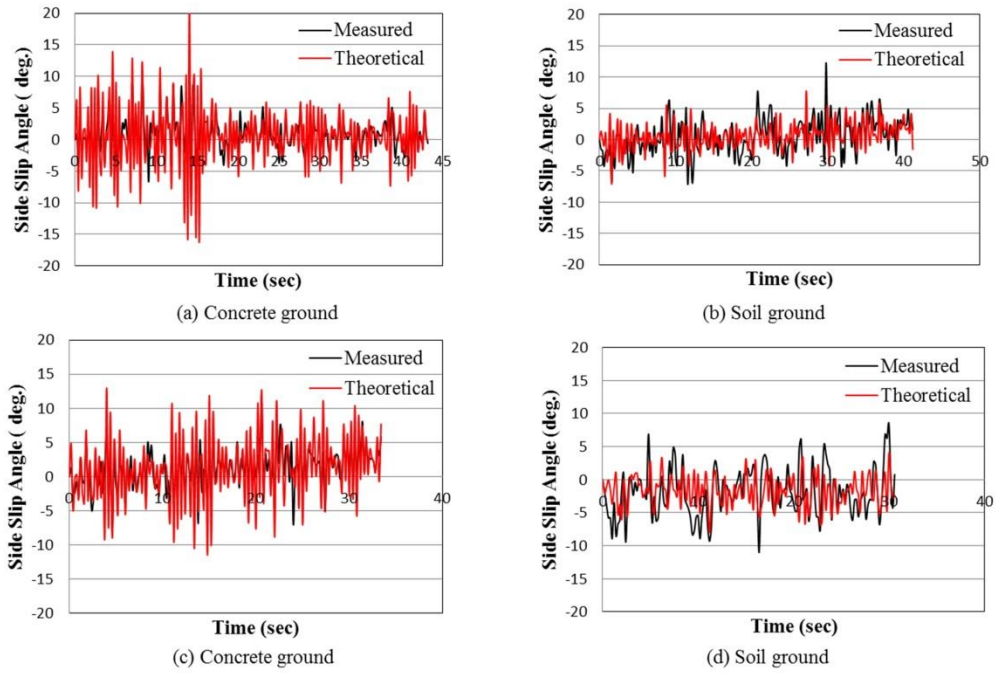


Figure 3-11. Measured and theoretical sideslip angle β for the circular trajectories

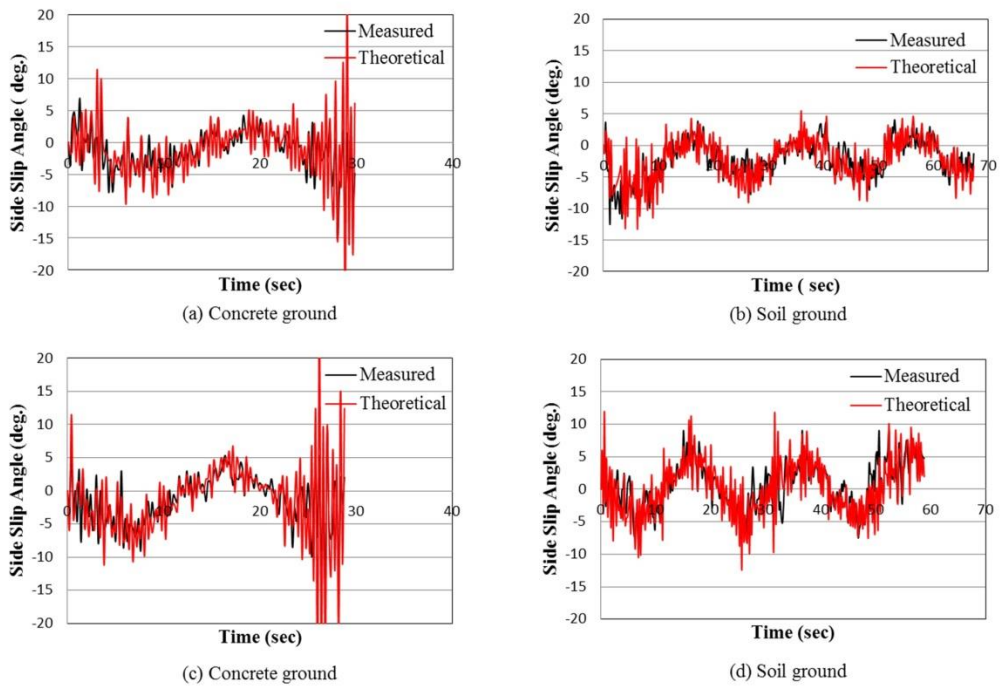


Figure 3-12. Measured and theoretical sideslip angle β for the sinusoidal trajectories

3.3.5 Turning Radius of Tracked Combine Harvester

Figure 3-13 and 3-14 shows the theoretical and measured turning radius R over time for circular and sinusoidal trajectories calculated by Eqs. (3.16) and (3.24). The measured turning radius R was calculated from the RTK-GPS position of the tracked combine harvester. The smoothness of measured turning radius R depends on the number of points chosen for the regression analysis by using the Eq. (3.24). The turning radius R for circular trajectories is almost constant with small fluctuation. The average turning radiuses R for circular trajectories are 6.0 m for 30 deg. steering and 4.2 m for 40 deg. steering as shown in figure 3-13. On the other hand, theoretical turning radius R was estimated for the evaluation of the measured turning radius. Unlike measured turning radius, theoretical turning radius is noisy but shows the similar trend. Theoretical output is influenced by the yaw rate and speed of the tracked combine harvester.

Figure 3-14 shows the inverse turning radius R for sinusoidal trajectories over time when the steering angles were of ± 30 and ± 40 deg., respectively. The inverse turning radius describes the continuous motion of the tracked combine harvester. The results indicated that the tracked combine harvester turns to the left side, the turning radius R will be negative; otherwise turning radius R will be positive for a right turn. Theoretical turning radius R is noisy but it's give a similar sinusoidal shape as measured turning radius.

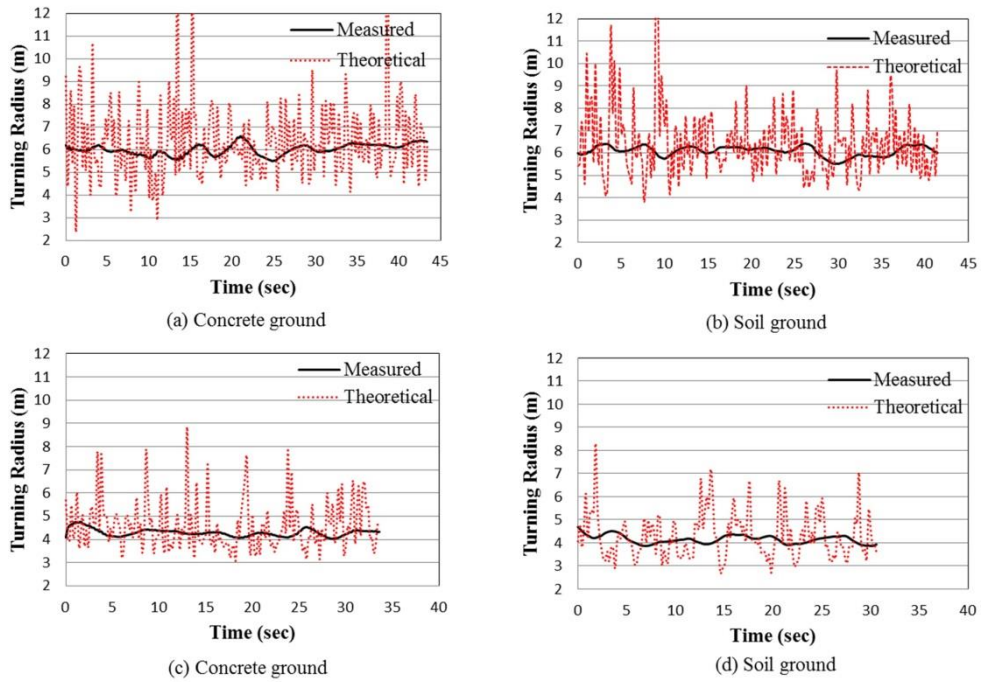


Figure 3-13. Measured and theoretical turning radius R for the circular trajectories

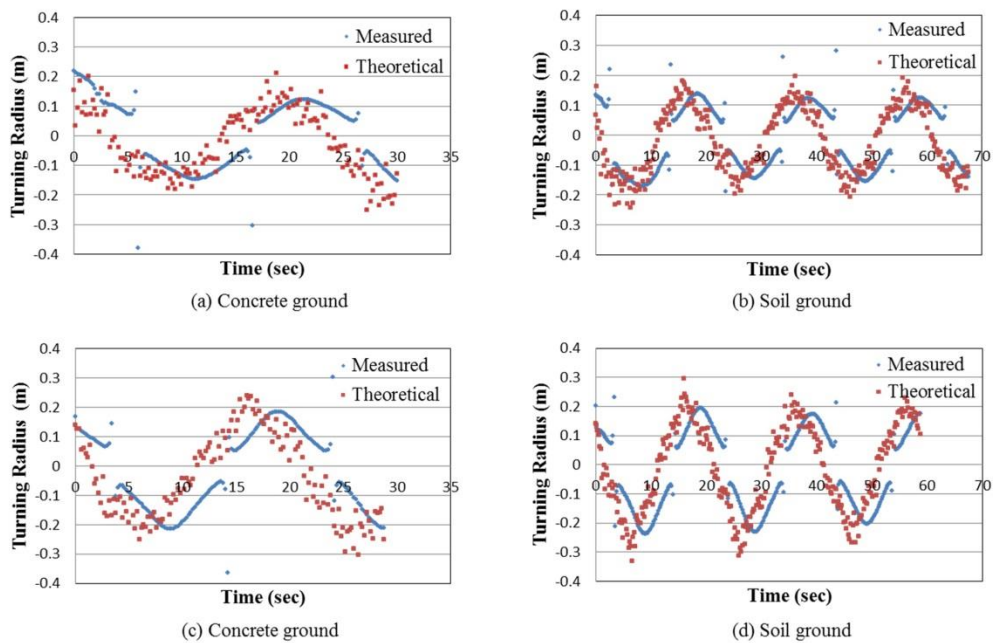


Figure 3-14. Measured and theoretical turning radius R for the sinusoidal trajectories

3.3.6 Tracks slip of Tracked Combine Harvester

Figure 3-15 and 3-16 shows the slip of left and right tracks for circular and sinusoidal trajectories, which are obtained by Eqs. (3.17) and (3.18), respectively. The slip of circular and sinusoidal trajectories for the concrete and soil ground is influenced by the steering command. When the tracked combine harvester runs both circular and sinusoidal trajectories, the slip increases significantly with increased the steering command in order to generate the track thrusts that overcome the turning moment resistance. This track thrusts cause a high slip of the outer track (Le, 1999). In 40 deg. steering, the slip of left track is higher than the slip of left track for 30 deg. steering during the right turning of the tracked combine harvester as shown in figure 3-15. But for sinusoidal trajectories, the slip for each track will be influenced by increasing the steering command because its turning is occurred consecutively left and right turns of the track. In figure 3-16, the slip of left and right tracks for both grounds during ± 30 deg. steering are little smaller than the slip for ± 40 deg. steering.

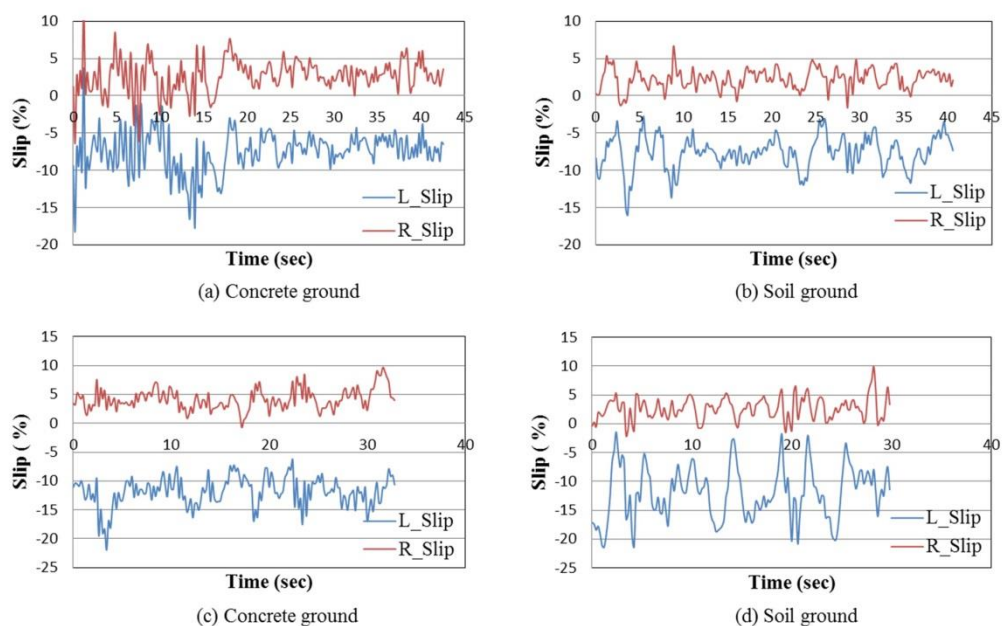


Figure 3-15. Computed slip of left and right tracks for the circular trajectories

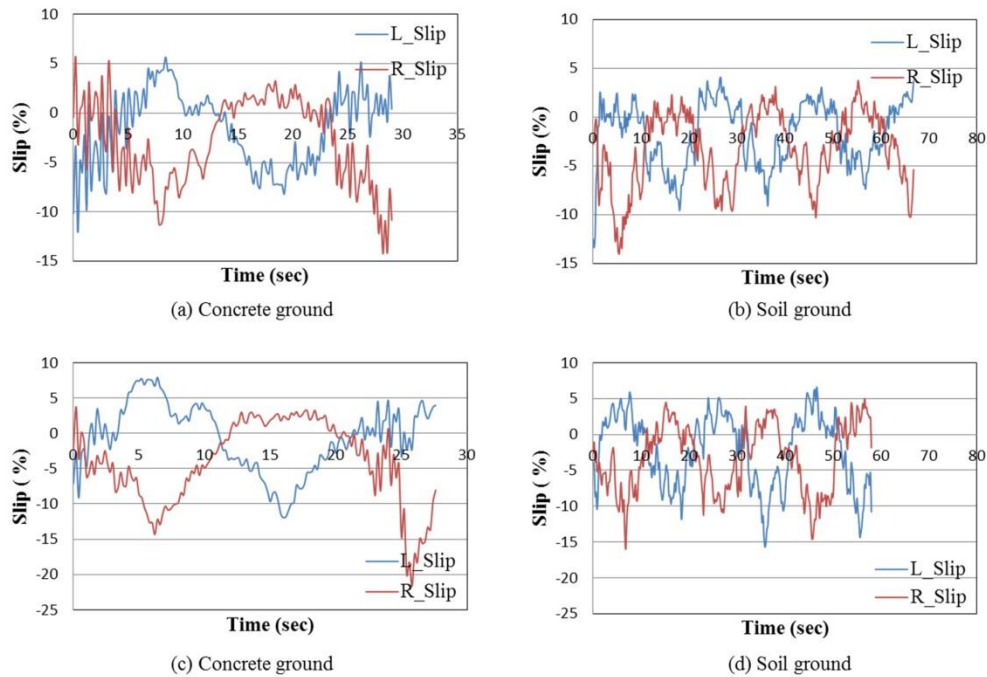


Figure 3-16. Computed slip of left and right tracks for the sinusoidal trajectories

3.3.7 Lateral Coefficient of Friction

By using the Eq. (3.12), the lateral coefficient of friction μ is computed for the circular and sinusoidal trajectories. Figure 3-17 and 3-18 shows the lateral coefficient of friction μ of the tracked combine harvester over time for the concrete and soil ground. The variation of lateral coefficient μ may be caused with the high thrust and small turning radius as compared to large turning radius (Tehmoor & Raul, 2010). It is also influenced by the each track velocity. In circular trajectories, the estimated lateral coefficient of friction μ for both concrete and soil ground are same due to same turning radius R as shown in figure 3-17 (a) and (b), but it may be higher for small tuning radius in figure 3-18 (c) and (d) as compared to the large turning radius. Similarly, the lateral coefficient for sinusoidal trajectories over concrete and soil ground can be increased from the larger turning radius to smaller turning radius as shown in figure 3-18.

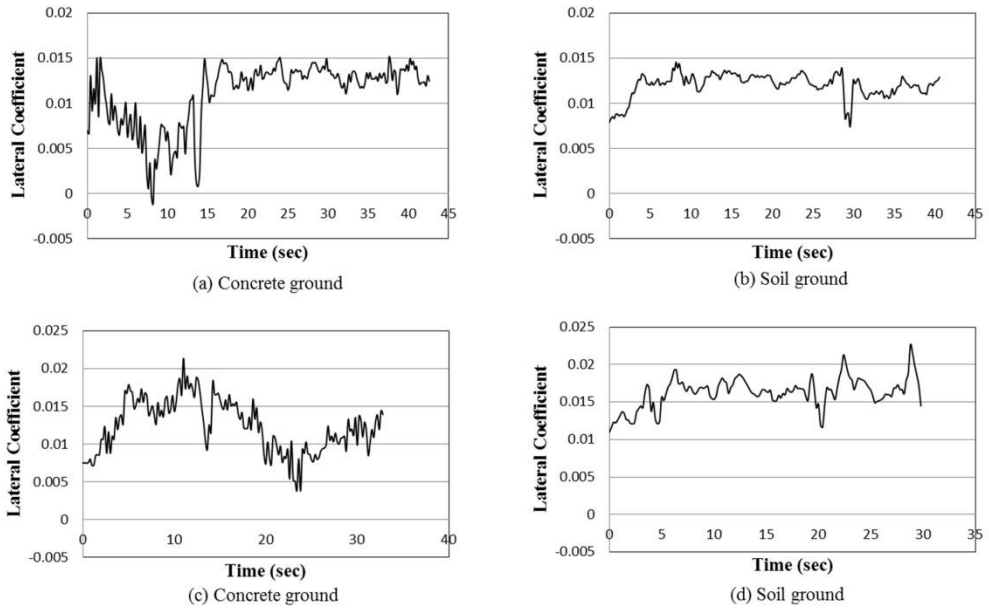


Figure 3-17. Lateral coefficient of circular trajectories for the concrete and soil ground

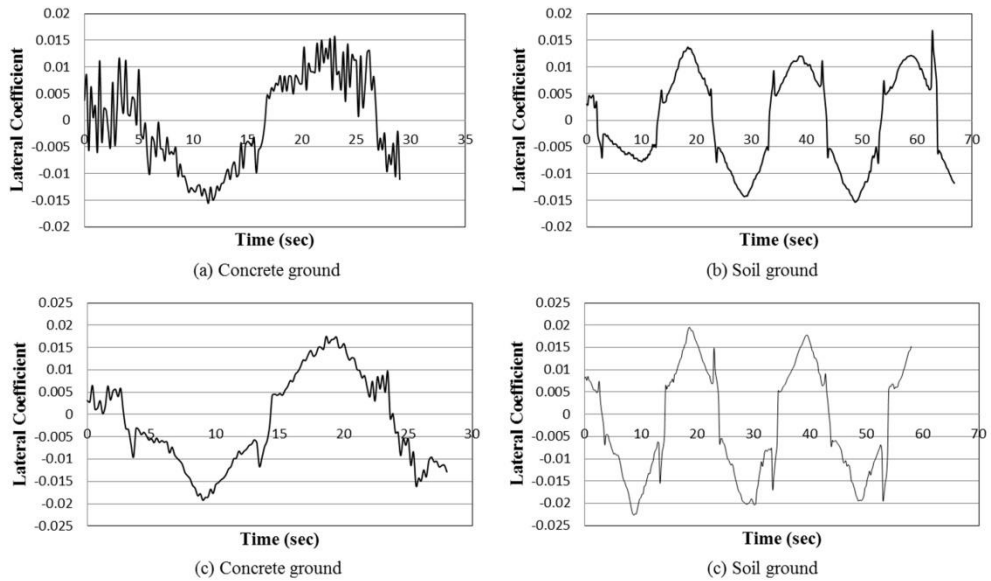


Figure 3-18. Lateral coefficient of sinusoidal trajectories for the concrete and soil ground

3.3.8 Longitudinal Coefficient of Friction

Figure 3-19 and 3-20 shows the longitudinal coefficient of friction for the left and right tracks for the circular and sinusoidal trajectories. The longitudinal coefficient of friction depends on the steering angle, turning radius and lateral coefficient of friction; which may be changed from terrain to terrain. Tehmoor & Raul (2010) reported that the coefficients of friction may be small to grass-gravel or concrete terrain. The longitudinal coefficient of friction for left and right tracks increase when the steering angle increases or turning radius R decreases. The longitudinal coefficients of friction for the left and right tracks by using Eqs. (3.13) and (3.14) are smaller for 30 deg. steering in figure 3-19 (a) and (b) than the longitudinal coefficient for 40 deg. steering in figure 3-19 (c) and (d).

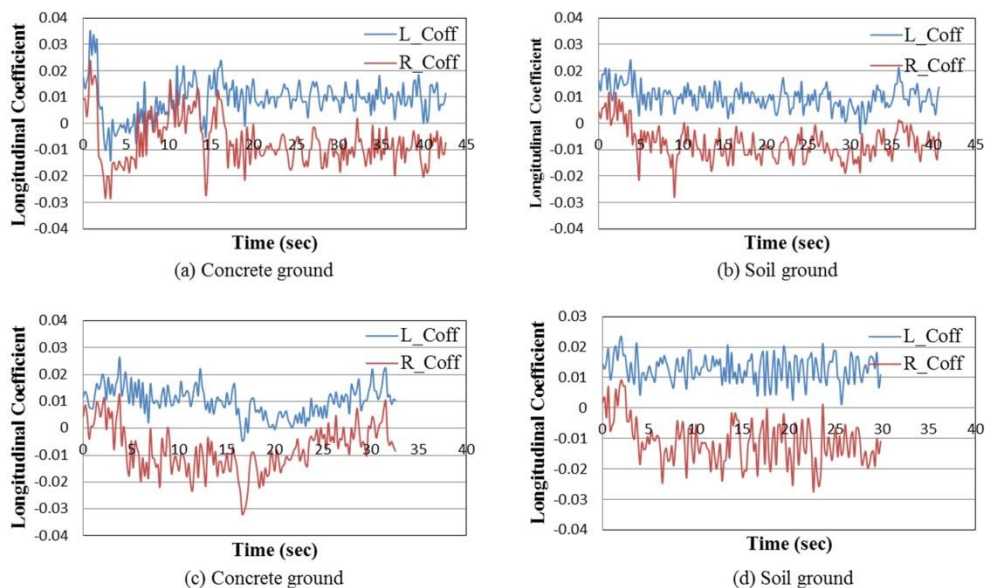


Figure 3-19. Longitudinal coefficient of friction for the left and right tracks computed for the circular trajectories on the concrete and soil ground

For sinusoidal trajectories over concrete and soil ground in figure 3-20, the longitudinal coefficient for the left and right tracks increases in order to the changing of steering command from ± 30 to ± 40 deg., respectively.

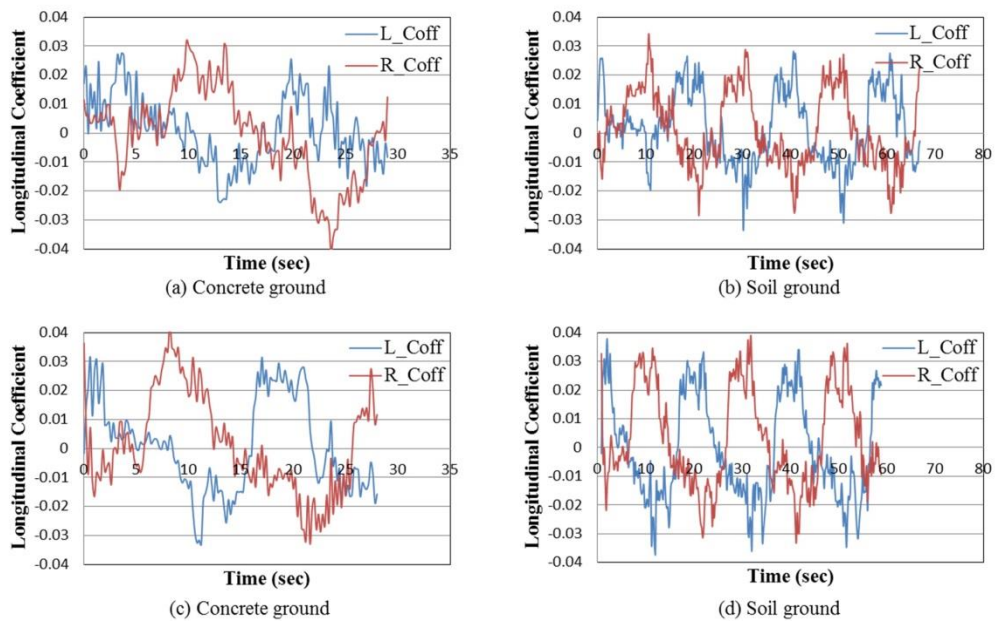


Figure 3-20. Longitudinal coefficient of friction for the left and right tracks computed for the sinusoidal trajectories on the concrete and soil ground

3.4 Conclusions

This paper describes the tracked combine harvester dynamic model equipped with the positioning and inertial system to compute the combine harvester state and orientation. Based on the tracked combine harvester dynamic model and sensor measurements, the soil interaction parameter and track coefficients were computed. The results of computed slip and coefficient of friction can be changed in terrain to terrain due to change of the tracked combine harvester steering and turning radius. The tracked combine harvester dynamic model is verified to estimate the tracked

combine harvester state based on the sensor measurements. The turning radius from the RTK-GPS positions using regression model is better than theoretical turning radius. In addition, based on the computed slip, sideslip angle, track coefficient of friction and turning radius, the tracked combine harvester dynamic model can be used to control the autonomous tracked combine harvester precisely for non-linear condition in all terrain. In future, the sensor measurement uncertainties will be compensated by using this tracked combine harvester motion model during turning maneuverability.

Chapter 4 Heading Estimation of Tracked Combine Harvester during Nonlinear Maneuverability

4.1 Introduction

Tracked vehicles are more popular than wheeled vehicles due to their non-linear characteristics between the tracks and the ground, which can be operated at any adverse field condition for agricultural farming, and makes turn at high speed and low turning radius or higher steering command. In autonomous condition, the tracked vehicle consists of global positioning system and inertial sensor for providing the vehicle state and direction, but during turning of this tracked vehicle, the inertial sensor reading gives measurement uncertainties. Since, the vehicle direction is more important for autonomous guidance and other navigation purposes, it is necessary to compensate this uncertainty of inertial sensor measurement.

The main controlling feature of auto guidance is to steer the vehicle followed a desired path automatically, which requires a proper guidance system be able to detect vehicle position and orientation, create proper steering signal, and steer the vehicle according to the signal (Zhang et al., 1999). There are different guidance sensing systems, including Global Positioning system (GPS), inertial sensors, geomagnetic direction sensors (GDS), machine vision and laser scanner which are used to find out the control parameters of the autonomous vehicles such as heading and offset (Ishii et al., 1994; Benson et al., 2001; Kise et al., 2001 & 2003; Choi, 2014). The functional characteristics of each sensor provide desired information's which contains erroneous measurement reading due to noise, measurement errors, and time delays. In general, a single sensor can not provide enough information, whereas multi-sensors integration can solve this problem, which also needs to fuse in a way to reduce sensor

uncertainties and perform the additional task of interpretation; which is more helpful and informative than what can be observed using a single sensor (Adla, 2013). Noguchi et al. (1998) developed a guidance system based on the RTK-GPS, GDS and machine vision by using a sensor fusion method which provides the most appropriate vehicle heading and offset information in real time. A non-linear extended kalman filter is used to compensate state noise, and measure trajectory, orientation and other soil parameters for the tracked vehicles (Tehmoor and Raul, 2010).

An autonomous tracked combine harvester developed by Zhang (2014) is used to cut the wheat and paddy in real time by using an appropriate harvesting map which is created based on the global positioning system and inertial sensors. But before harvesting, the outside crop near to headland is cut twice or thrice by the tracked combine harvester, and during this time the sensors measurement is logged for making a navigation map. Generally, the tracked combine harvester takes turn at moderate to high speed with low turning radius, which is very popular to the farmers and this turning position is marked by a circle in figure 4-1. During turning, the absolute heading of tracked combine harvester is difficult to estimate due to the uncertainty of inertial sensor. For getting absolute heading, this sensor measurement needs to compensate by using tracked combine harvester motion model and sensor fusion method. In this chapter, the tracked combine harvester dynamic model which is discussed in chapter 3 and the sensor fusion method combined with global positioning system and inertial sensor are used to estimate the absolute heading of tracked combine harvester during turning at high speed and high steering command in the crop field. This estimated heading can further be used to obtain the crop periphery for calculating the harvesting map of the robot combine harvester.

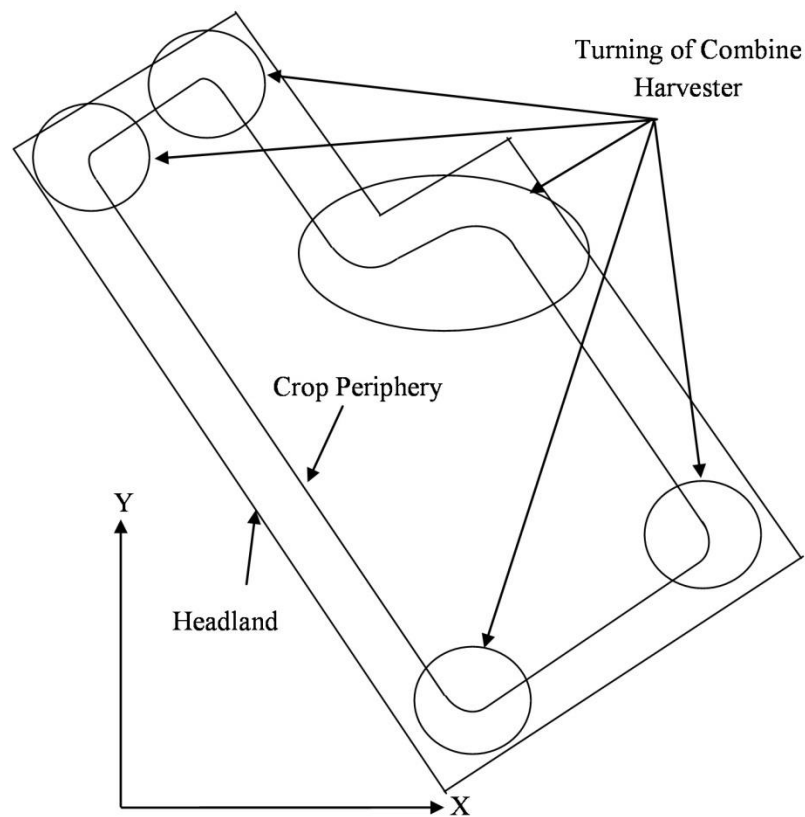


Figure 4-1. Circle representing the turning area of the tracked combine harvester

4.2 Materials and Methods

4.2.1 System platform and sensors

An AG1100 Yanmar Tracked Combine harvester was equipped with Real Time Kinematic Global Positioning System (RTK-GPS) and Inertial Measurement Unit (IMU). The IMU provides 9 axes, consisting of 3 accelerometers, 3 magnetometers and 3 rate gyros, which was sampled at a rate of 200 Hz. In addition, the update rate of RTK-GPS is up to 20 Hz. But for logging the RTK-GPS output, the update rate is maintained 5 Hz or 10 Hz, where the IMU is also coincided with that update rate. The sensor measurements were logged into the control pc of tracked

combine harvester as a GGA header for RTK-GPS and VNIMU & VNYMR header for IMU. The GGA header from RTK-GPS sensor gives the position of the tracked combine harvester. On the other hand, the VNYMR header receives the bias compensated output such as yaw, roll, pitch, magnetic, acceleration, and angular rate measurements, whereas the VNIMU header provides the bias uncompensated IMU measurements such as magnetic, acceleration and angular rate measurements, temperature and pressure. In this chapter, the bias uncompensated output was used. The detailed about the combine harvester, RTK-GPS and IMU are described in chapter 2.

4.2.2 Tracked combine harvester model

In chapter 3, the tracked combine harvester dynamic model is described in detailed. The equations of dynamic model for the tracked combine harvester are written as follows:

$$m\ddot{x}_c = F_R + F_L - R_R - R_L - F_c \sin\beta \quad (4.1)$$

$$m\ddot{y}_c = F_c \cos\beta - \mu mg \quad (4.2)$$

$$I\ddot{\phi} = \frac{[(F_R - R_R) - (F_L - R_L)]B}{2} - M_r \quad (4.3)$$

Using the Eq. (3.26), the above equations can be rewritten by the Eq. (4.4).

$$\begin{bmatrix} \dot{X}_c \\ \dot{Y}_c \\ \dot{\phi} \end{bmatrix} = \begin{bmatrix} \left(\frac{1}{m} (F_R + F_L - R_R - R_L - F_c \sin\beta) \cos\varphi - \frac{1}{m} (F_c \cos\beta - \mu mg) \sin\varphi \right) \Delta t \\ \left(\frac{1}{m} (F_R + F_L - R_R - R_L - F_c \sin\beta) \sin\varphi + \frac{1}{m} (F_c \cos\beta - \mu mg) \cos\varphi \right) \Delta t \\ \left(\frac{[(F_R - R_R) - (F_L - R_L)]B}{2} - M_r \right) \frac{\Delta t}{I} \end{bmatrix} \quad (4.4)$$

The discrete-time process model is developed from the continuous-time process model, where the state space equation is obtained by integrating the

continuous-time equations over the interval from t_k to t_{k+1} . And, the discrete-time model is an approximation of the continuous-time model. Now, the discretization of the Eq. (4.4) can be written by the following Eq. (4.5).

$$\begin{bmatrix} \dot{X}_{k+1} \\ X_{k+1} \\ \dot{Y}_{k+1} \\ Y_{k+1} \\ \dot{\varphi}_{k+1} \\ \varphi_{k+1} \end{bmatrix} = \begin{bmatrix} \dot{X}_k + \left(\frac{1}{m}(F_R + F_L - R_R - R_L - F_c \sin\beta)\cos\varphi - \frac{1}{m}(F_c \cos\beta - \mu mg)\sin\varphi\right)\Delta t \\ X_k + \dot{X}_k \Delta t + \left(\frac{1}{m}(F_R + F_L - R_R - R_L - F_c \sin\beta)\cos\varphi - \frac{1}{m}(F_c \cos\beta - \mu mg)\sin\varphi\right)\frac{\Delta t^2}{2} \\ \dot{Y}_k + \left(\frac{1}{m}(F_R + F_L - R_R - R_L - F_c \sin\beta)\sin\varphi + \frac{1}{m}(F_c \cos\beta - \mu mg)\cos\varphi\right)\Delta t \\ Y_k + \dot{Y}_k \Delta t + \left(\frac{1}{m}(F_R + F_L - R_R - R_L - F_c \sin\beta)\sin\varphi + \frac{1}{m}(F_c \cos\beta - \mu mg)\cos\varphi\right)\frac{\Delta t^2}{2} \\ \dot{\varphi}_k + \left(\frac{[(F_R - R_R) - (F_L - R_L)]B}{2} - M_r\right)\frac{\Delta t}{I} \\ \varphi_k + \dot{\varphi}_k \Delta t + \left(\frac{[(F_R - R_R) - (F_L - R_L)]B}{2} - M_r\right)\frac{\Delta t^2}{2I} \end{bmatrix} \quad (4.5)$$

4.2.3 RTK-GPS and IMU Fusion Algorithm

In order to high speed turning of the tracked combine harvester, the yaw rate measurement from the IMU sensor will give bias which requires compensating for estimating the absolute heading. In this reason, the model in given Eq. (4.5) was used to estimate the heading of tracked combine harvester by using non-linear extended kalman filter. According to the given Eq. (4.5), the state vector of tracked combine harvester was defined as the Eq. (4.6).

$$X_{k+1} = [X_{k+1}, Y_{k+1}, \dot{X}_{k+1}, \dot{Y}_{k+1}, \dot{\varphi}_{k+1}, \varphi_{k+1}, \varphi_{gk+1}, b_{k+1}]^T \quad (4.6)$$

Where,

X_{k+1} = Tracked combine harvester position in east direction at time t_{k+1} ;

Y_{k+1} = Tracked combine harvester position in north direction at time t_{k+1} ;

\dot{X}_{k+1} = Tracked combine harvester velocity in X-direction at time t_{k+1} ;

\dot{Y}_{k+1} = Tracked combine harvester velocity in Y-direction at time t_{k+1} ;

$\dot{\phi}_{k+1}$ = Yaw rate at time t_{k+1} ;

φ_{k+1} = Heading of tracked combine harvester at time t_{k+1} ;

φ_{gps} = Heading from RTK-GPS at time t_{k+1} ; and

b_{k+1} = Yaw rate gyro measurement bias at time t_{k+1} ;

The system measurement vector is defined by the following Eq. (4.7).

$$Z_{k+1} = [X_{gps}, Y_{gps}, \dot{\phi}_{imu}, \varphi_{gps}]^T \quad (4.7)$$

Where,

X_{gps} = Measurement position in east direction from RTK-GPS;

Y_{gps} = Measurement position in north direction from RTK-GPS;

$\dot{\phi}_{imu}$ = Yaw rate gyro measurement from IMU; and

φ_{gps} = Measurement heading from RTK-GPS;

In chapter 2, the working principle of kalman and extended kalman filter were discussed. The extended kalman filter equations in the following Eqs. (4.8) and (4.9) are considered for prediction and correction steps; which is maintained in a cyclic manner. The initial state covariance matrix, process noise covariance matrix and

measurement noise covariance matrix are used, which was measured by the static and dynamic test of each sensor.

Prediction:

$$\begin{aligned}
 & \text{Predicted state, } X_{k+1} = f(X_k, u_k) \\
 & \text{Predicted covariance, } P_{k+1} = A_k P_k A_k^T + Q_k \\
 & \text{Predicted measurement, } Z_{k+1} = h(X_{k+1})
 \end{aligned}
 \quad \left. \vphantom{\begin{aligned} & \text{Predicted state, } X_{k+1} = f(X_k, u_k) \\ & \text{Predicted covariance, } P_{k+1} = A_k P_k A_k^T + Q_k \\ & \text{Predicted measurement, } Z_{k+1} = h(X_{k+1}) \end{aligned}} \right\} \quad (4.8)$$

Correction:

$$\begin{aligned}
 & \text{Estimate state, } \bar{X}_{k+1} = X_{k+1} + K v_k \\
 & \text{Estimate covariance, } \bar{P}_{k+1} = P_{k+1} (I - K H_k)
 \end{aligned}
 \quad \left. \vphantom{\begin{aligned} & \text{Estimate state, } \bar{X}_{k+1} = X_{k+1} + K v_k \\ & \text{Estimate covariance, } \bar{P}_{k+1} = P_{k+1} (I - K H_k) \end{aligned}} \right\} \quad (4.9)$$

Where,

$$\text{Innovation or measurement residual, } v_k = Z_{k+1} - h(X_{k+1})$$

$$\text{Kalman gain, } K = P_{k+1} H_k^T S^{-1}$$

$$\text{Innovation (or residual) covariance, } S = H_k P_{k+1} H_k^T + R_k$$

Jacobian matrix of A_k and H_k are

$$A_k = \frac{\partial f}{\partial x} = \begin{bmatrix} \frac{\partial f_1}{\partial x_1} & \dots & \frac{\partial f_1}{\partial x_m} \\ \vdots & \ddots & \vdots \\ \frac{\partial f_n}{\partial x_1} & \dots & \frac{\partial f_n}{\partial x_m} \end{bmatrix} \quad \text{and,} \quad H_k = \frac{\partial h}{\partial x} = \begin{bmatrix} \frac{\partial h_1}{\partial x_1} & \dots & \frac{\partial h_1}{\partial x_m} \\ \vdots & \ddots & \vdots \\ \frac{\partial h_n}{\partial x_1} & \dots & \frac{\partial h_n}{\partial x_m} \end{bmatrix}$$

P_k is the initial state covariance matrix, where

$$P_k = \begin{bmatrix} 0.0028 & 0 & 0 & 0 & 0 & 0 & 0 & 0 \\ 0 & 0.0028 & 0 & 0 & 0 & 0 & 0 & 0 \\ 0 & 0 & 0.01 & 0 & 0 & 0 & 0 & 0 \\ 0 & 0 & 0 & 0.01 & 0 & 0 & 0 & 0 \\ 0 & 0 & 0 & 0 & 0.0008 & 0 & 0 & 0 \\ 0 & 0 & 0 & 0 & 0 & 0.0015 & 0 & 0 \\ 0 & 0 & 0 & 0 & 0 & 0 & 0.005 & 0 \\ 0 & 0 & 0 & 0 & 0 & 0 & 0 & 0.0007 \end{bmatrix}$$

Q_k is the process noise covariance matrix, where

$$Q_k = \begin{bmatrix} 0.002909839 & 0 & 0 & 0 & 0 & 0 & 0 & 0 \\ 0 & 0.002909839 & 0 & 0 & 0 & 0 & 0 & 0 \\ 0 & 0 & 0 & 0 & 0 & 0 & 0 & 0 \\ 0 & 0 & 0 & 0 & 0 & 0 & 0 & 0 \\ 0 & 0 & 0 & 0 & 0.000781853 & 0 & 0 & 0 \\ 0 & 0 & 0 & 0 & 0 & 0.001350055 & 0 & 0 \\ 0 & 0 & 0 & 0 & 0 & 0 & 0.00508 & 0 \\ 0 & 0 & 0 & 0 & 0 & 0 & 0 & 0 \end{bmatrix}$$

R_k is the measurement noise covariance matrix, where

$$R_k = \begin{bmatrix} 0.00000297878 & 0 & 0 & 0 \\ 0 & 0.00000297878 & 0 & 0 \\ 0 & 0 & 0.000000438461 & 0 \\ 0 & 0 & 0 & 0.010348 \end{bmatrix}$$

4.3 Results and Discussion

4.3.1 Trajectory of Tracked Combine Harvester

For estimating the heading of tracked combine harvester by compensating yaw rate gyro measurement bias at non-linear condition, the tracked combine harvester was run in circular and sinusoidal shapes, during this time, the sensor measurements were logged, and the running trajectory of the tracked combine harvester can be obtained by using RTK-GPS position. Figure 4-2 shows the circular trajectories of the tracked combine harvester for the different input steering commands that were at 10 deg., 15 deg., 20 deg. and 25 deg., respectively. The turning radius of these circular trajectories can also be obtained by using the Eq. (3.24) that was discussed in chapter 3. On the other hand, the sinusoidal trajectories of the tracked combine harvester was made by a series of input steering commands such as ± 20 deg., ± 30 deg., ± 40 deg. and ± 50 deg., respectively as shown in figure 4-3.

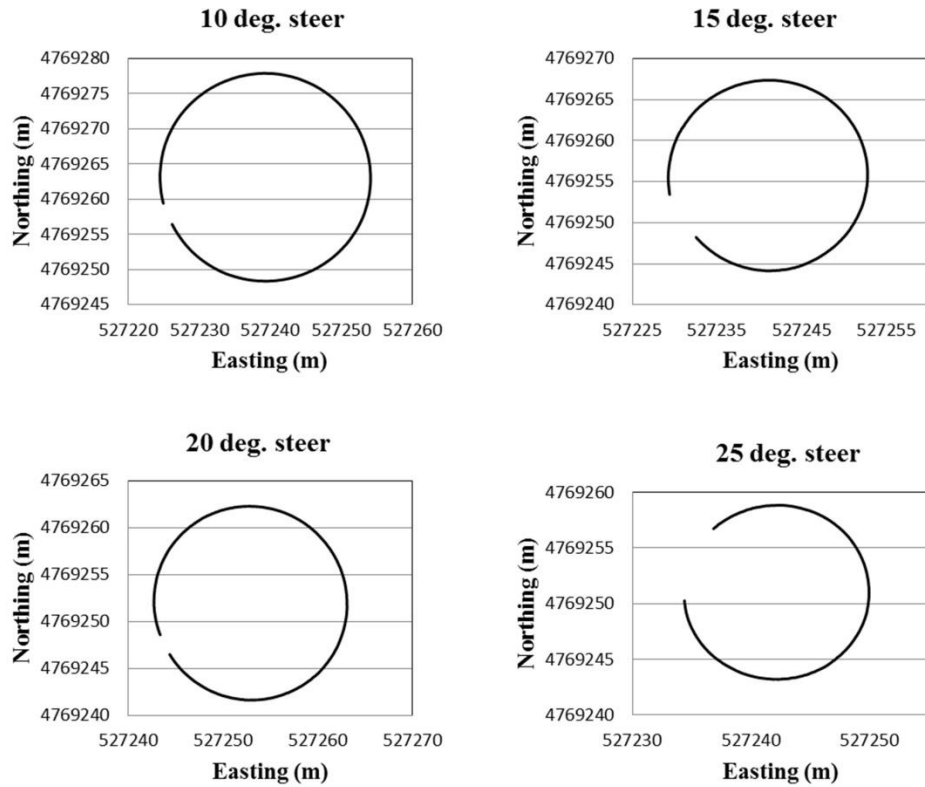


Figure 4-2. Circular trajectories of the tracked combine harvester at different input steering angles

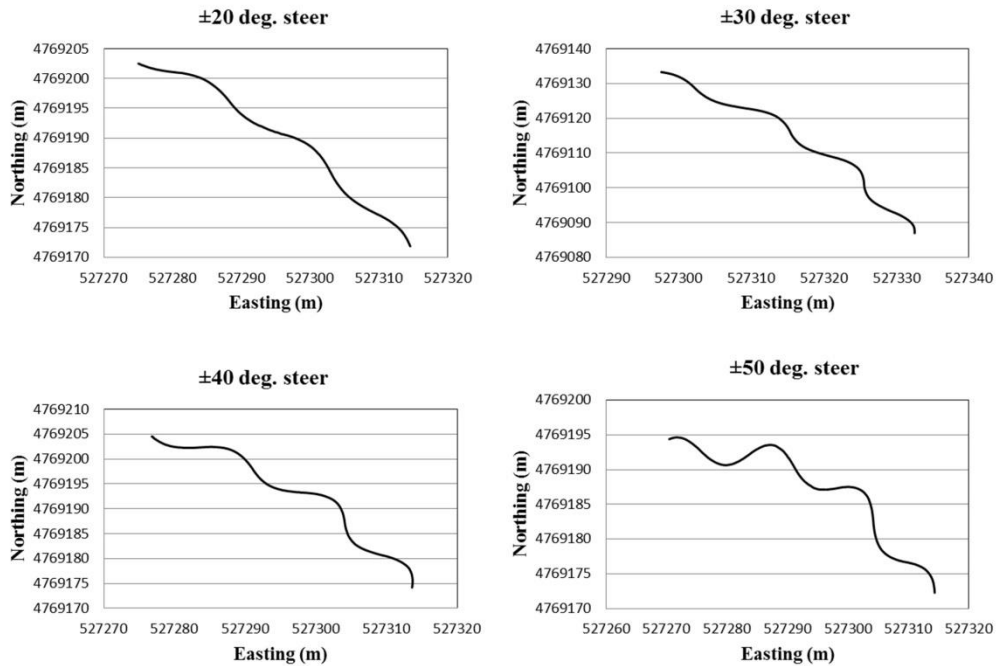


Figure 4-3. Sinusoidal trajectories of the tracked combine harvester at different input steering angles

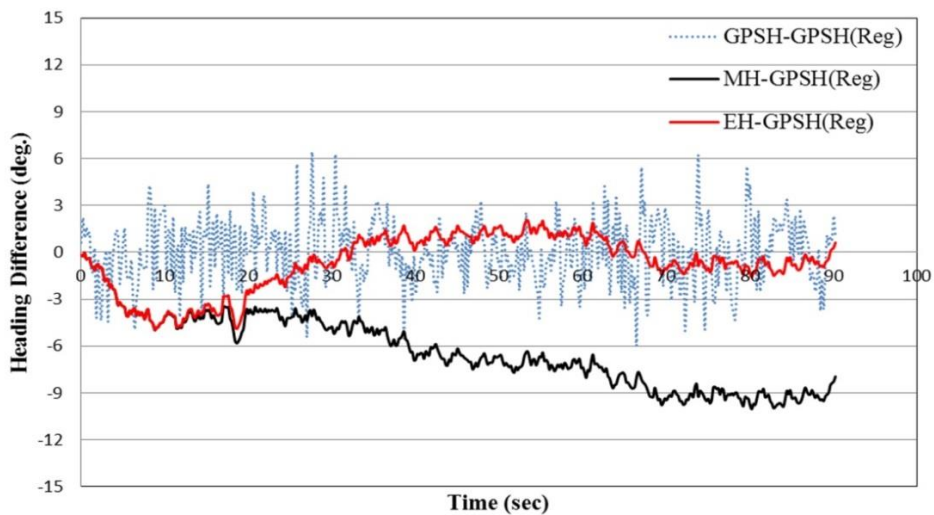
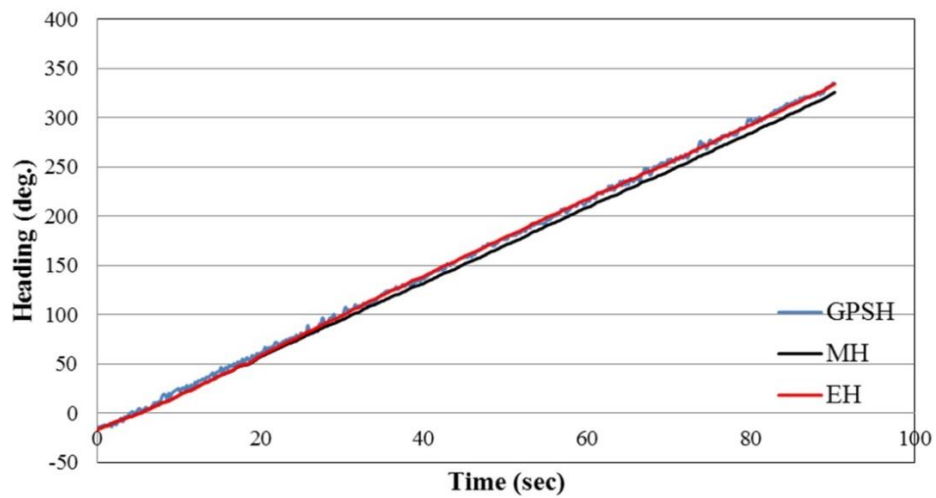
4.3.2 Estimated Heading of Circular Trajectory

Figure 4-4 indicates the measured and estimated heading (top figures) of circular trajectories as well as the difference of these headings from the reference GPS heading (bottom figures) which was obtained by linear regression of noisy trend GPS heading. The heading from GPS measurement is indicated by blue line, where the measured and estimated headings are marked by the black and red lines. In general, a full rotation of circle is counted to 360 deg., and when the tracked combine harvester was run in the field with a constant steering command, therefore, a full trajectory of circle will be 360 deg. That why, the top figures 4-4 (a) to (d) indicates that the output headings were bounded by 360 deg. According to these figures, the red line was tried to follow the blue one, which means the estimated heading consistent to the GPS heading. In addition, the heading difference analysis was shown in bottom figure 4-4, which indicates the difference of the measured and estimated headings from the reference GPS heading. Since, the GPS heading provides the exact direction of vehicle that is computed from the exact position of the tracked combine harvester, the linear regression of GPS heading was used as a reference GPS heading for the analysis of headings difference in this chapter. The result figured out that the estimated heading (red line) concentrates with the reference GPS heading for all circular trajectories as show in figure (bottom) 4-4.

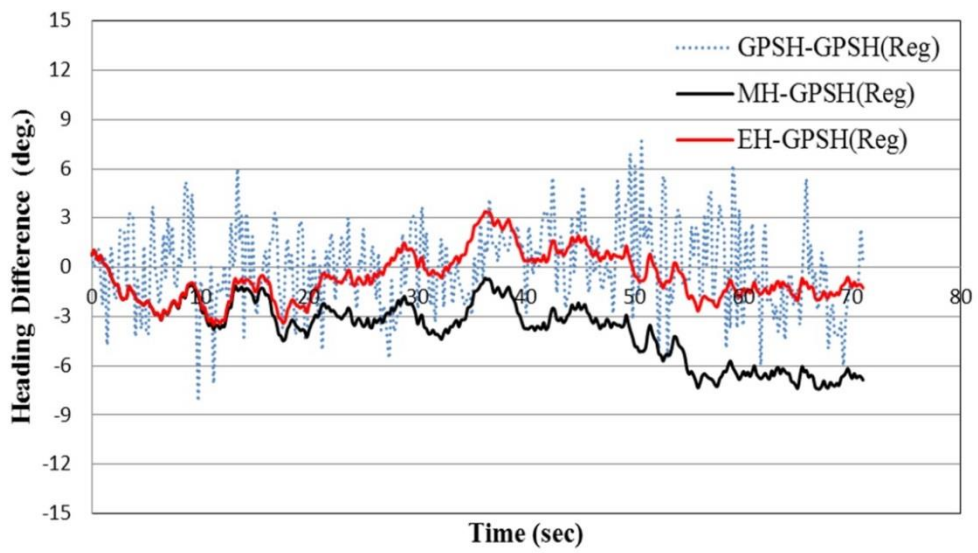
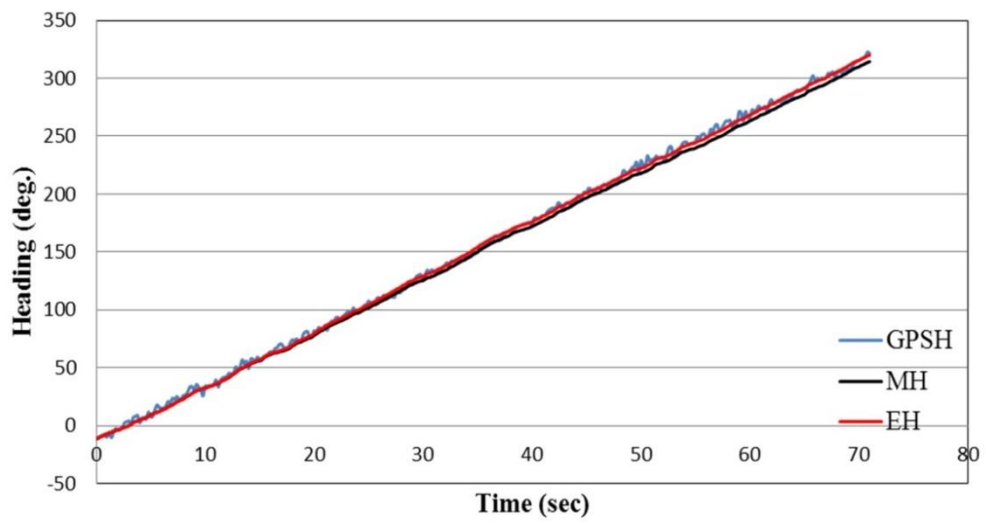
From the error analysis of these headings, the RMS errors between the measured or estimated heading and the reference GPS heading were calculated, which is given in the table 4-1. The RMS errors for the estimated heading are lower than the measured heading for all circular trajectories, and it indicates that the heading drift errors caused from the yaw rate gyro measurement bias is compensated, and the estimated heading concentrates to the reference GPS heading than measured heading.

Table 4-1. RMS errors for Measured and Estimated heading

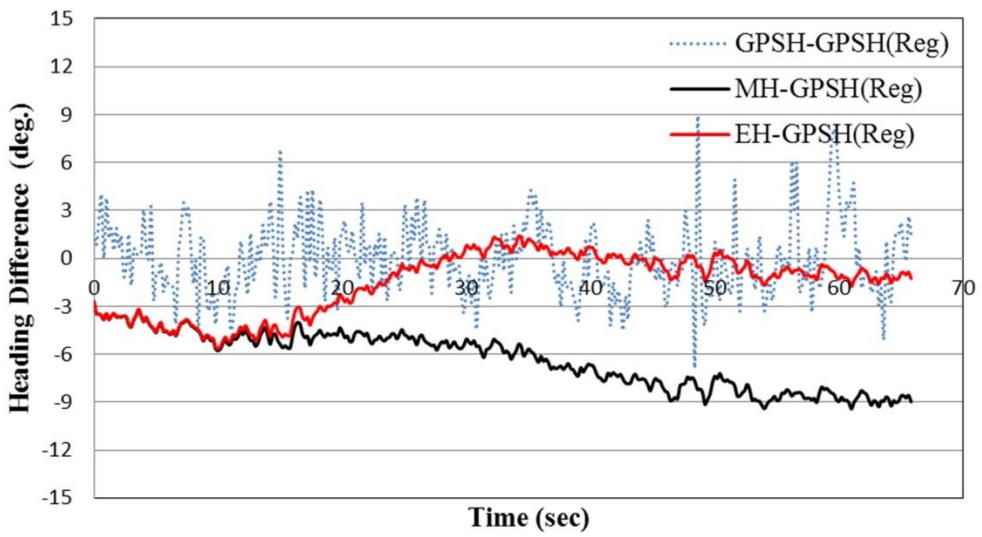
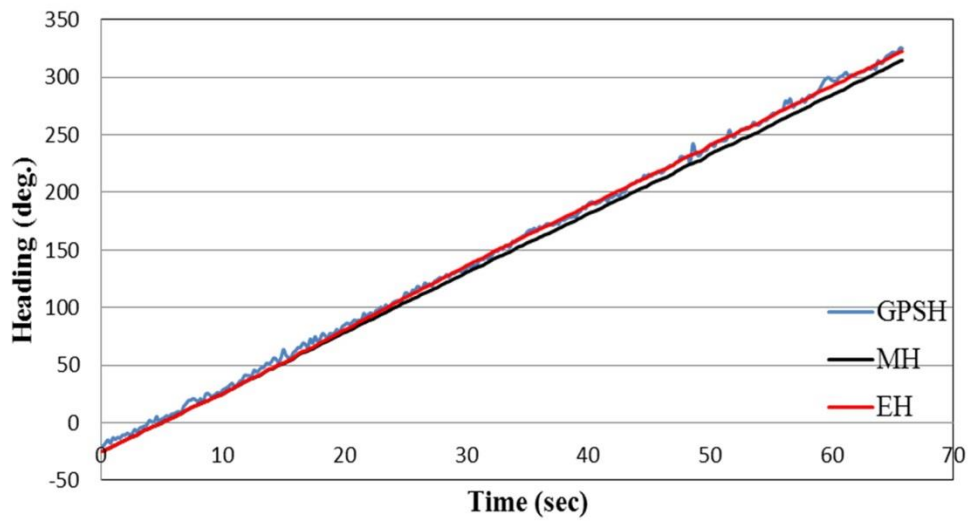
	RMS errors for circular trajectories when steering commands are at			
	10 deg.	15 deg.	20 deg.	25 deg.
Measured Heading (MH)	6.74	4.18	6.58	4.42
Estimated Heading (EH)	1.93	1.58	2.44	2.02



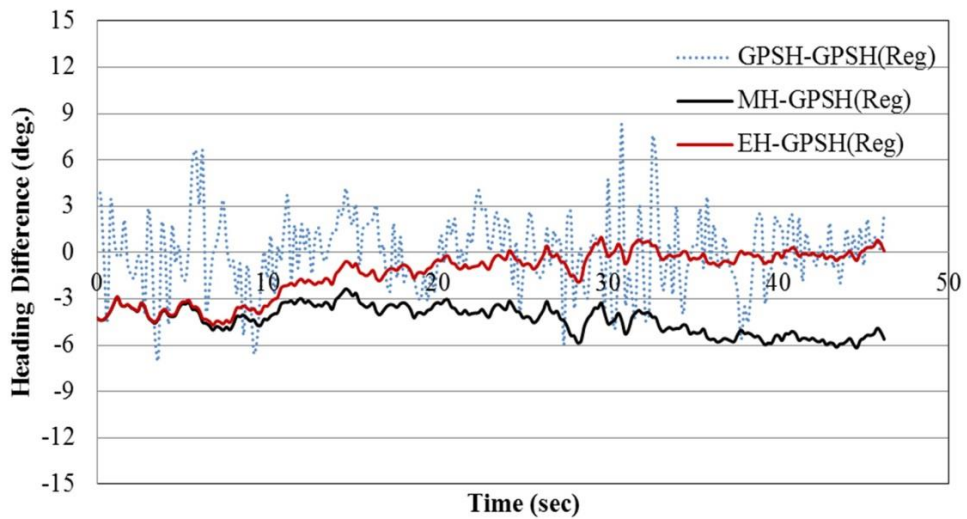
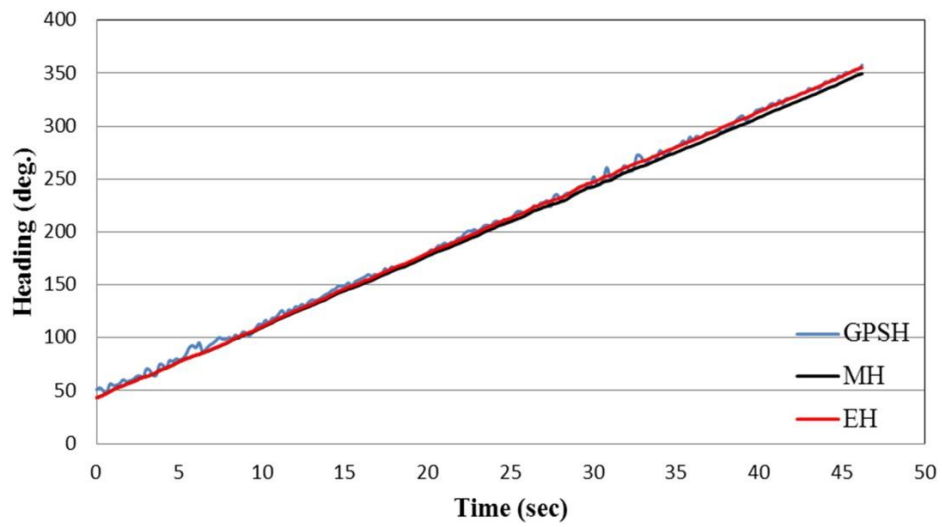
(a) Heading for 10 deg. Steering



(b) Heading for 15 deg. Steering



(c) Heading for 20 deg. Steering



(d) Heading for 25 deg. Steering

Figure 4-4. Measured and estimated headings (top figures) for circular trajectories as well as heading difference (below figures). (Where, GPSH = GPS Heading, MH = Measured Heading, EH = Estimated Heading and GPSH (Reg) = Linear Regression of GPS Heading)

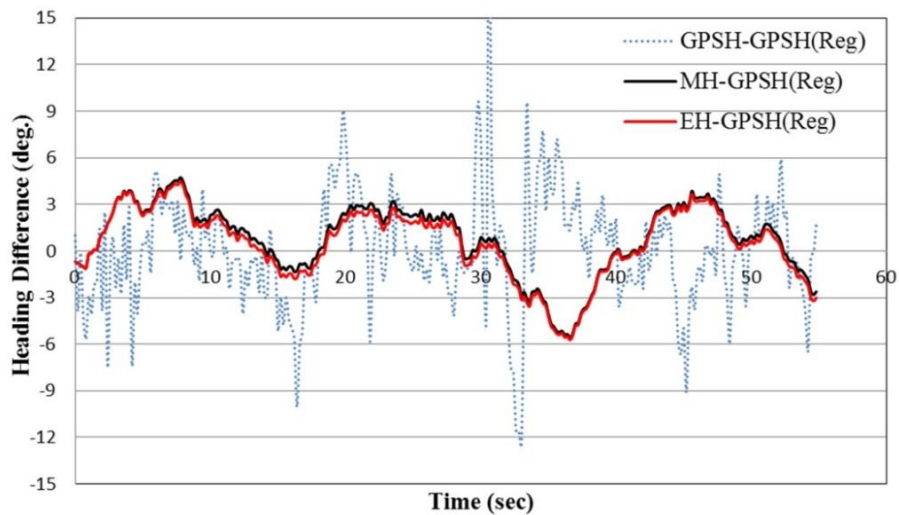
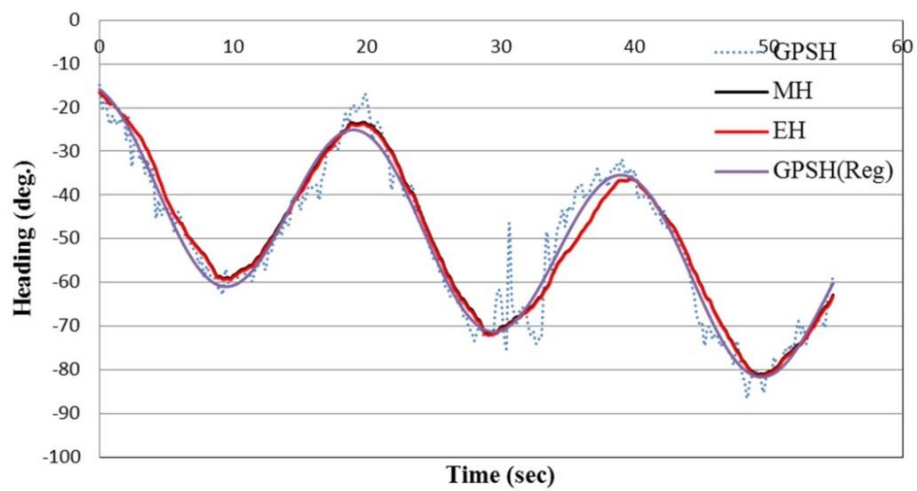
4.3.3 Estimated Heading of Sinusoidal Trajectory

Figure 4-5 shows the measured and estimated heading (top figures) and heading difference between the measured or estimated heading and the non-linear regression of GPS heading (bottom figures). The purple color line in top figures indicates the non-linear regression of GPS heading which was obtained by using the Gauss-Newton algorithm, called the reference GPS heading. Gauss-Newton algorithm is a simple method for solving any non-linear regression problem, and the equation for non-linear regression analysis was considered as $Y_i = A \sin\left(\frac{X_i}{T} + \theta\right) + aX_i + b$, where A , T , θ , a and b are the amplitude, period, phase shift angle, phase shift (horizontally) and vertical shift, respectively. On the other hand, the black and red color lines were represented by the measured and estimated heading. According to the figure 4-5, the estimated heading is better than measured heading and it tried to concentrate with the reference GPS heading.

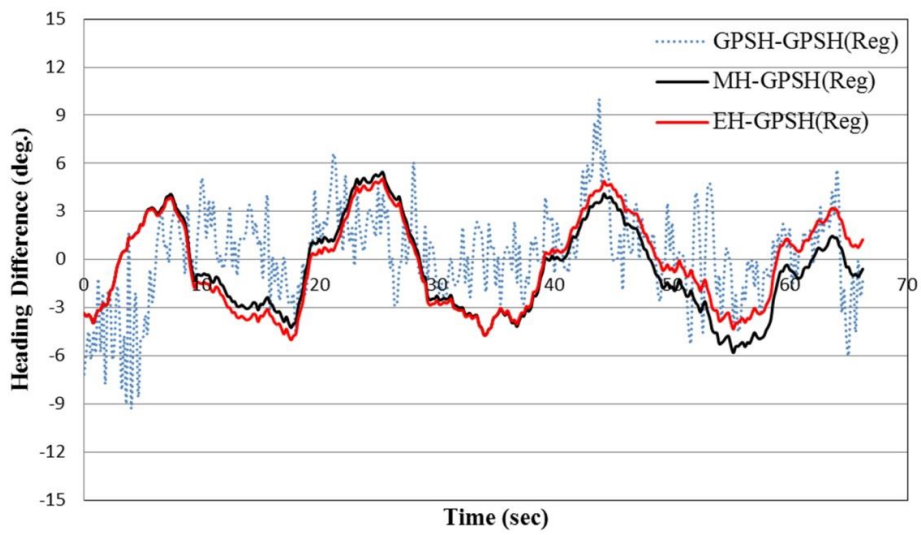
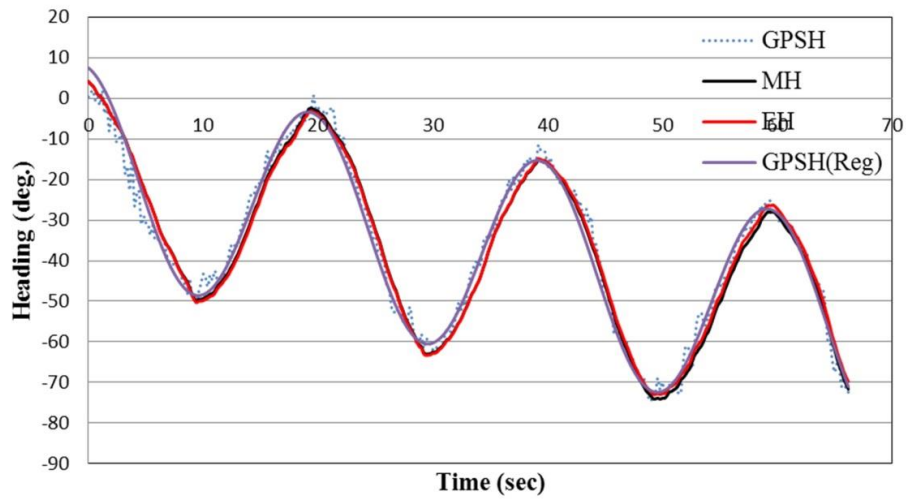
From the error analysis of measured and estimated heading regarding the reference GPS heading in the table 4-2, the RMS errors for measured and estimated heading seem almost same, because the reference GPS heading is sometimes matched with noisy trend GPS heading, and sometimes not matched. If the reference GPS heading matches with the exact GPS heading, the RMS error of measured and estimated heading will be changed, and the RMS error of estimated heading will be lower than measured heading. Besides, the heading difference in bottom figure 4-5 indicates that the estimated heading is trying to concentrate to the reference GPS heading than that of measured heading. The results also mean that the measured heading contains drift error as IMU is corrupted by biases, whereas the estimated heading is considered drift free.

Table 4-2. RMS errors for measured and estimated heading

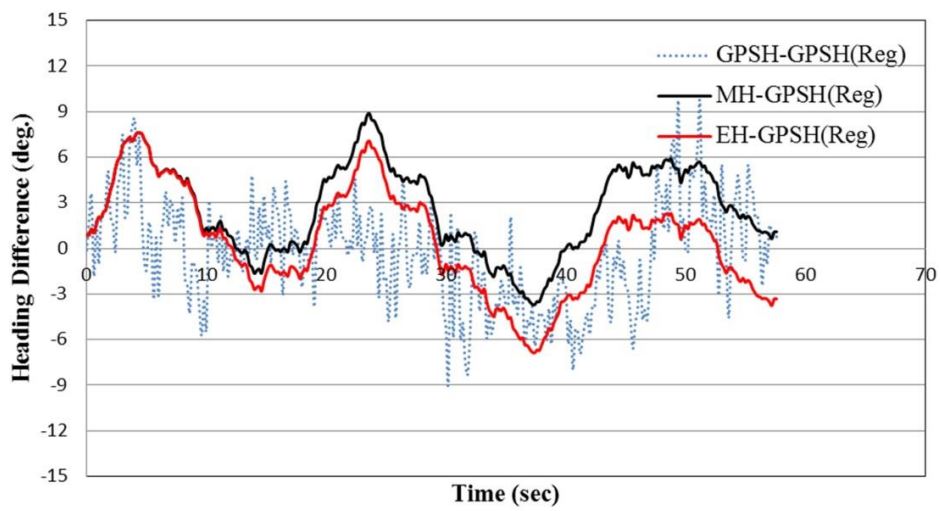
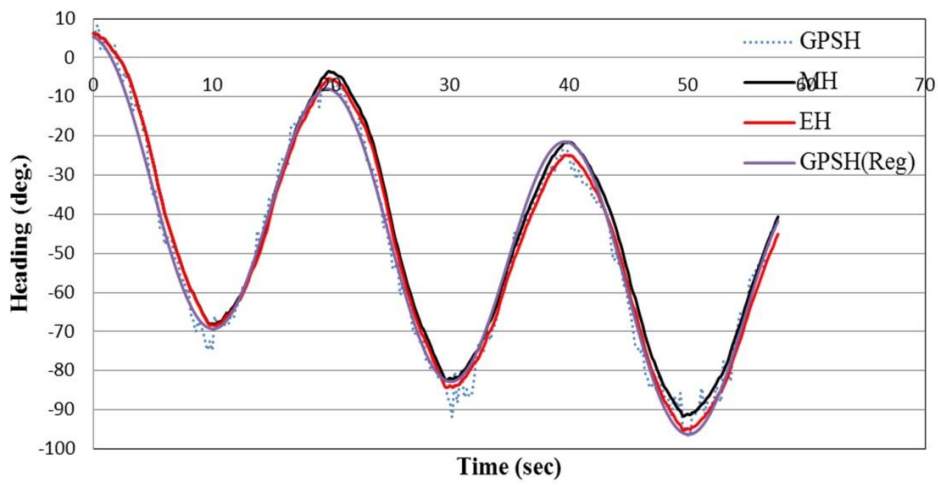
	RMS errors for sinusoidal trajectories when steering commands are at			
	± 20 deg.	± 30 deg.	± 40 deg.	± 50 deg.
Measured Heading (MH)	2.39	2.90	3.96	5.78
Estimated Heading (EH)	2.29	2.84	3.48	5.08



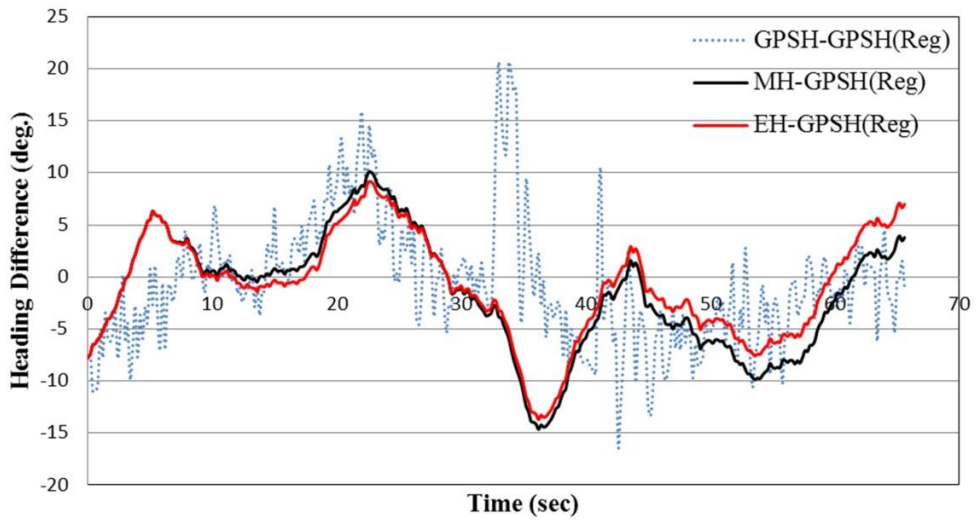
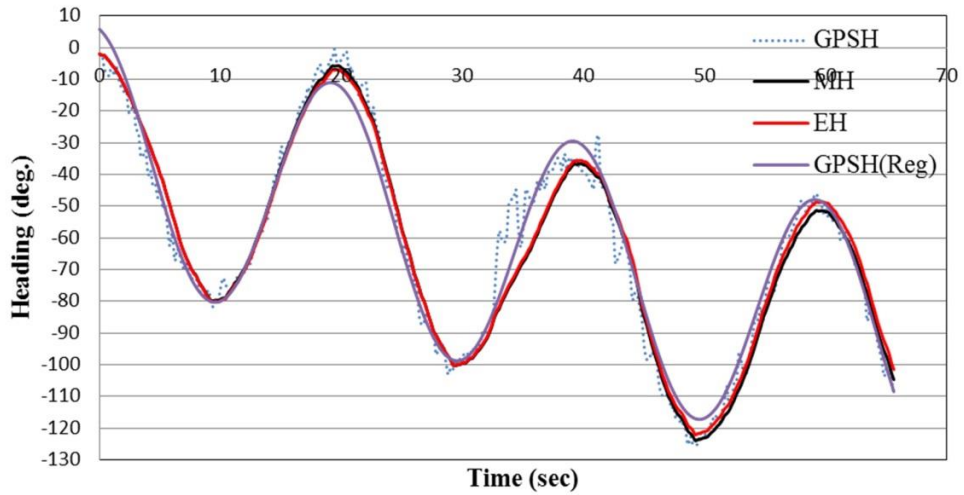
(a) Heading for 20 deg. Steering



(b) Heading for 30 deg. Steering



(c) Heading for 40 deg. Steering



(d) Heading for 50 deg. Steering

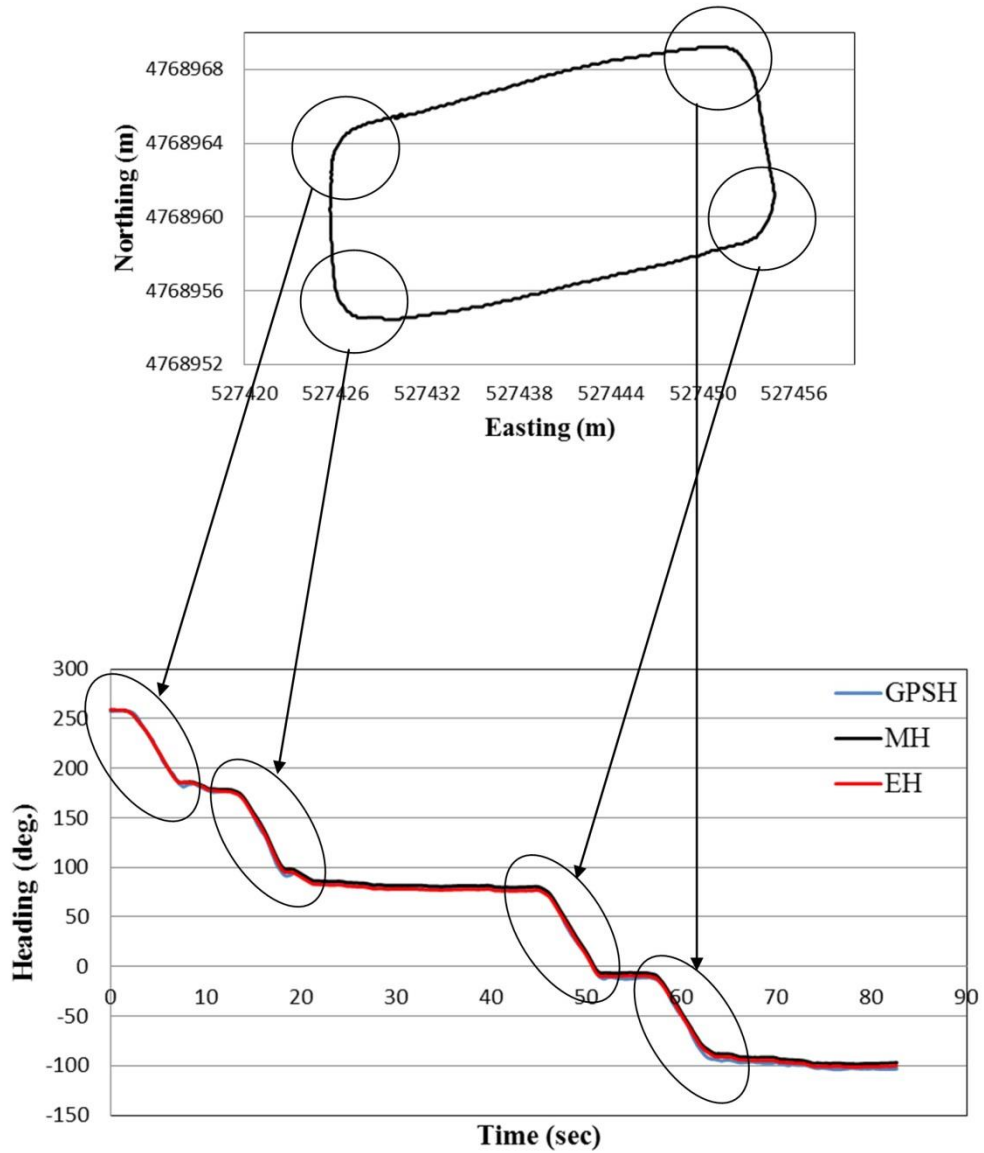
Figure 4-5. Measured and estimated headings (top figures) for sinusoidal trajectories as well as heading difference (below figures). (Where, GPSH = GPS Heading, MH = Measured Heading, EH = Estimated Heading and GPSH (Reg) = Linear Regression of GPS Heading)

4.3.4 Estimated heading of convex and concave polygon field

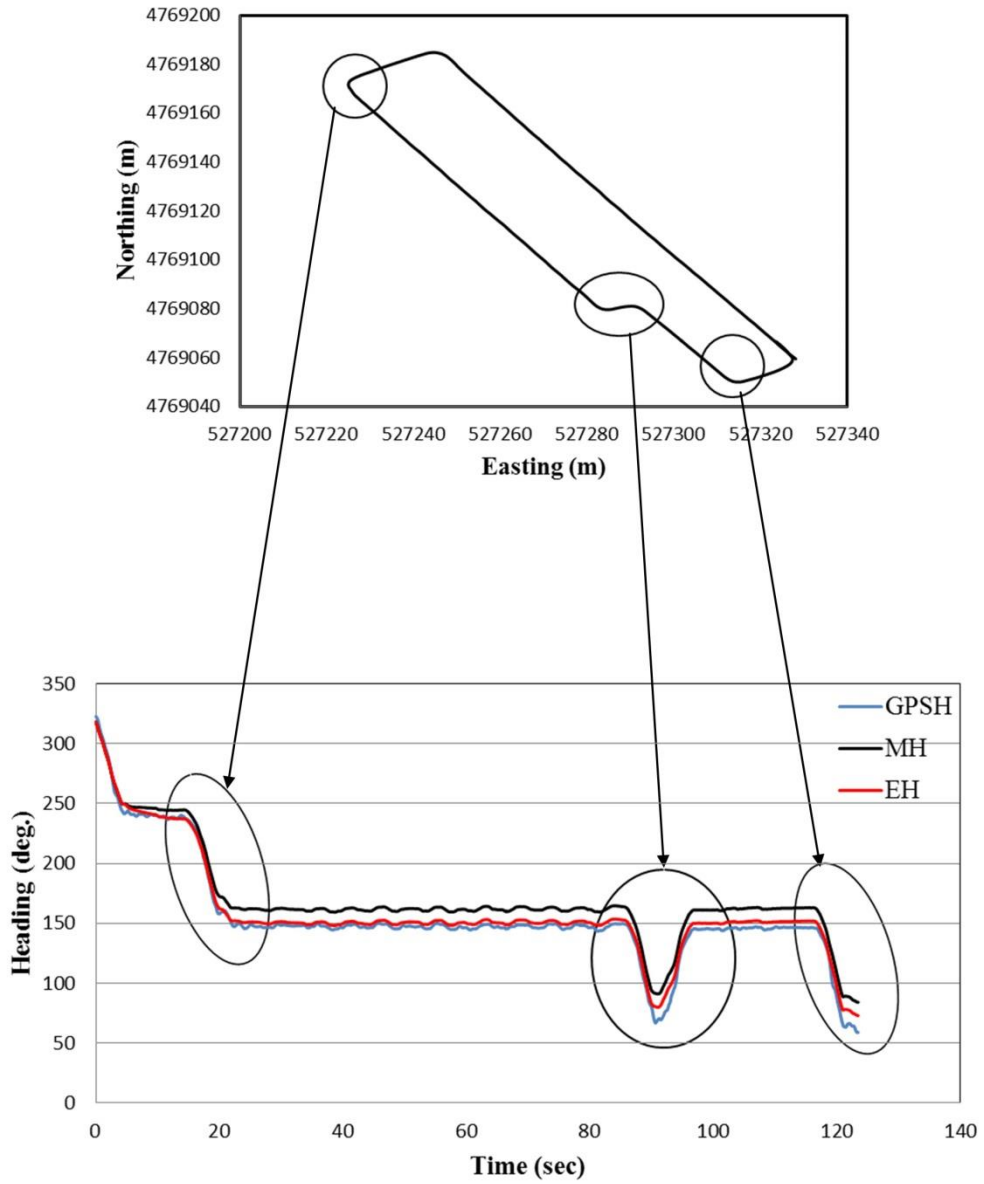
The heading estimation method based on the tracked combine harvester dynamic model and the extended kalman filter was evaluated for a convex and concave polygon field as shown in figure 4-6. The circle mark on the convex and concave polygon field indicates the turning position of the tracked combine harvester. In these circle positons, the tracked combine harvester turned at high speed with considering low turning radius, which creates yaw rate gyro measurement bias. This bias creates the measured heading drift that is important to compensate. Figure 4-6 (a) shows a heading of rectangular field where the red and black lines are marked for the measured and estimated heading, which was analyzed with respect to the reference GPS heading (blue color line). The reference GPS heading (indicated by GPSH(Reg)) was obtained from the moving average of noisy trend GPS heading. The difference of heading was calculated between the measured heading or estimated heading and the reference GPS heading shown in figure 4-7 (a). The RMS error was calculated from the measured or estimated heading and the reference GPS heading, and from the error analysis, the RMS errors for measured and estimating heading were 4.07 deg. and 2.08 deg., respectively. Since, the RMS error of estimated heading is lower than the measured heading, the estimated heading shows more consistent with the reference GPS heading.

In figure 4-6 (b), the measured and estimated heading were estimated from the concave polygon field as well as the heading difference between the two measurements with the reference GPS heading as given in figure 4-7 (b). The RMS errors for measured and estimated headings were 14.93 and 5.17 deg., respectively. This result means that the estimated heading is more consistent with the reference GPS heading than that of measured heading. In addition, the results also described

that the measured heading drift error was compensated by the extended kalman filter and the tracked combine harvester dynamic model.

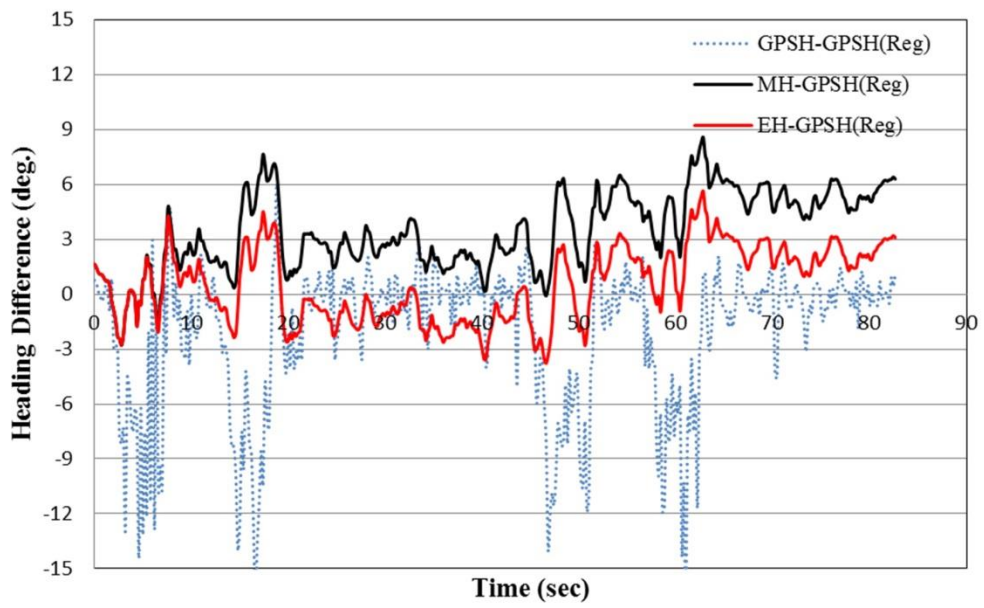


(a) Heading for rectangular field

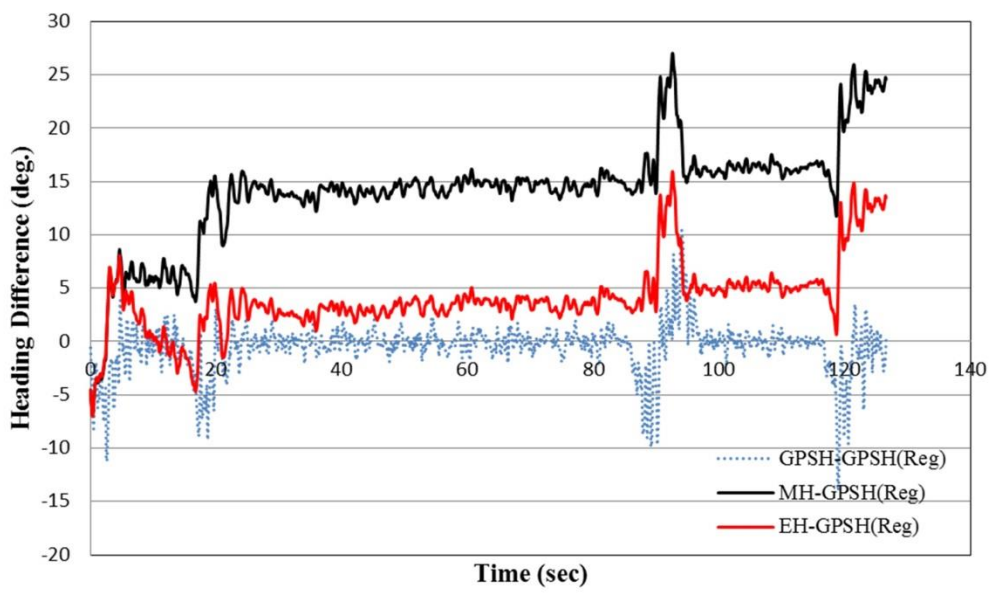


(b) Heading for concave field

Figure 4-6. Estimated heading for convex and concave polygon field during field



(a)



(b)

Figure 4-7. Heading difference for convex and concave polygon field

4.4 Conclusions

This chapter describes the tracked combine harvester dynamic model and the sensor fusion method like the extended kalman filter, which are used to estimate the absolute heading of tracked combine harvester in non-linear condition by compensating the yaw rate gyro measurement bias. Different set of experiments such as circular, sinusoidal, rectangular and concave shape were done to evaluate this estimation method. The experimental results for circular and sinusoidal trajectories reveal that the yaw rate gyro measurement bias was compensated based on the extended kalman filter and the tracked combine harvester dynamic model, and simultaneously the absolute heading was determined. Therefore, this method can be used to estimate absolute heading when the tracked combine harvester will take turn at high speed and high steering command in order to cut wheat and paddy nearby headland to calculate the header end position or exact outline of crops for the developing of harvesting map.

Chapter 5 Optimum Harvesting Area for Path Planning of Robot Combine Harvester

5.1 Introduction

Development of an agricultural robot means to make the operator's work easier in the agricultural industry. The concept of a robot is considered due to the decreasing of agricultural population, and the increasing their age. In general, a human operator is not able to operate a farm vehicle over a long period of time in the field, whereas agricultural robot vehicles with proper operational map can work frequently for long time in any adverse condition.

Reid (2004) stated that proper operational map or path planning for agricultural robot vehicles is one of the key tasks in the planning process. Field efficiency and operational costs with the use of high end technology is driven by the proper planning of field operation. The proper field operation reduces the production costs and increases the adoption of agricultural robots by the farmers (Rodrigo, 2012). A proper path planning or operational map is made based on some global and local sensors such as global positioning system, inertial measurement unit, laser scanner and camera for the operation of agricultural robot vehicles. This operational map should be as much as appropriate sothat whole field will cover or field will be optimized. That why, the field optimization is very important during the operation of agricultural robot vehicles; otherwise overall field efficiency will be reduced.

Autmatic path planning for the robot combine harvester developed by Zhang el al. (2013) is required to choose the crop field optimum harvesting area; otherwise,

crop losses may occur during harvesting in the field. In general, a boundary zone in the field includes some water inlets and outlets, or some objects that are very dangerous for a robot running. In order to make the turning margin safe for the robot combine harvester, the surrounding crop nearby boundary zone is cut twice or thrice by manual operation; however, this surrounding cutting crop is not exactly straight, sometimes it is curved or meandering. Mostly, this curved or meandering portion happens if the crop pattern is not in row. Moreover, in a conventional way, the path planning is made by using AB corner position and the parallel path is calculated based on the first path. Developing a path planning in a conventional AB position method, in order to take a corner position from the global positioning system by visual observation is a time consuming operation; the curved or meandering crop is not cut, and the harvesting area is not optimum. During harvesting, this curved or meandering crop may be left in the field. In order to consider the crop losses in the field and the operational processing time, an optimum harvesting area of convex or concave polygon form in the field is very important.

Therefore, in this chapter, the overall objective is to develop an algorithm that can estimate the optimum harvesting area for a convex or a concave polygon field, and determine the corner vertex to calculate the working path of a robot combine harvester.

5.2 Materials and methods

5.2.1 Research platform and sensors

A robot combine harvester developed by Zhang et al. (2013) was used that is designed to harvest cereal crops like paddy, wheat and soybean; which is equipped with an on-board computer to log data from the positioning and inertial sensors by using serial ports. Figure 5-1 shows the robot combine harvester equipped with

positioning and inertial sensors. In this research, 2 m and 2.5 m header was fixed with the robot combine harvester to cut the wheat. A Topcon GB-3 GPS receiver with a PG-S1 antenna was used to receive the RTK-GPS position, where the low latency configuration (update rate: 5 or 10 Hz, data link: 115200 Baud) was selected for the RTK mode in this research. On the other hand, IMU was equipped to the robot combine harvester for measuring the direction angle. The output data from the IMU was logged into the control pc at a frequency of 200 Hz through a USB serial port.



Figure 5-1. Robot combine harvester equipped with RTK-GPS position and IMU direction sensors

5.2.2 Automatic Path planning algorithm

Overall automatic path planning algorithm for the robot combine harvester is described as shown in figure 5-2.

Firstly, the measured RTK-GPS position $P(X_i, Y_i)$ and heading angle φ were used to calculate the header end position $P(X_H, Y_H)$, which is called the crop perimeter or the exact outline of a crop.

Secondly, the convex hull CH ($p_0, p_1 \dots p_i$) was obtained from the computed crop perimeter position $P(X_H, Y_H)$ by using the incremental convex hull method (Kallay, 1984).

Thirdly, the actual field shape was selected from the estimated convex hull. When the shape of field is a rectangular polygon, the optimum harvesting area of rectangular field was determined by using the rotating caliper method, which estimates the corner vertices $V(X_i, Y_i)$ to calculate the working path. But when the field shape is pentagon or L-shape polygon other than rectangular polygon, an N-polygon algorithm and the split of convex hull and cross point method were developed to estimate the corner vertices $V(X_i, Y_i)$ of that polygon.

Fourthly, the edges of the polygon were obtained using the estimated corner vertices $V(X_i, Y_i)$, which indicates the path direction called the first path. Using the first path, another path was calculated by using the header length.

Finally, as every path gives start and end points, the waypoints of every path were calculated and stored in a file of control pc. This file is the input file of the robot combine harvester for the completely automatic harvesting of a crop. These whole procedures are discussed in details in the following sections.

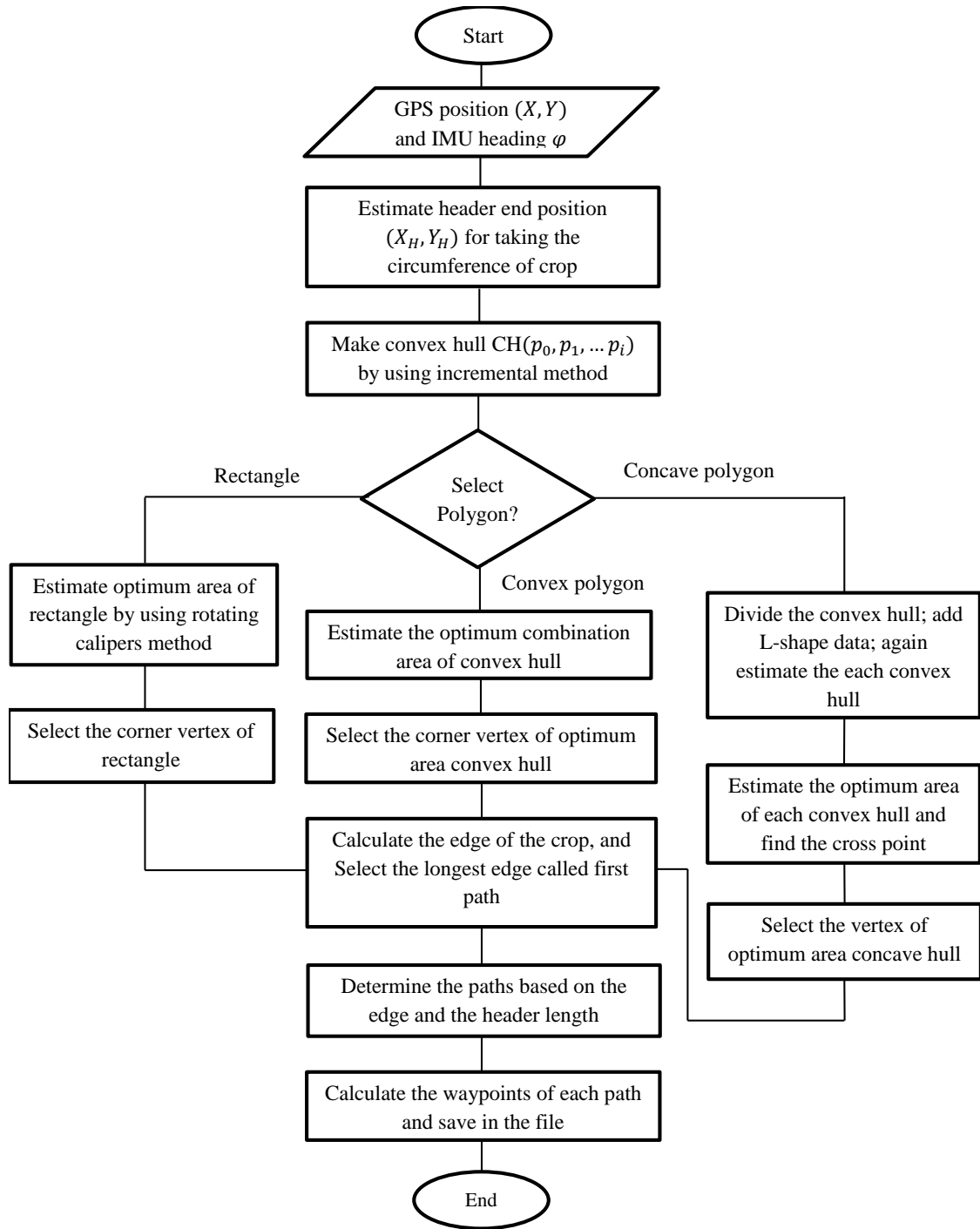


Figure 5-2. Automatic path planning algorithm of the robot combine harvester

5.2.3 Header end position

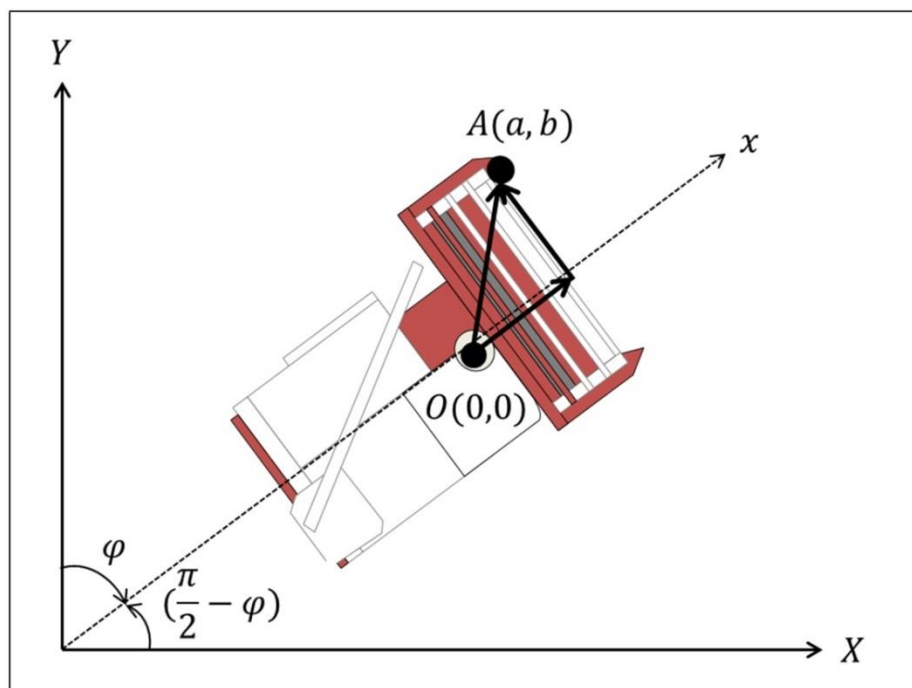


Figure 5-3. Heading angle of the robot combine harvester for estimating the header's end position

Header end position is calculated by using the RTK-GPS position and IMU heading angle for considering the safe turning of the robot combine harvester during its operation. To obtain a safe turning area for the robot combine harvester, the surrounding crop near to headland was cut twice or thrice in manual operation so that the water inlets and outlets in the field are not damaged. The RTK-GPS and IMU sensors were equipped on the robot combine harvester to receive the position $P(X_i, Y_i)$ and heading angle φ of that robot harvester. The header end position $P(X_H, Y_H)$ or the exact outline of a crop was determined from this measured RTK-

GPS position $P(X_i, Y_i)$ and IMU heading angle φ . Let us consider the relative coordinate system with the origin $O(0, 0)$ that coincides with the RTK-GPS position, and the x axis aligned with the vehicle forward direction, as shown in figure 5-3. The header's end position A is identified with the relative coordinates (a, b) . Parameters a and b indicate the distance between the header center to the GPS antenna and the header's center to header's end.

Hence, the header's end position (X_H, Y_H) is calculated by Eq. (5.1) in the ground coordinate system rotating along the vector OA by $(\frac{\pi}{2} - \varphi)$.

$$\begin{bmatrix} X_H \\ Y_H \end{bmatrix} = \begin{bmatrix} \cos(\frac{\pi}{2} - \varphi) & -\sin(\frac{\pi}{2} - \varphi) \\ \sin(\frac{\pi}{2} - \varphi) & \cos(\frac{\pi}{2} - \varphi) \end{bmatrix} \begin{bmatrix} a \\ b \end{bmatrix} + \begin{bmatrix} X_i \\ Y_i \end{bmatrix} \quad (5.1)$$

5.2.4 Convex hull algorithm

The convex hull method was briefly discussed in chapter 2. The convex hull of a set of points Q is defined as the smallest convex polygon P that contains all the points of it; which is expressed as $CH(Q)$. An incremental convex hull algorithm was developed by Kallay (1984) to make a convex hull $CH(Q)$ from a finite set of convex polygon points which are the RTK-GPS position $P(p_0, p_1 \dots p_i)$ points. This algorithm reduces the RTK-GPS position $P(p_0, p_1 \dots p_i)$ by consecutively selecting the outer most positions or points that cover all points inside of the convex hull as shown in figure 5-4. In this case, the point set Q is sorted clockwise to create a sort sequence of the convex hull $CH(p_0, p_1 \dots, p_i)$.

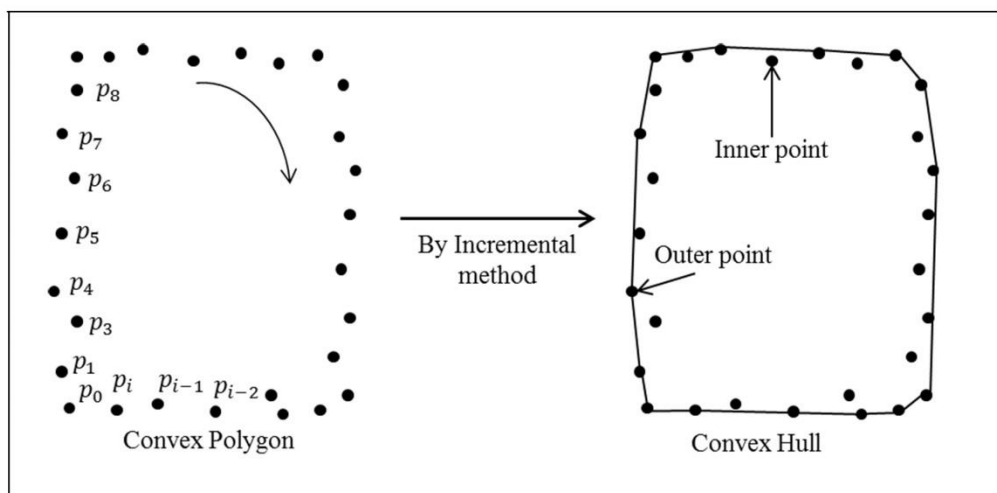


Figure 5-4. Convex hull from a finite set of RTK-GPS position of convex polygon

5.2.5 Optimum area of Rectangle by Rotating Caliper method

The optimum harvesting area enclosing rectangle was determined from the estimated convex hull $CH(Q)$ of a rectangle by using the rotating calipers method (Shamos, 1978; Godfried, 1983). In this method, consider $L_s(p_i, p_j, p_k, p_l)$ which indicates a straight line passing through p_i, p_j, p_k and p_l , as shown in figure 5-5. At first, the vertices $(p_i, p_j, p_k$ and $p_l)$ are selected based on the minimum or maximum x and y coordinates, which are rotated to build a set of calipers with an angle θ . After the rotation, the corners vertices of the rectangle was computed from the coordinates $(p_i, p_{i+1}, p_j, p_k$ and $p_l)$ while the optimum harvesting area of the rectangle was determined. In chapter 2, the rotating caliper method is described in details (Shamos, 1978; Godfried, 1983).

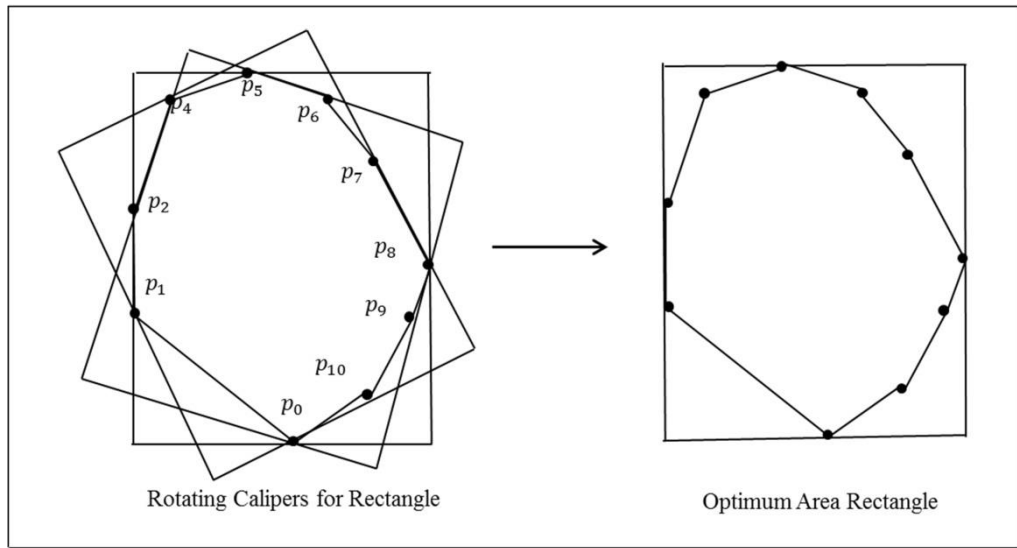


Figure 5-5. Optimum harvesting area of rectangle obtained by the Rotating Caliper method

5.2.6 Optimum area of Convex polygon from N-Polygon algorithm

The optimum harvesting area for a convex polygon was determined from the vertices of convex hull $CH(p_1, p_2, p_3, \dots, p_i)$ by using the developed N-polygon algorithm, which is described in counter clockwise order as shown in figure 5-6. The vertices p_i of the convex hull CH indicates the RTK-GPS position (X_i, Y_i) . By using these vertices p_i, p_{i+1} of the convex hull CH, the equation of i^{th} straight line was obtained. Let us consider the two straight i^{th} and j^{th} lines, described by the Eq. (5.2). The cross point $CP(X_i, Y_i)$ was calculated by using the Eqs. (5.2) which is indicated by the Eq.(5.3).

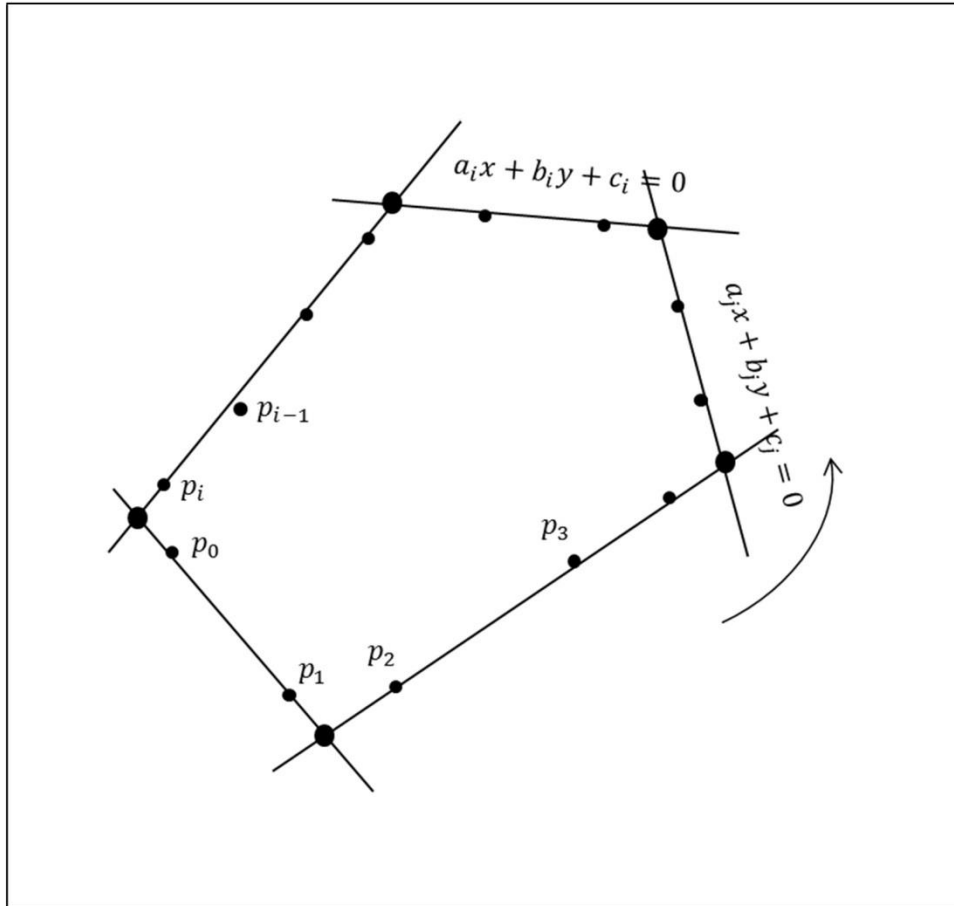


Figure 5-6. Optimum harvesting area of an N-angular shape polygon

$$\begin{pmatrix} a_i & b_i \\ a_j & b_j \end{pmatrix} \begin{pmatrix} X_i \\ Y_i \end{pmatrix} + \begin{pmatrix} c_i \\ c_j \end{pmatrix} = 0 \quad (5.2)$$

$$(X_i, Y_i) = \left(\frac{b_i c_j - b_j c_i}{a_i b_j - a_j b_i}, \frac{a_j c_i - a_i c_j}{a_i b_j - a_j b_i} \right) \quad (5.3)$$

Where a , b and c are the constant parameters that was calculated from the vertices of the convex hull CH ($p_1, p_2, p_3, \dots, p_i$) by the following Eqs. (5.4), (5.5) and (5.6). Here, j is equal to $i + 1$.

$$a_i = Y_{i+1} - Y_i \quad (5.4)$$

$$b_i = X_{i+1} - X_i \quad (5.5)$$

$$c_i = X_{i+1}Y_i - X_iY_{i+1} \quad (5.6)$$

By using the cross points $CP(X_i, Y_i)$ of a convex polygon and the vertices of convex hull $CH(p_1, p_2, p_3, \dots, p_i)$, the contour of polygon and the contour of convex hull were determined. The center of gravity point (G_x, G_y) was determined by the Eq. (5.7). This center of gravity point (G_x, G_y) is used for checking whether this point is inside or outside of convex polygon and convex hull.

$$\left. \begin{aligned} G_x &= \frac{C_x}{A} \\ G_y &= \frac{C_y}{A} \end{aligned} \right\} \quad (5.7)$$

Where, C_x and C_y indicates the centroid of a polygon that is calculated by Eqs. (5.8) and (5.9).

$$C_x = \frac{1}{6A} \sum_{i=0}^{n-1} (X_i + X_{i+1})(X_iY_{i+1} - X_{i+1}Y_i) \quad (5.8)$$

$$C_y = \frac{1}{6A} \sum_{i=0}^{n-1} (Y_i + Y_{i+1})(X_iY_{i+1} - X_{i+1}Y_i) \quad (5.9)$$

Finally, when the center of gravity is inside of polygon or convex hull, the cross point $CP(X_i, Y_i)$ was selected, and the area was determined by using the Eq. (5.10). This procedure is continued until the optimum harvesting area is obtained. Afterward, the corner vertices $V(X_i, Y_i)$ of convex polygon are selected based on the optimum harvesting area.

$$A = \frac{1}{2} \sum_{i=0}^{n-1} (X_iY_{i+1} - X_{i+1}Y_i) \quad (5.10)$$

5.2.7 Optimum area of Concave polygon from Concave hull algorithm

An algorithm was developed to estimate a concave hull CCH (Q) by the developed split of convex hull CH (Q) and cross point method which describes the

optimum area of concave polygon as shown in figure 5-7. To compute the optimum area of concave hull, this algorithm is described by the following four steps.

Step-1: Convex hull CH (Q) was determined from concave polygon which outline represents the RTK-GPS position $P(p_0, p_1 \dots p_i)$ points. The incremental convex hull algorithm was used to make convex hull from concave polygon. The optimum area of that convex hull was computed, which provides the corner vertices (X_i, Y_i) . These corner vertices were stored.

Step-2: When the optimum area of convex hull was determined, the L-shape data was added into this optimum area of the convex hull, which represents the concave hull $P(p_0, p_1 \dots p_i)$. Afterward, this concave hull was divided into two convex polygons. Again, the convex hull CH (Q) was estimated for each convex polygon. These estimated convex hull was used to calculate the optimum area of both convex hull CH (Q). The corner vertices of each optimum area of convex hull were stored.

Step-3: The cross point $CP(X_i, Y_i)$ was obtained by using the Eq. (5.3) from the optimum area of each convex hull CH (Q). This cross point $CP(X_i, Y_i)$ was stored with the corner vertices $V(X_i, Y_i)$ of the convex hull CH (Q).

Step-4: Using this cross point $CP(X_i, Y_i)$ and corner vertices $V(X_i, Y_i)$ of concave hull, the optimum area of the concave hull was determined. This estimated optimum area was stored in a memory stack. This procedure was continued until the optimum area of concave hull was calculated.

Step-5: Finally, the corner vertices $V(X_i, Y_i)$ of the concave hull CCH (Q) were obtained when the optimum harvesting area of the concave hull was determined.

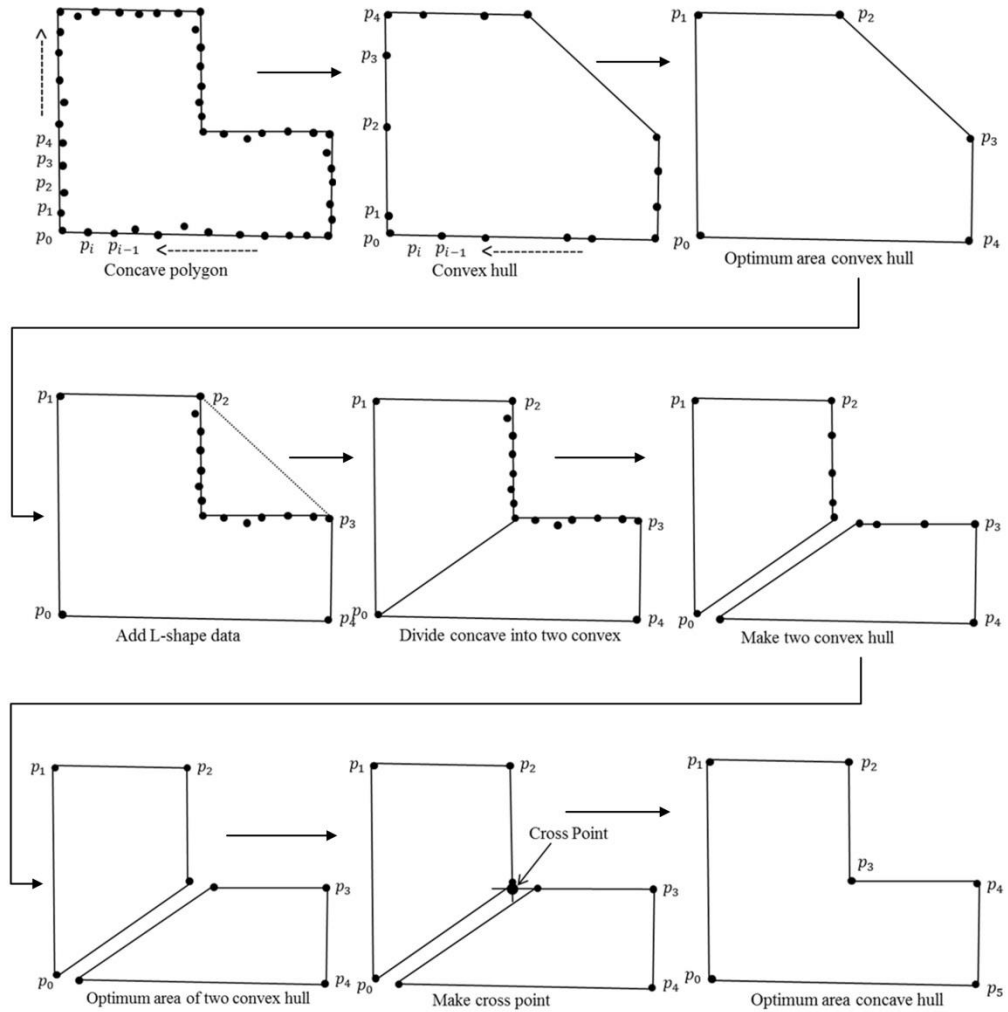


Figure 5-7. Schematic of a concave hull by the split of convex hull and cross point method

5.2.8 Working path and waypoints algorithm

The working path of a robot combine harvester was calculated from the estimated corner vertices (x_i, y_i) of an optimum harvesting area of convex or concave polygon field.

Firstly, each edge was calculated by using the Eq. (5.11) which is the modified form of the general line equation $Ax_i + By_i + C = 0$, as described in figure 5-8. By using these edges, the operator will decide the working direction of the robot combine harvester. The operator can choice any direction but in general longest direction is

better than shortest one due to consider the no. of turning. In figure 5-8, the longest edge is selected as a working direction of the robot combine harvester.

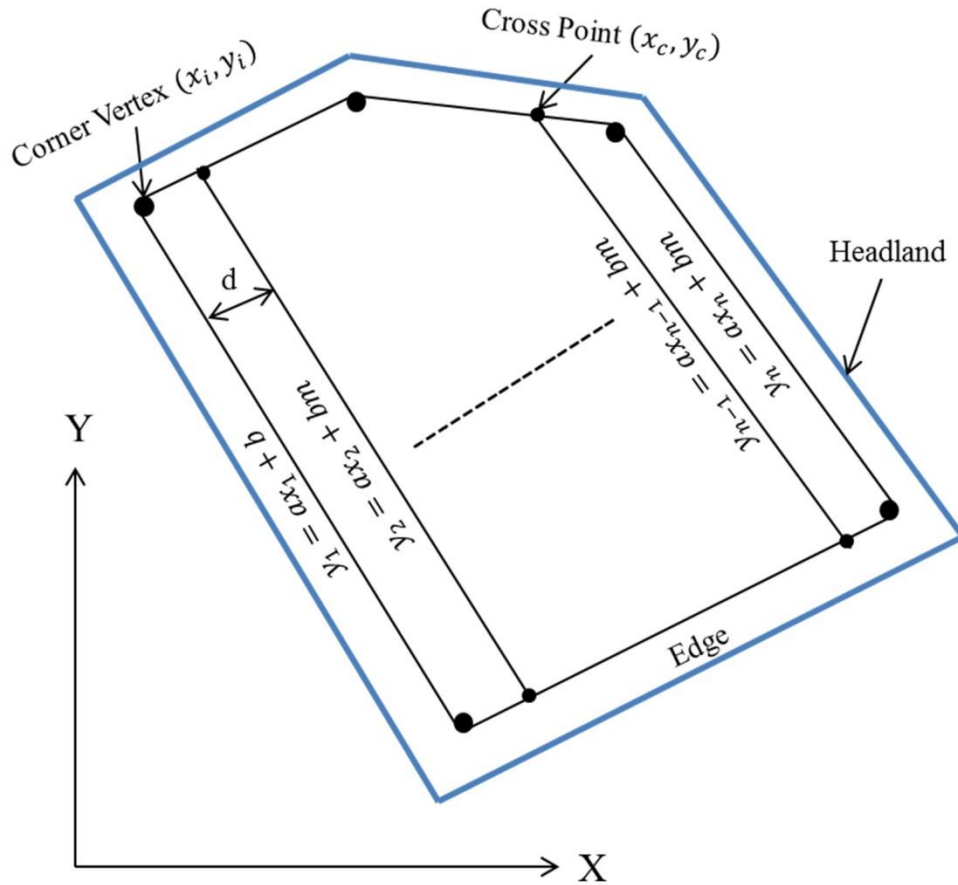


Figure 5-8. Schematic representation of the estimated path for the robot combine harvester

$$y_i = ax_i + b \quad (5.11)$$

Where,

$$a = \frac{y_i - y_{i+1}}{x_i - x_{i+1}}, \text{ and } b = y_i - \frac{y_i - y_{i+1}}{x_i - x_{i+1}} x_i$$

Secondly, based on the header length d and the turning direction, the next working path was estimated by using the Eq. (5.12).

$$y_i = ax_i + bm \quad (5.12)$$

$$\text{Where } bm = \begin{cases} b + d \sin \left[\tan^{-1} \left(-\frac{1}{a} \right) \right] - d \cos \left[\tan^{-1} \left(-\frac{1}{a} \right) \right] & (\text{for right turn}) \\ b - d \sin \left[\tan^{-1} \left(-\frac{1}{a} \right) \right] + d \cos \left[\tan^{-1} \left(-\frac{1}{a} \right) \right] & (\text{for left turn}) \end{cases}$$

Thirdly, the cross point (x_c, y_c) was calculated by using the Eq. (5.13) from the above two lines Eqs. (5.11) and (5.12).

$$(x_c, y_c) = \left(\frac{b_i - bm}{a_i - a_{i+1}}, a_i x_c + b_i \right) \quad (5.13)$$

Finally, the way point (x', y') for every path was calculated by using the following Eq. (5.14) where D indicates the distance between the start and end cross points (x_c, y_c) .

$$(x', y') = \left(x_i + \frac{x_{i+1} - x_i}{D}, y_i + \frac{y_{i+1} - y_i}{D} \right) \quad (5.14)$$

5.3 Results and Discussion

5.3.1 Estimated Header end position

During the field experiment of wheat harvesting in the field site of Hokkaido University, Japan, the RTK-GPS position and IMU measurements were taken. The red color points in figure 5-9 show the exact position of RTK-GPS antenna when the wheat field periphery nearby headland is harvested in manual operation by the robot combine harvester. Afterward, the header's end position $P(X_H, Y_H)$ was determined by using the Eq. (5.1) from the measured RTK-GPS position points $P(X_i, Y_i)$ and IMU heading angle φ , depicted in figure 5-9.

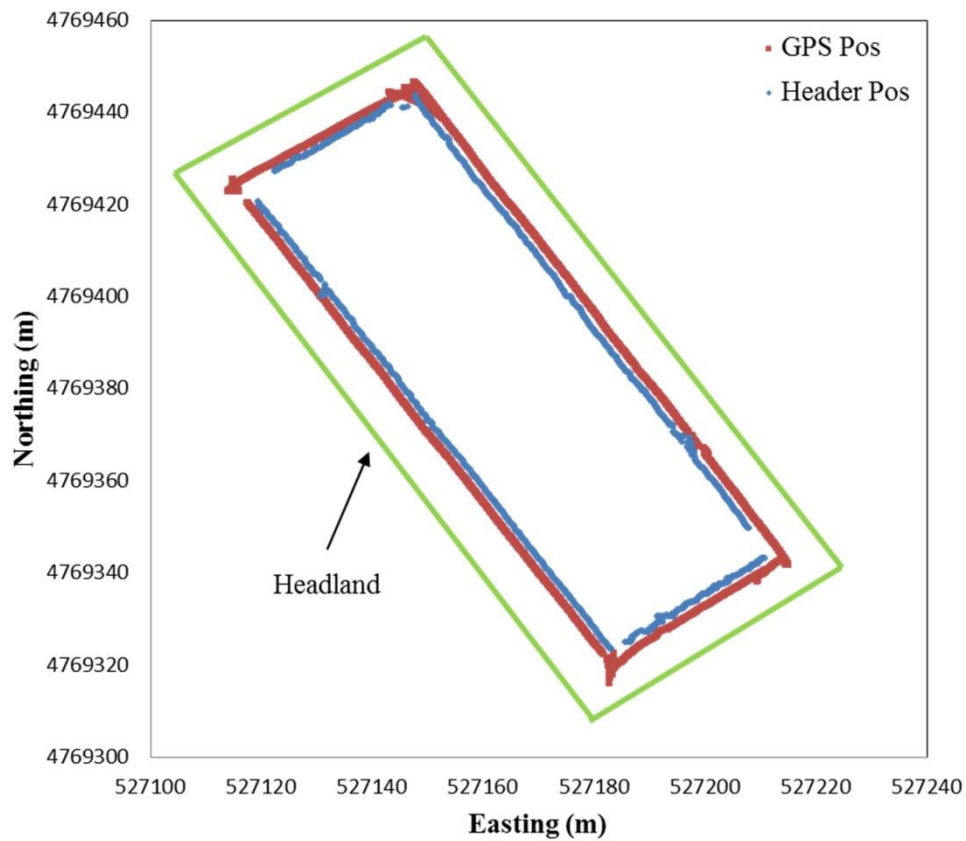


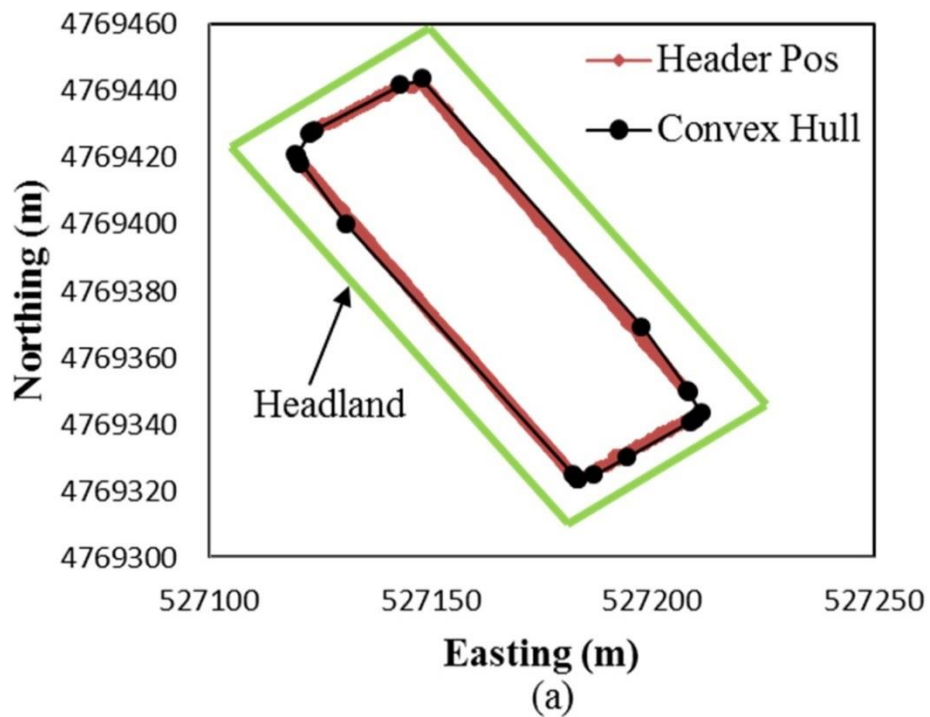
Figure 5-9. Estimated Header end position from the measured RTK-GPS position $P(X_i, Y_i)$ and heading angle φ of the robot combine harvester

The values a and b can be changed based on the size of header mounted on the robot combine harvester. The distance a and b taken in the Eq. (5.1) were 2.5 m and 1.6 m, respectively. This estimated header end position $P(X_H, Y_H)$ indicates the actual perimeter or outline of wheat in the field, which have to be harvested by the robot combine harvester.

5.3.2 Estimated Convex and Concave Hull

Figure 5-10 (a) and (b) shows the vertices of the convex hull CH (Q) that was estimated from the header's end position $P(X_H, Y_H)$ of the convex polygon field by using the incremental convex hull method. For concave polygon field, the vertices of concave hull CCH (Q) are estimated by using the split of convex hull and cross point

method which is shown in figure 5-10 (c). The results showed that the header's end position indicates the finite set of points for both convex and concave polygons field whilst the convex and concave hull gives a small set of points of that polygon field as given in figure 5-10. The result also described that the convex and concave hull method reduces the point cloud of crop perimeter, and determines the vertices of the convex hull that belongs the crop perimeter position on the boundary or inside of the convex hull that belongs the crop perimeter position on the boundary or inside of the convex and concave polygon field.



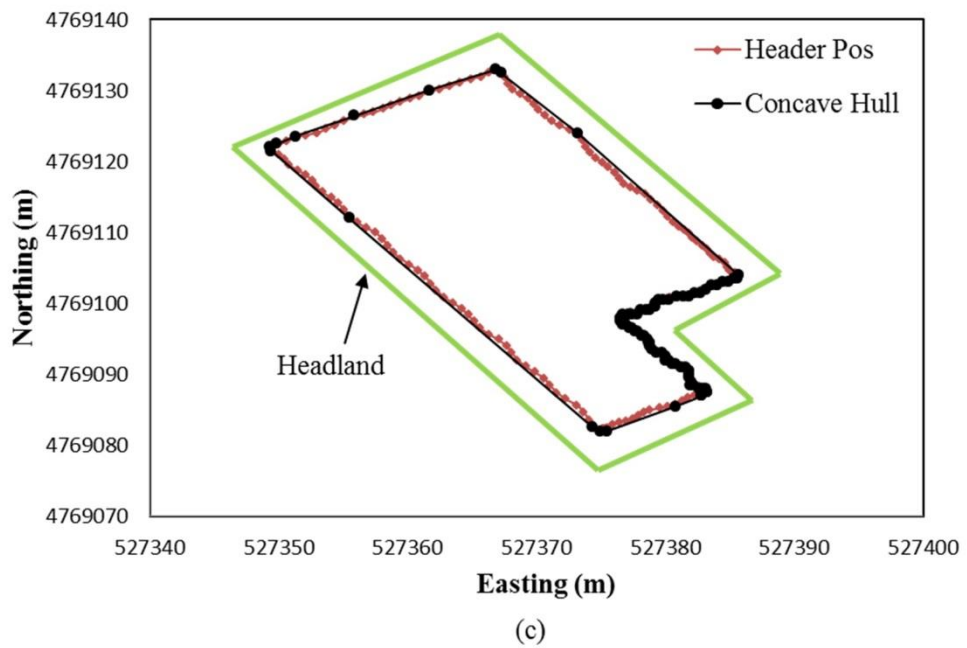
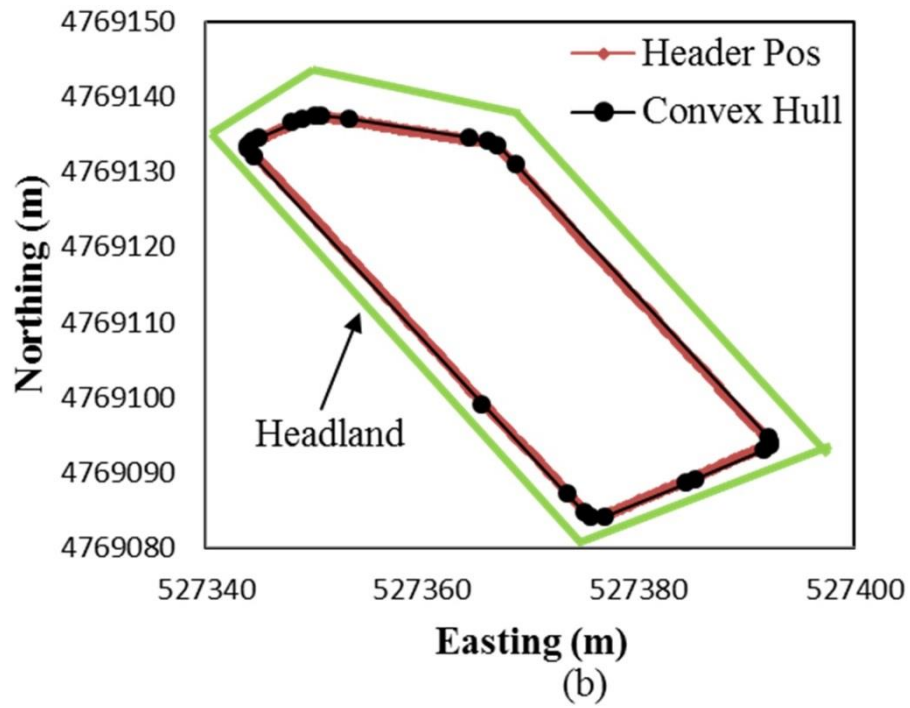
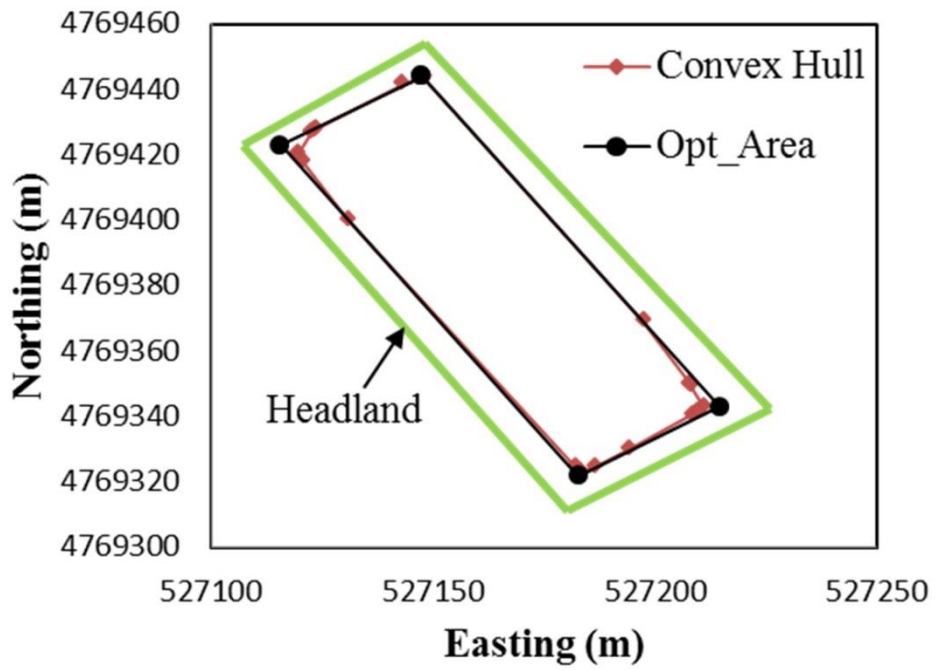


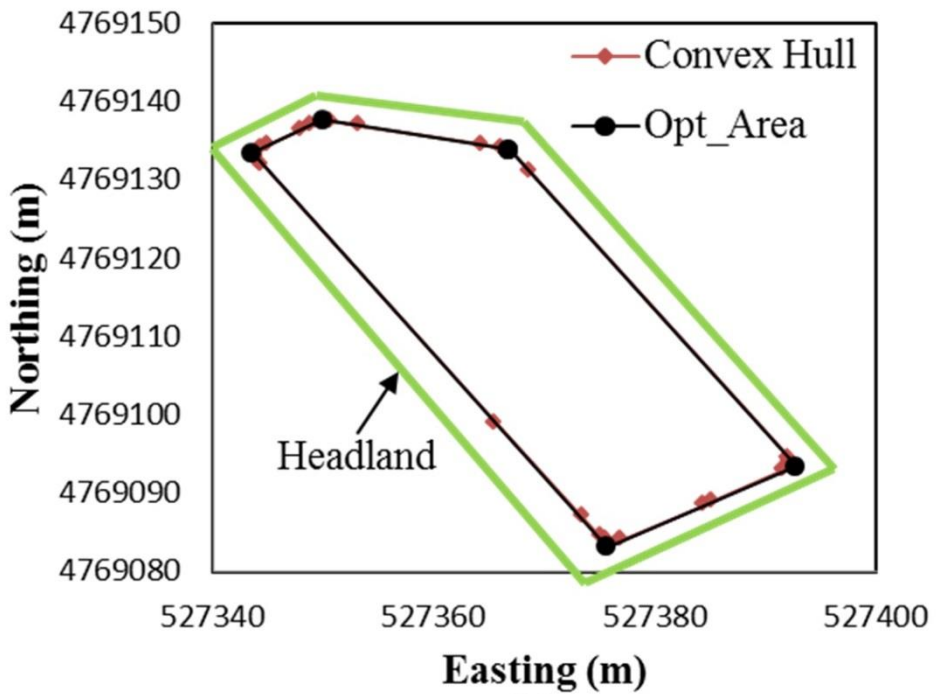
Figure 5-10. Estimated vertices of convex and concave hull from the crop perimeter of convex and concave polygon field

5.3.3 Estimated the optimum harvesting area of polygon field

The optimum harvesting area of the convex polygon field was determined from the convex hull of a convex polygon field. When the operator judges that the shape of the crop periphery is a rectangular polygon, the rotating caliper method was used to create an optimum harvesting area of rectangle field. Figure 5-11 (a) shows the corner vertices $V(X_i, Y_i)$ of an optimum harvesting area of rectangular polygon field by the rotating caliper method. When the shape of the crop periphery is an arbitrary polygon, the optimum N-Polygonal algorithm was used to calculate the corner vertices $V(X_i, Y_i)$ of an optimum harvesting area of convex polygon field, by using the Eq. (5.10) with the selected n sides of that polygon, which is given in figure 5-11 (b). In similarly way, the corner vertices $V(X_i, Y_i)$ of the concave polygon field was obtained by using the split of convex hull and cross point method as shown in figure 5-11 (c). The results indicated that the optimum harvesting area of convex and concave polygon field considers the curved or meandering parts of the convex and concave polygon field. As a consequence, the robot combine harvester will completely harvest the wheat or paddy crop without leaving any mowing residual in the field.



(a)



(b)

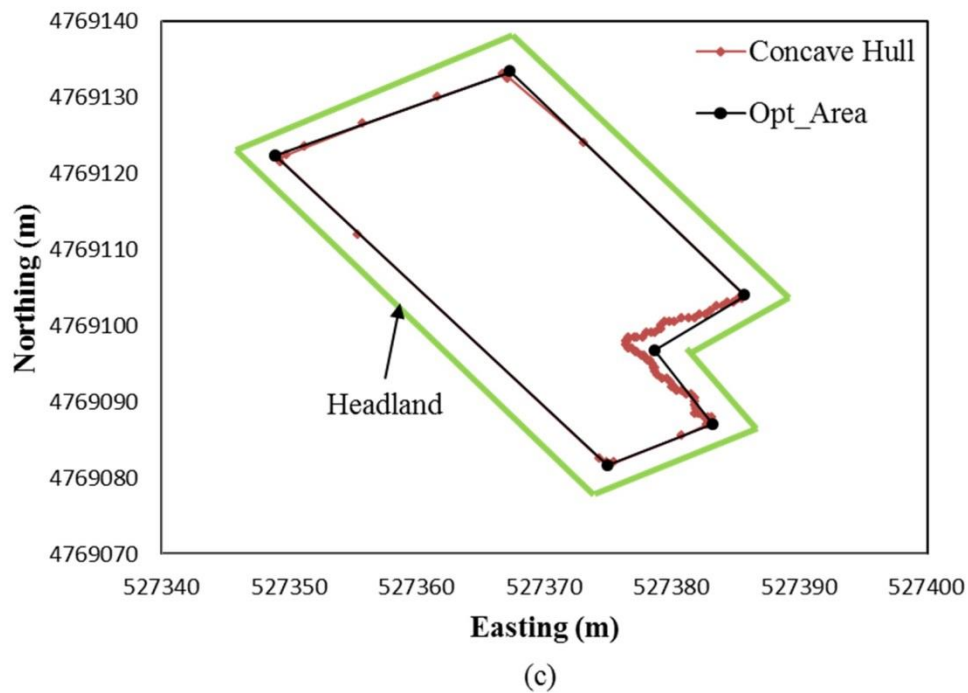


Figure 5-11. Estimated optimum harvesting area and corner vertices of convex and concave polygon field

5.3.4 Comparison of Optimum Harvesting Area

The optimum harvesting area of a rectangular polygon field during the wheat experiment was also calculated by using the optimum N-Polygon algorithm, which can be compared with the optimum harvesting area from the rotating caliper method as shown in figure 5-12. The estimated optimum harvesting area (Green line) of rectangular polygon from the optimum N-polygon algorithm was 4586.79 m^2 , while the optimum harvesting area (Red line) from the rotating caliper method was 4631.63 m^2 . During harvesting of wheat, the area size of the wheat field periphery (Blue line) from the conventional AB point method was also calculated as 4333.97 m^2 , which is smaller than the optimum harvesting area of the rectangular polygon field as shown in figure 5-12. This area size of rectangular field will be sometimes smaller or larger

than the optimum harvesting area because the corner points are measured by an operator's observation. If the operator is an expert and can take the corner point perfectly, then the robot combine harvester can harvest the wheat of the whole field. Otherwise, some mowing residual will remain in the field.

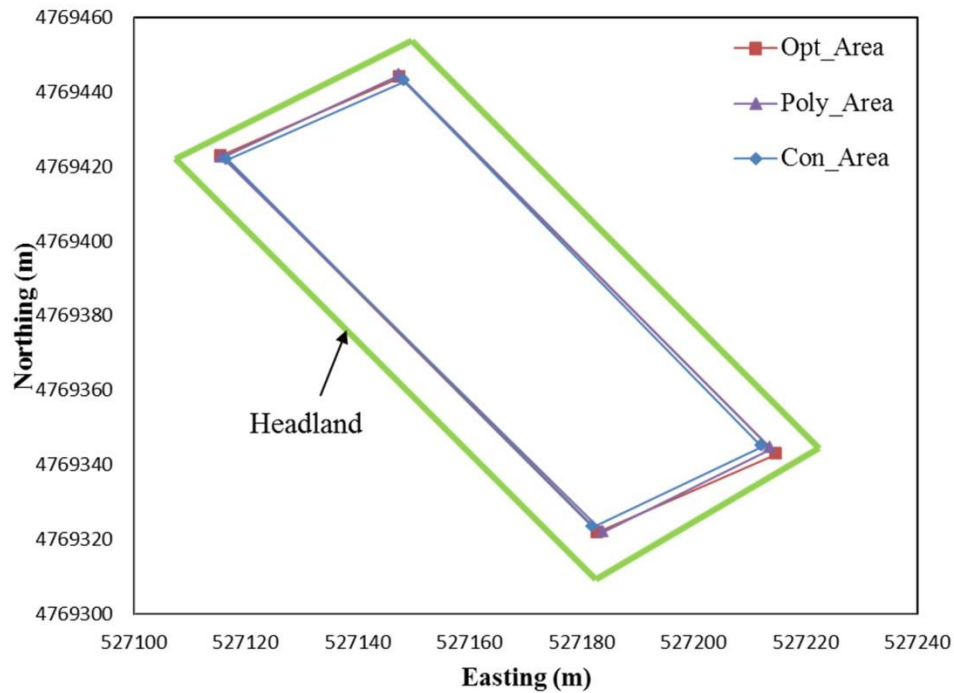


Figure 5-12. Comparison of the optimum and conventional harvesting area of convex polygon field

5.3.5 Estimated working path of the convex and concave polygon field

Figure 5-13 shows the simulated working path of the robot combine harvester on the basis of optimum harvesting area of convex and concave polygon field. This working path was generated from the estimated corner vertices $V(X_i, Y_i)$ of the optimum harvesting area of convex and concave polygon by using Eqs. (5.11) and (5.12), when the header length was considered to 2.5 m, which indicates the working width of the robot combine harvester. Afterward, during the experiment in the

rectangular wheat field, the working path was estimated based on the corner vertices $V(X_i, Y_i)$ from the Optimum harvesting area method and AB point method as shown in figure 5-14. In both methods, the total number of working paths for the robot combine harvester was 16. In the AB point method shown in figure 5-14 (a), the total working distance was counted as 1890.12 m, whereas the total distance from the optimum area method was 1941.45 m, as given in figure 5-14 (b). The results described that unlike the optimum area method for working path, if we provide the working path to the robot combine harvester by using the conventional AB point method, the robot will leave 51.33 m of mowing residual or meandering of wheat in the field. In addition, if we take the corner points based on the conventional AB point method for estimating the working path, the system needs almost 20-25 minutes to perform calculations. This time can be increased or decreased regarding the size of crop field. But on the other hand, the working path based on the proposed optimum area method need only a few minutes.

For the experiment in concave wheat field, figure 5-15 (a) shows the working path of robot combine harvester obtained by using the conventional corner points and by using Eqs. (5.11) and (5.12), whereas the working path was computed based on the corner vertices of optimum harvesting area as given in figure 5-15 (b). The working path obtained from conventional corner points is counted as 13 in figure 5-15 (a), while 11 nos. of working path was calculated from the optimum harvesting area for the same wheat field shown in figure 5-15 (b). Since the conventional corner points were taken from the visual observation, sometimes this observation will be good and sometimes not. In addition, the area obtained from this observation points is not optimum, and little bit larger than optimum harvesting area that was obtained based on the developed optimization algorithm, for this reason, 2 nos. of working path is more

for conventional area than optimum harvesting area. This experiment indicated that the working path based on the optimum harvesting area reduces the operational processing time and increases the overall harvesting efficiency of robot combine harvester in real time.

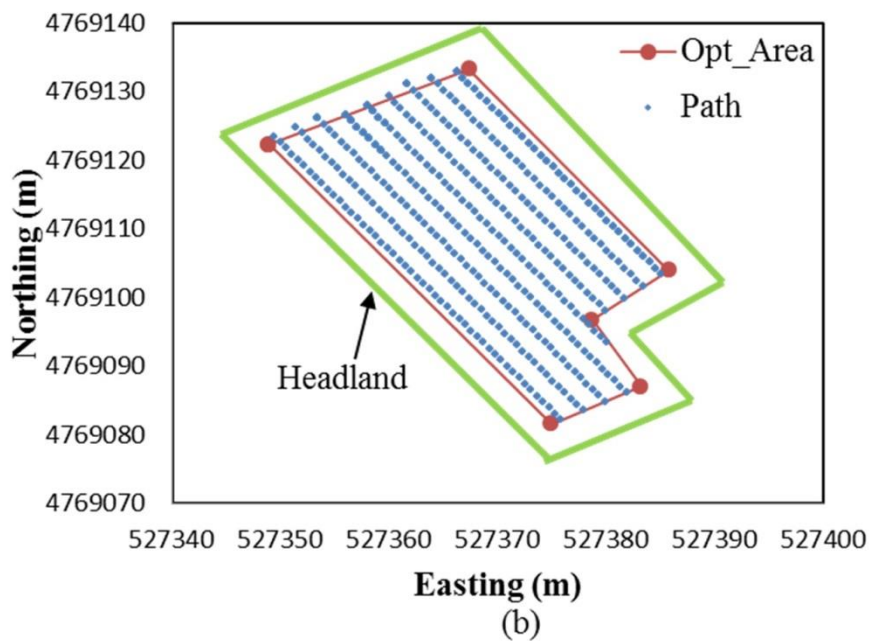
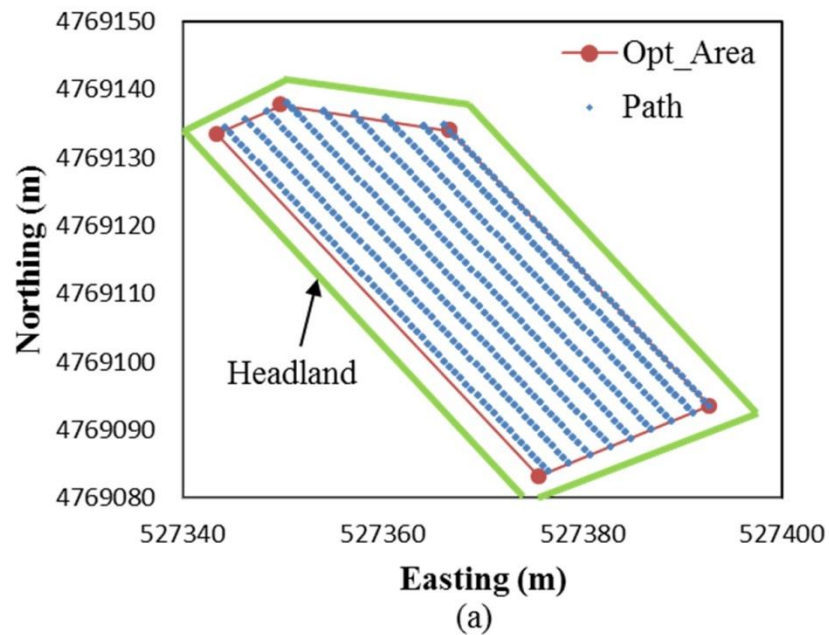


Figure 5-13. Estimated working path of the convex and concave polygon field

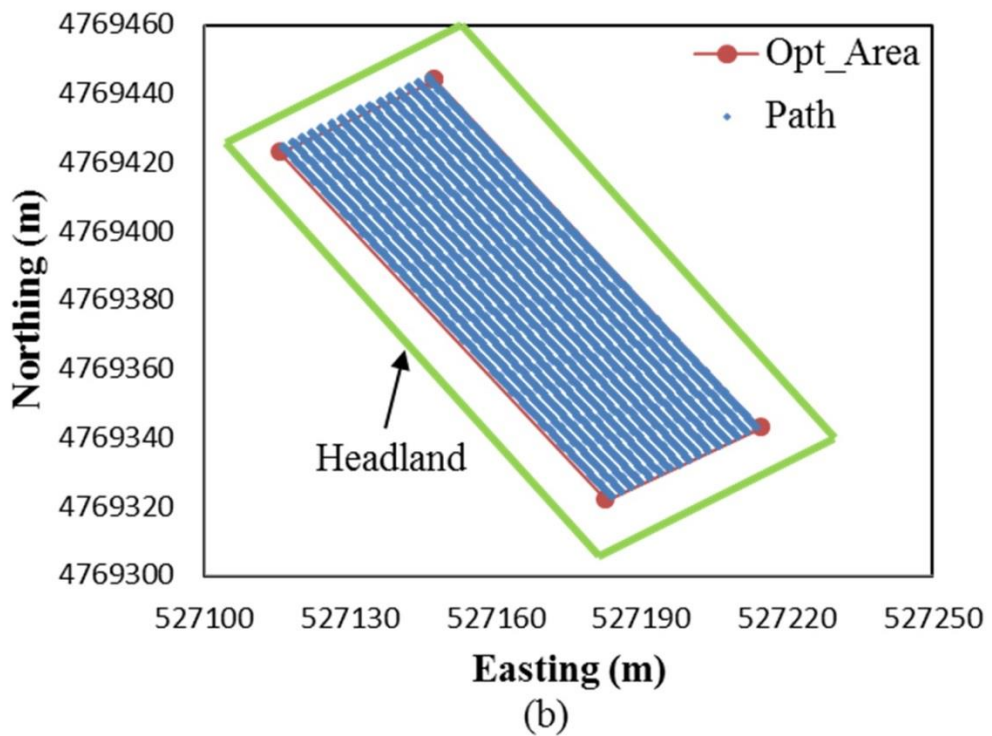
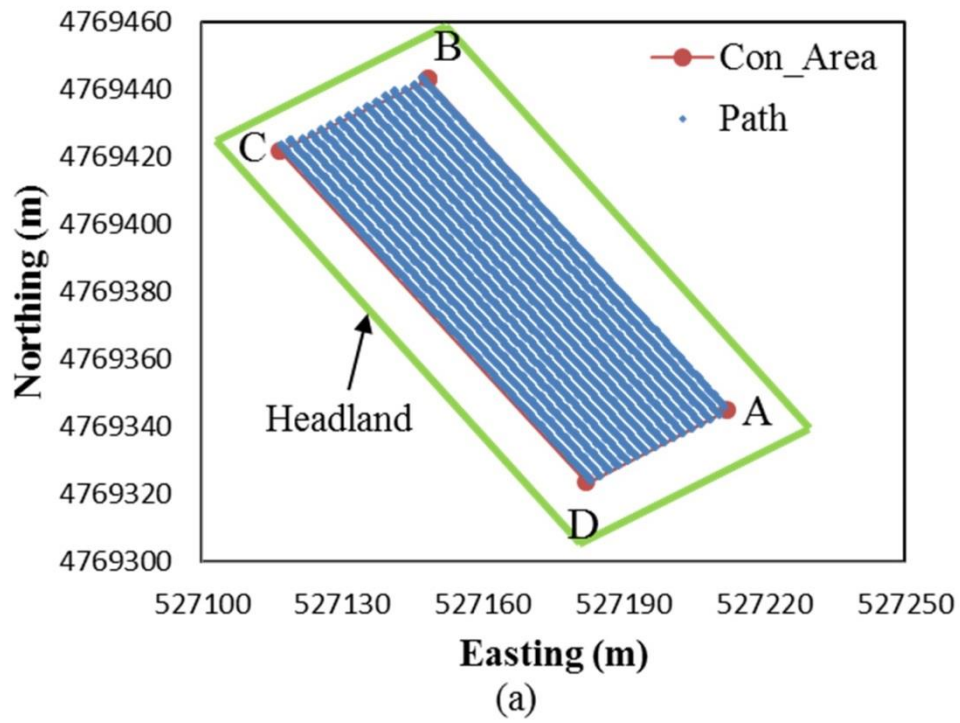


Figure 5-14. Estimated working path of the robot combine harvester during experiment in a rectangular wheat field

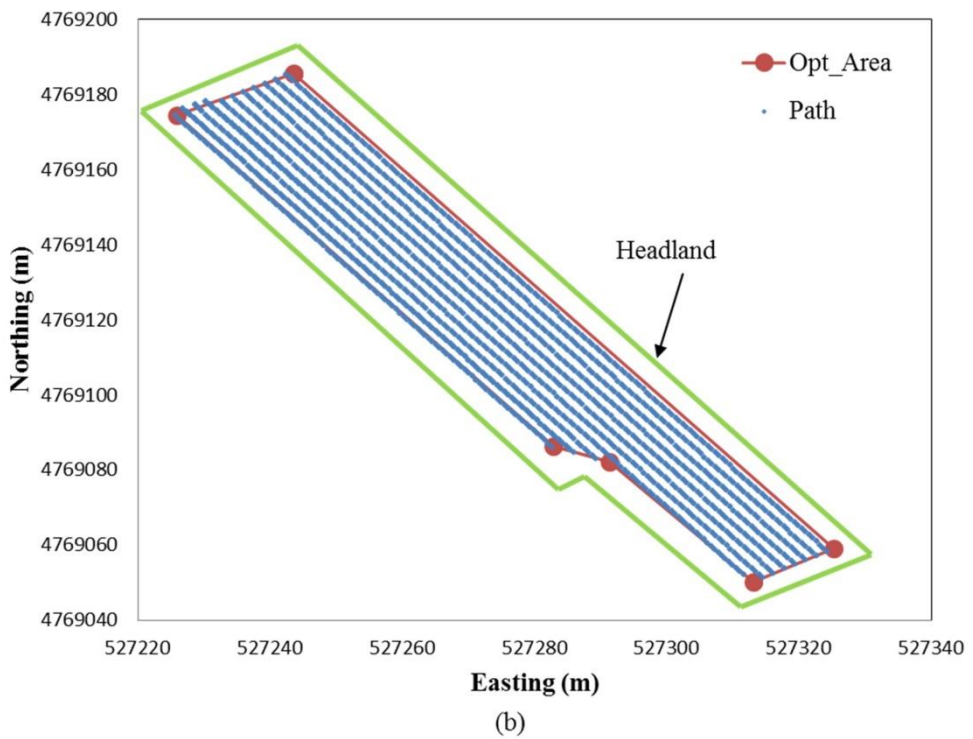
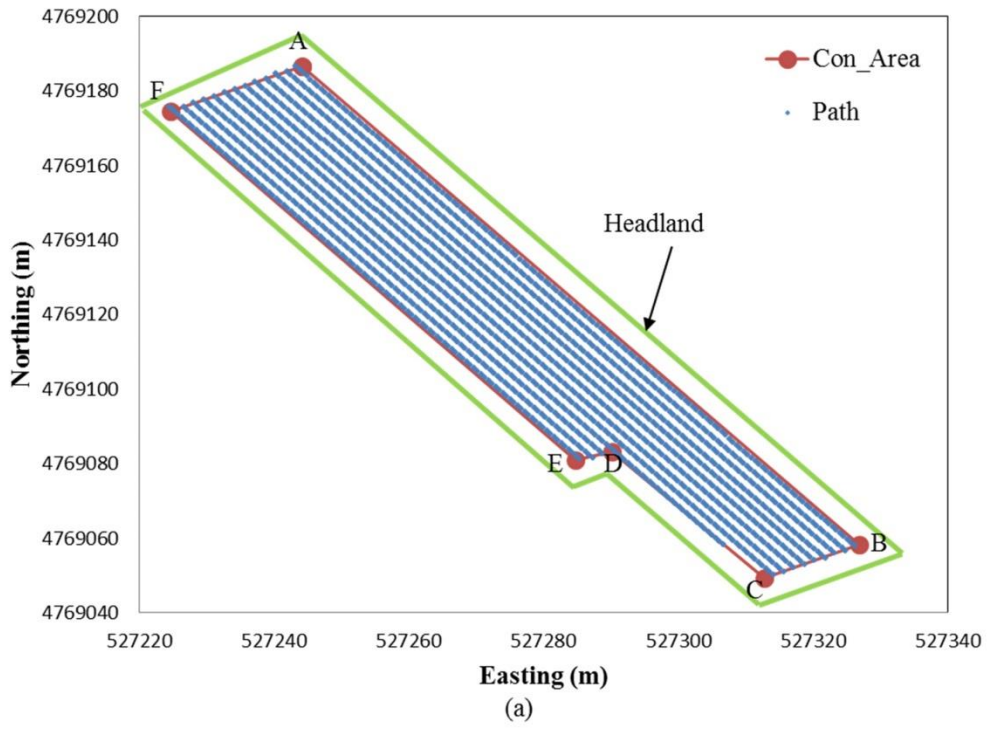


Figure 5-15. Estimated working path of the robot combine harvester during experiment in a concave wheat field

5.4 Conclusions

Automatic path planning is an important topic nowadays for robotic agricultural vehicles. This chapter described an automatic path planning algorithm for a robot combine harvester to harvest wheat or paddy which is not in row. The crop exact outline measured from the RTK-GPS position and IMU heading, which provides thousands of points, and this point clouds are reduced by using the incremental convex hull method. Using the estimated convex hull, the optimum harvesting area of a polygon is determined by the rotating caliper method, the optimum N-polygon algorithm, and by the split of convex hull and cross point method; which are better optimization method for an area than the area based on the conventional AB point method. Unlike the conventional AB point method, the developed algorithm calculates an optimum harvesting area of polygon that covers the whole part of the remaining crop and provides appropriate corner vertices. These corner vertices are used to calculate a working path for the robot combine harvester, which is better than the working path obtained from the conventional AB point method. The harvesting of a crop based on the working path from the conventional method is not good enough and highly depends on the operator's visual accuracy. This problem is completely solved by using the developed algorithm in this research. In addition, the work path estimated based on the conventional AB point method needs more times to process all information, whereas the developed algorithm requires only a few minutes. Finally, we can conclude that the developed algorithm reduces the operational processing time and completely remove the crop losses in course of the harvesting operation performed in the field by the robot combine harvester in real time.

Chapter 6 Research Summary and Conclusion

6.1 Introduction

This chapter summarizes the whole research presented throughout the thesis and draws conclusions. In section 6.2, the summary of each chapter contents are discussed. The contributions of the thesis are reviewed in Section 6.3. Finally, the future research issues for the robot combine harvester are identified in Section 6.4.

6.2 Summary of Each Chapter

In chapter 1, an overview of past and present researches for agricultural robot vehicles were presented. The concepts of agricultural robot adopted instead of manual driven agricultural vehicles were discussed. Researches on autonomous combine harvester, sensors and sensor fusion method were discussed. Mathematical motion model is important for controlling of tracked vehicles which was also presented. Existing working system for autonomous agricultural vehicles was discussed. Based on the different related research contents, the overall motivation and research objectives were presented in that chapter.

In chapter 2, a robot Combine harvester was presented in detailed, which is equipped with RTK-GPS and IMU sensors, where the detailed specifications of these sensors were given. Sensor fusion method is used to remove sensor measurements uncertainties, which was given in that chapter. For the estimated optimum harvesting area of a crop field, a convex hull and rotating caliper method were also described.

In chapter 3, the tracked combine harvester motion model based on RTK-GPS and IMU sensors was revealed. The tracked dynamic model was evaluated to obtain the state and angular rate of tracked combine harvester in non-linear conditions.

Tracked soil interaction parameter and track coefficients were presented in that chapter. Turning radius obtained from the RTK-GPS position is important parameter for turning maneuverability, which was also given. The sideslip angle from the tracked combine harvester direction and RTK-GPS heading was discussed.

In chapter 4, Extended Kalman Filter method is used to compensate the yaw rate gyro measurement bias which was presented. The tracked combine harvester dynamic model, sensor measurements and extended kalman filter were discussed to estimate the absolute heading of tracked combine harvester during turning in the field corner, when the tracked combine harvester was turn at high speed in order to cut the crop periphery. The results were analyzed for the circular and sinusoidal trajectories, which showed that the estimated heading is better than the measured ones. The experimental results for estimated heading in convex and concave polygon field were also discussed in that chapter. This estimated heading can further be used to calculate the header end position or exact outline of crops for the time of turning.

In chapter 5, an optimum harvesting area was estimated for automatic path planning of the robot combine harvester. An incremental convex hull method was presented to make a convex hull from a finite set of RTK-GPS positions. The optimum harvesting area for a rectangular field obtained by the rotating caliper method was also discussed. The developed N-Polygon algorithm is used to estimate the optimum harvesting area of convex polygon field was presented in that chapter. For concave polygon field, the estimation of optimum harvesting area is little bit difficult, but the developed split of convex hull and cross point method can solve this problem, which was also disclosed. Using the optimum harvesting area for convex

and concave polygon field, the working routes of the robot combine harvester was calculated in that chapter.

6.3 Contributions

6.3.1 Tracked Combine Harvester Motion Model

Tracked combine harvester motion model integrated with sensor measurements may help to know the controlling behavior of tracked combine harvester in non-linear conditions. Consequently, the track-soil interaction parameter and track coefficients derived from the tracked combine harvester motion model and sensor measurements may be computed in real time. The turning radius and sideslip angle are obtained on the basis of RTK-GPS and IMU sensor measurements, which gives better results than theoretically calculated.

6.3.2 Heading Estimation Method

The IMU yaw rate gyro measurement gives uncertainty like bias which is essential to compensate for estimating the absolute heading of the tracked combine harvester. This absolute heading is important for the robot combine harvester in the course of turning, which is estimated by using the extended kalman filter and tracked combine harvester dynamic model. The experimental results showed that the gyro measurement bias was compensated based on this integrated method.

6.3.3 Optimization of Harvesting Area of Convex and Concave Polygon field

Using incremental convex hull method, a convex hull can be obtained by reducing the point clouds, which is good approach for estimating the exact shape of crop periphery. Rotating caliper method is only used to determine the optimum harvester area of rectangular field, but this method is not applicable for other convex polygon field like pentagon, hexagon etc. In this circumstance, N-Polygon algorithm

was developed to estimate the optimum harvesting area of convex polygon field, which is another good approach for this research. But this method has also limitation, and it can not work for concave polygon field. For this case, the developed split of convex hull and cross point method is suitable for estimating the optimum harvesting area of concave polygon field.

6.3.4 Path Planning for Convex and Concave Polygon field

Path planning for any agricultural robot vehicles is very important so that it can cover the whole field. Especially, for the robot combine harvester, the harvesting of crop field should be optimized, otherwise the crop loss will be occurred, and the overall field efficiency will be reduced. As for path planning needs field corner vertices, the path planning method from the corner vertices based on the optimum harvesting area is a good approach, which can be applicable for any shape of convex and concave polygon field.

6.4 Future Work

One important thing is how to communicate the robot combine harvester and the unloader robot tractor during harvesting of wheat or paddy. When the robot combine harvester grain tank is filled up, it is unloaded by manually bringing the robot combine harvester near to the unloader tractor. But if a suitable communication system or algorithm is developed between the robot combine harvester and unloader robot tractor so that a robot combine harvester can call the unloader robot tractor and unload its grain from the grain tank automatically to the unloader robot tractor, and starts again harvesting without any operator intervention.

References

- Acar E. U., Choset H., Rizzi A. A., Atkar P.N. and Hull D. (2002). Morse decompositions for coverage tasks. *The International Journal of Robotics Research*. 21(4): 331-344.
- Adla R., Yousef B. and Al-Holou N. (2013). Multi sensor Data Fusion, Methods and Problems. *Proceedings of the International conference on Parallel and Distributed Processing Techniques and Applications, Las Vegas Nevada, USA, July 22-23, Volume-II*.
- Ahamed T., Takigawa T., Koike M., Honma T., Yoda A., Hasegawa H., Junyusen P. and Zhang Q. (2004). Characterization of laser range finder for in-field navigation of autonomous tractor. In *Conference Proceedings of Automation Technology for Off-Road equipment, ASABE, October 7-8, Kyoto, Japan*.
- Bekker M. G. (1962). *Theory of Land Locomotion*. The University of Michigan Press.
- Bekker M. G. (1969). *Introduction to Terrain–Vehicle Systems*. The University of Michigan Press.
- Belforte G., Deboli R., Gay P., Piccarolo P. and Ricauda Aimonino D. (2006). Robot Design and Testing for Greenhouse Applications. *Biosystems Engineering*, 95(3): 309-321.
- Bell T. (1999). Automatic tractor guidance using carrier-phase differential GPS. *Computers and electronics in agriculture: Special Issue Navigating Agricultural Field Machinery*.

- Bell T. (2000). Automatic tractor guidance using carrier-phase differential GPS. *Computer and electronics in agriculture*, 25(1-2): 53-66.
- Benson E.R., Reid J.F. and Zhang Q. (2001). Machine vision based steering system for agricultural combines. ASAE Annual Meeting, 011159.
- Benson E.R., Reid J.F. and Zhang Q. (2003). Machine Vision-based Guidance System for Agricultural Grain Harvesters using Cut-edge Detection. *Biosystems Engineering*, 86 (4):389–398.
- Bochtis D., Griepentrog H.W., Vougioukas S., Busto P., Berruto R. and Zhou K. (2015). Route planning for orchard operations. *Computers and Electronics in Agriculture*, 113: 51-60.
- Chateau T., Debain C., Collange F., Trassoudaine L. and Alizon J. (2000). Automatic guidance of agricultural vehicles using a laser sensor. *Computers and Electronics in Agriculture*, 28, 243–257.
- Cho S.I., Ki N.H. (1999). Autonomous speed sprayer guidance using machine vision and fuzzy logic. *Transactions of the ASAE*, 42(4): 1137-1143.
- Choi J. (2014). Development of Guidance System Using Local Sensors for Agricultural Vehicles. PhD theses, Graduate School of Agriculture, Hokkaido University, Sapporo, Japan. Source: <http://hdl.handle.net/2115/56098>
- Coen T., Vanrenterghem A., Saeys W. and De Baerdemaeker J. (2008). Autopilot for a combine harvester. *Computers and Electronics in Agriculture*, 63: 57–64.
- Cordesses L., Cariou C. and Berducat M. (2000). Combine Harvester Control Using Real Time Kinematic GPS. *Precision Agriculture*, 2: 147-161.

- David J. Purdy and Patrick J. H. Wormell (2003). Handling of High Speed Tracked Vehicles. *Journal of Battle Field Techonology*, 6(2):17-22.
- de Berg M., van Kreveld M., Overmars Mark and Schwarzkopf O. (2000). *Computational Geometry: Algorithms and Applications*, Springer, pp. 2–8.
- Driscoll T. M. (2011). Complete coverage path planning in an agricultural environment. *Graduate Theses and Dissertations*, Iowa State University, USA.
- English A., Ball D., Ross P., Upcorft B., Wyeth G. and Corke P. (2013). Low Cost Localisation for Agricultural Robotics. *Proceedings of Australasian Conference on Robotics and Automation*, December 2-4, University of New South Wales, Sydney, Australia.
- Fehr B.W. and Gerrish, J.B. (1995). Vision-guided row crop follower. *Appl. Eng. Agric.* 11 (4): 613–620.
- Godfried T. (1983). Solving geometric problems with the rotating calipers. In *Proceedings of IEEE MELECON*, 1-8.
- Hague T., Marchant J.A. and N.D. Tillett (2000). Ground based sensing systems for autonomous agricultural vehicles. *Computers and Electronics in Agriculture*, 25(1-2):11-28.
- Hameed A., la Cour-Harbo A. and Osen O. L. (2016). Side-to side 3D coverage path planning approach for agricultural robots to minimize skip/overlap areas between swaths. *Robotics and Autonomous System*, 76: 36-45.

- Hofstee J. W., Spa L. E. E. M. 'tjens and Ijken H. (2009). Optimal path planning for field operations, Precision Agriculture, 511-519. Source: <https://www.researchgate.net/publication/41182748>
- Huh K. and Hong D. (2001). Track tension estimation in tracked vehicle under various maneuvering tasks. Journal of Dynamic System, Measurement, and Control, 123: 179-184.
- Iida M. and Yamada Y. (2006). Rice Harvest Using Driverless Combine Harvester Equipped with GPS and Gyro. Journal of JSAM, 68(6): 138-143.
- Inoue K., Otsuka H., Sugimoto H. and Murakami N. (1999). Sensor fusion of GPS and gyroscope by using Kalman Filter for automatic navigation (Part 1). Journal of the Society of Agricultural Machinery, 61(4):103-114.
- Iqbal U., Tashfeen B. K., Aime F.O. and Noureldin A. (2009). Experimental Results on an Integrated GPS and Multisensor System for Land Vehicle Positioning. International Journal of Navigation and Observation, p:18.
- Ishii K., Terao H. and Noguchi N. (1994). Studies on Self-learning Autonomous Vehicles (Part- 1). Journal of the Society of Agricultural Machinery, 56(4): 53-60, (Japanese).
- Ishii K., Terao H. and Noguchi N. (1995). Studies on Self-learning Autonomous Vehicles (Part- 2). Journal of the Society of Agricultural Machinery, 57(6): 61-67, (Japanese).
- Ishii K., Terao H. and Noguchi N. (1998). Studies on Self-learning Autonomous Vehicles (Part- 3). Journal of the Society of Agricultural Machinery, 60(1): 51-58, (Japanese).

- Ishii K., Terao H. and Noguchi N. (1998). Studies on Self-learning Autonomous Vehicles (Part- 4). *Journal of the Society of Agricultural Machinery*, 60(2): 53-58, (Japanese).
- Janarthanan B., Padmanabhan C. and Sujatha C. (2011). Lateral dynamics of single unit skid-steered tracked vehicle. *International Journal of Automotive Technology*, 12(6): 865-875.
- Jin J. and Tang L. (2010). Optimal coverage path planning for arable farming on 2D surfaces. *Transactions of the ASABE*. 53(1): 283-295.
- Jorge A. Heraud and Arthur F. Lange (2009). *Agricultural Automatic Vehicles Guidance from Horses to GPS: Where we are going*. Agricultural Equipment Technology Conference, Louisville, Kentucky, USA.
- Julian S. H., Francisco R., Ramon G., Jose L. G. and Manuel B. (2010). A Mechatronic Description of an Autonomous Mobile Robot for Agricultural Tasks in Greenhouses, *Mobile Robots Navigation*, Alejandra Barrera (Ed.), ISBN: 978-953-307-076-6, InTech, Available from: <http://www.intechopen.com/books/mobile-robots-navigation/a-mechatronic-description-of-an-autonomousmobile-robot-for-agricultural-tasks-in-greenhouses>.
- Kallay M. (1984). The complexity of incremental convex hull algorithms in R^d . *Information Processing Letters*. 19(4): 197.
- Kise M., Noguchi N., Ishii K. and Terao H. (2001). Field mobile robot navigated by RTK-GPS and FOG (Part-2). *Journal of JSAM*, 63(5): 80-85.
- Kise M., Noguchi N., Ishii K. and Terao H. (2003). Field mobile robot navigated by RTK-GPS and FOG (Part-3). *Journal of JSAM*, 64(2): 102-110.

- Kitano M. and Jyozaki H. (1976). A theoretical analysis of steerability of tracked vehicles. *Journal of Terramechanics*, Pergamon Press Printed in Great Britain, 13(4): 241-258.
- Kitano M. and Kuma M. (1977). An analysis of horizontal plane motion of tracked vehicles. *Journal of Terramechanics*, Pergamon Press Printed in Great Britain, 14(4): 221-225.
- Kurita H., Iida M., Cho W. and Suguri M. (2017). Rice Autonomous Harvesting: Operation Framework. *Journal of Field Robotics*, 34(6): 1084-1099.
- Le A. T. (1999). *Modelling and Control of Tracked Vehicles*. Doctoral thesis. Department of Mechanical and Mechatronic Engineering, The University of Sydney.
- Le A. T., Rye David. C. and Durnat-Whyte Hugh. F. (1997). Estimation of track-soil interactions for autonomous tracked vehicles. *Proceedings of the IEEE International Conference on Robotics and Automation*, Albuquerque, New Mexico, April, pp: 1388-1393.
- Linsong G., Yong H., Qin Z. and Shufeng H. (2002). Real-Time Tractor Position Estimation System Using a Kalman Filter. *Transactions of the CSAE*, 18(5): 96-101.
- Liu Y. (2017). *Autonomous Navigation for an Agricultural Unmanned Airboat in Paddy Field*. PhD theses, Graduate School of Agriculture, Hokkaido University, Sapporo, Japan. Source: <http://hdl.handle.net/2115/66101>
- Mandow A., Go`mez de Gabriel J. M., Mart´ınez J. L., Munoz V. F., Ollero A. and Garcı´a-Cerezo A. (1996). The autonomous mobile robot AURORA for greenhouse operation. *IEEE Robotics & Automation Magazine*, 18–28.

- Miu P. (2016). *Combine harvesters: Theory, Modelling, and Design*. CRC Press, Taylor & Francis Group, 6000 Broken Sound Parkway NW, Suite 300, Boca Raton, FL 33487-2742.
- Mizushima A., Ishii K., Noguchi N., Matsuo Y. and Lu R. (2011). Development of a low-cost attitude sensor for agricultural vehicles. *Computer and Electronics in Agriculture*, 76: 198-204.
- Murphy R. R. (2000). *Introduction to AI Robotics*. A Bradford Book, The MIT Press.
- Nagasaka Y., Saito H., Tamaki K., Seki M., Kobayashi K. and Taniwaki K. (2009). An autonomous rice transplanter guided by global positioning system and inertial measurement unit. *Journal of Field Robotics*, 26(6-7): 537-548.
- Nagasaka Y., Tamaki K., Nishiwaki K., Saito M., Kikuchi Y. and Motobayashi K. (2013). A global positioning system guided automated rice transplanter. *Proceedings of 4th IFAC Conference on Modelling and Control in Agriculture, Horticulture and Post Harvest Industry*, 41-46.
- Nagasaka Y., Taniwaki K., Otani R., Shigeta K. and Sasaki Y. (1999). The Development of Autonomous Rice Transplanter.(Part 1): The Location of the Rice Transplanter by a Real-Time Kinematic GPS. *Journal of the Society of Agricultural Machinery*, 61(6): 179-186.
- Nagasaka Y., Umeda N., Kanetai Y., Taniwaki K. and Sasaki Y. (2004). Autonomous guidance for rice transplanting using global positioning and gyroscopes, *Computers and Electronics in Agriculture*, 43: 223-224.

- Noguchi N., Ishii K. and Terao H. (1997). Development of an agricultural mobile robot using a geomagnetic direction sensor and image sensors. *J. agric. Engng Res.* 67: 1-15.
- Noguchi N., Reid J. F., Benson E., Will J. and Stombaugh T. (1998). Vehicle automation system based on multi-sensor integration. ASAE Paper 983111. St. Joseph, MI.
- Oksanen T. and Visala A. (2007). Path planning algorithms for agricultural machines. *Agricultural Engineering International: the CIGR Ejournal*, Manuscript ATOE 07 009, IX.
- Oksanen T., Linja M. and Visala A. (2005). Low-cost positioning system for agricultural vehicles. Proceedings 2005 IEEE International Symposium on Computational Intelligence in Robotics and Automation, Espoo, Finland, June 27-30.
- Parkinson B. W. and Spilker J. J. (1996). *Global Positioning System: Theory and Applications*. Washington, D.C.: American Institute of Aeronautics and astronautics.
- Patrick J. H. Wormell and David J. Purdy, (2004). Handling of Tracked Vehicles at Low Speed. *Journal of Battle Field Techonology*, 7(1):21-26.
- Randle J. S. and Horton M. A. (1997). Low cost navigation using micro-machined technology. In Proceedings o IEEE Conference on Intelligent Transportation Systems ITSC, Boston, MA, pp:1064-1067.

- Reid J. F., Zhang Q., Noguchi N. and M. Dickson (2000). Agricultural automatic guidance research in North America. *Computers and Electronics in Agriculture*, 25(1-2):155-167.
- Reid J.F. (2004). Mobile Intelligent Equipment for Off-road Environments. In *Proceedings of ASAE International Conference on Automation Technology for Off-road Equipment*, 1-9.
- Reid J.F. and Searcy S.W. (1987). Vision-based guidance of an agricultural tractor. *IEEE Control Systems* 7 (12): 39–43.
- Rodrigo S. Z. (2012). Computational tools for improving route planning in agricultural field operations. *Theses and Dissertations-Biosystems and Agricultural Engineering*, 11.
- Rovira-Más F., Han S., Wei J. and Reid J. F. (2007). Autonomous Guidance of a Corn Harvester using Stereo Vision. *Agricultural Engineering International: the CIGR Ejournal*. Manuscript ATOE 07 013. Vol. IX.
- Saito M., Tamaki K., Nishiwaki K. and Nagasaka Y. (2012). Development of an Autonomous Rice Combine Harvester Using CAN Bus Network. *Journal of the Society of Agricultural Machinery*, 74(4): 312-317.
- Saito M., Tamaki K., Nishiwaki K., Nagasaka Y. and Motobayashi K. (2013). Development of Robot Combine Harvester for Beans Using CAN Bus Network. 4th IFAC Conference on Modelling and Control in Agriculture, Horticulture and Post-Harvest Industry, Espoo, Finland, August 27-30.
- Sandini G., Buemi F., Massa M. and Zucchini M. (1990). Visually guided operations in greenhouse. *Proceedings of the IEEE International Workshop on intelligent Robots and Systems IROS '90*, pp 279–285.

- Sedgewick R. and Wayne K. (2011). Algorithms. Text book. Printed in the United States of America. ISBN-13:978-321-57351-3.
- Shamos M.I. (1978). Computational geometry, Ph.D. thesis, Yale University.
- Shiller Z., Serate W. and Hua M. (1993). Trajectory Planning of Tracked Vehicles. Proceedings IEEE International Conference on Robotics and Automation, May 2-6.
- Statistics Bureau (2016). Statistical Handbook of Japan. Ministry of Internal Affairs and Communications Japan.
(<http://www.stat.go.jp/english/data/handbook/index.htm>)
- Stoll A. (2003). Automatic operation planning for GPS-guided machinery. In: Proceedings of the 4th European Conference on Precision Agriculture, 657-664.
- Stombaugh T., Benson E. and Hummel J.W. (1998). Automatic guidance of agricultural vehicles at high field speed. ASAE Paper, 983110, St. Joseph, MI.
- Stombaugh T., Benson E. and Hummel J.W. (1998). Automatic guidance of agricultural vehicles at high field speeds. ASAE Paper 983110. St. Joseph, MI.
- Subramanian V., Burks T. F. and Dixon W. E. (2009). Sensor fusion using fuzzy logic enhanced kalman filter for autonomous vehicle guidance in citrus groves. Transactions of the ASABE, Vol. 52(5): 1411-1422.
- Suguri M., Karita K. and Nishiike Y. (2004). RTK-GPS based autonomous crawler wagon control, Proceedings of the Automation Technology for Off-road Equipment (ATOE 2004), 360-368.

- Taix M., Soueres P., Frayssinet H. and Cordesses L. (2006). Path planning for complete coverage with agricultural machines. *Field and service robotics*, 24: 549-558.
- Takai R., Barawid O. Jr., Ishii K. and Noguchi N. (2010). Development of Crawler-Type Robot Tractor based on GPS and IMU. Preprint of the IFAC International Conference on AGRICONTROL 2010 (CD-R), A3-5.
- Takai R., Yang L. and Noguchi N. (2014). Development of a crawler-type robot tractor using RTK-GPS and IMU. *Engineering in Agriculture, Environment and Food*, 7(4): 143-147.
- Tehmoor M. Dar and Raul G. Longoria (2010). Estimating traction coefficients of friction for small scale robotic tracked vehicles. *Proceeding of the ASME 2010 Dynamic System and Control Conference*, Cambridge, Massachusetts, USA, September 12-15.
- Tehmoor M. Dar and Raul G. Longoria (2010). Slip estimation for small scale robotic tracked vehicles. *American Control Conference*, Marriott Waterfront, Baltimore, MD, USA, June 30-July 02.
- TerrisGPS (2016). Explaining RTK in GNSS/GPS. Source: <http://terrisgps.com/what-is-gps-gnss-rtk/>
- Tillet N.D., Hague T. and Marchant J. A. (1998). A robotic system for plant-scale husbandry. *Journal of agricultural engineering research*, 69: 169-278.
- Van Henten E. J., Hemming J., Van Tuijl B. A. J., Kornet J. G., Meuleman J., Bontsema J. and Van Os E. A. (2002). An autonomous robot for harvesting cucumbers in greenhouses. *Autonomous Robots*, 13, 241–258.

- Van Willigenbug L. G., Hol C. W. J. and van Henten E. J. (2004). On-line near minimum-time path planning and control of an industrial robot for picking fruits, *Computer and Electronics in Agriculture*, 44: 223-237.
- Vectornav (2017). VectorNav Embeded Navigation Solution. Vectornav Technology, LLC (US). Source: <https://www.vectornav.com/products/vn-100>
- Watanabe K. and Kitano M. (1986). Study on steerability of articulated tracked vehicles-Part 1, Theoretical and Experimental Analysis. *Journal of Terramechanics*, 23(2):69-86.
- Wikipedia (2017). Rotating calipers. Source: https://en.wikipedia.org/wiki/Rotating_calipers.
- Wikipedia (2017). Convex hull. Source: https://en.wikipedia.org/wiki/Convex_hull.
- Wikipedia (2017). Inertial Measurement Unit. Source: https://en.wikipedia.org/wiki/Inertial_measurement_unit.
- Wikipedia (2017). Kalman filter. Source: https://en.wikipedia.org/wiki/Kalman_filter.
- Wong J. Y. (1989). *Theory of Ground Vehicles*. A Wiley-Interscience Publication, New York.
- Wong J. Y. and Chiang C. F. (2001). A general theory for skid steering of tracked vehicles on firm ground. *Proc Instn Mech Engrs*, Vol 215 Part D, pp:343-355.
- Wong J Y (2008) *Theory of ground vehicles*. A Wiley-Interscience Publication, New York.

- Yang L. and Noguchi N. (2014). An active safety system using two laser scanner for a robot tractor. Preprints of the 19th world Congress the International Federation of Automatic Control, Cape Town, South Africa, August 24-29.
- Yang L., Noguchi N. and Takai R. (2016). Development and application of a wheel-type robot tractor. *Engineering in Agriculture, Environment and Food*, 9(2): 131-140.
- Zhang F., Shin B., Feng X., Li Y. and Shou R. (2013). Development of a prototype of guidance system for rice-transplanter. *J. of Biosystems Eng.*, 38(4):255-263.
- Zhang Q., Reid John F. and Noguchi N. (1999). Agricultural vehicle navigation using multiple guidance sensors. In *Proceeding of the Int. Conf. on Field and Service Robotics*.
- Zhang Z. (2014). Development of a Robot Combine Harvester Based on GNSS. PhD theses, Graduate School of Agriculture, Hokkaido University, Sapporo, Japan. Source: <http://hdl.handle.net/2115/56100>
- Zhang Z., Noguchi N., Ishii K., Yang L. and Zhang C. (2013). Development of a Robot Combine Harvester for Wheat and Paddy Harvesting. *IFAC Proceedings*, 46 (4): 45-48.
- Zhang, C. (2017). Development of a Multi-robot Tractor System. PhD Theses. Graduate School of Agriculture, Hokkaido University, Japan.